Centre for Hyperpolarization in Magnetic Resonance (CHyM)

Utilising SABRE hyperpolarisation to enhance $^{13}C_2$ Pyruvate

Gulmira Konspayeva

University of York
Department of Chemistry

31th of March 2022

Declaration

I declare that this thesis has been composed solely by myself and that it has not been submitted, in whole or in part, in any previous application for a degree. Except where states otherwise by reference or acknowledgment, the work presented is entirely my own. All sources are acknowledged as References.

Abstract

Hyperpolarisation methods as signal amplification by reversible exchange (SABRE) can enhance nuclear magnetic resonance signals several orders of magnitude higher than those derived under Boltzmann conditions. SABRE is able to deliver the spin polarisation via the scalar coupling of the iridium catalyst at low magnetic field. SABRE techniques have been used for the hyperpolarisation of pyruvate, the substrate applied in many human MRI studies. In this thesis, we tried to optimise the $^{13}C_2$ Pyruvate signal gains delivered through SABRE varying NHC ligands (IMes, SIMes, IPr, SIPr) present in the sample, pyruvate's concentrations and the temperature at which the measurements were obtained on the level of delivered hyperpolarisation. We present the study of the effects of changing of these conditions and ligands on the production of the active $[Ir(H)_2(\eta^2\text{-pyruvate})(DMSO)(NHC)]$ catalyst to deliver a rationale for achieving high pyruvate signal. These approaches allow us to achieve signal enhancements of [1,2-^{13}C]Pyruvate, 341-fold for [1-^{13}C] and 301-fold for [2-^{13}C] of sodium pyruvate-1,2-[$^{13}C_2$]. Overall, in this the work we have shown that SABRE hyperpolarisation has the potential to aid clinical diagnosis of cancer via pyruvate metabolism.

Contents

Chapter 1. Introduction

Magnetic Resonance Imaging (MRI) is used to scan the human body in order to study disease by detecting anatomical and function changes. In fact, MRI can measure dynamic processes that occur at cellular and molecular scales at different stages of development and these measurements can provide information about morphology, structural connectivity, microstructure, as well as functional architectures (as reviewed by Dubois J, Alison M).[1] Moreover, a variety of disabilities can be diagnosed and prognosed through MRI measurements associated with clinical, behavioural, and electrophysiological markers. The main advantage of using MRI in this way is that it is non-invasive and non-destructive. MRI harnesses the quantum mechanical properties of 'magnetically' active atoms/nuclei endogenous to the body for its measurements. In chemical laboratories, the related method, Nuclear Magnetic Resonance (NMR), is widely used to obtain the structure of compounds.[2]

Nevertheless, there are essential functions that cannot be resolved with current MRI methods due to low sensitivity.[3] For instance, in some cases, MRI may be insufficient for distinguishing benign from malignant diseases (such as breast fibroadenomas), which may result in false positives.[4] Low sensitivity exists even though strong magnetic fields are now used in both MRI and NMR to compensate for this. The low sensitivity is primarily driven by the low thermal polarisation that exists between nuclear spin state alignments within a magnetic field. In case of the ^{13}C NMR, the main reason for low sensitivity is that carbon-13 nuclei account for about one percent of all the carbon nuclei. Carbon-13 NMR data, consequently, will be less sensitive (have a worse signal-to-noise ratio) than that of proton.

In fact, when a spin ½ nucleus like 13C or 1H is placed in an external magnetic field, it will exhibit two spin alignments or states (+1/2 and -1/2). The energy difference between these two states is very small and comparable to the thermal energy of the system. Thus the two spin states have similar populations according to the Boltzmann distribution. The ratio between these states determines how much detectable magnetisation is created, and this equates to approximately 1 in every 194,448 1H spins in a sample at 1.5 Tesla; it is 1 in every 777791 spins for 13C according to the Boltzmann equation (see section 1.3.1). Consequently, to provide a high-resolution image, a high concentration of nuclear spins is needed. Hence, MRI most commonly detects protons within the large water pool of the body.[5]

In order to increase the sensitivity of NMR and MRI measurements, various strategies have been studied. One of these solutions is to improve the hardware. Using this route, sensitivity can be increased by increasing the strength of the

magnetic field. For instance, doubling the strength of NMR and MRI scanner by changing a standard 1.5 T scanner with a 3 T scanner will improve the population difference by a factor of 2.25. As the strength of the field increases the energy difference between the spin states increases and thus the state population is altered. The equation that provides these calculations can be found in section 1.3.1. In addition to high magnetic fields using a high concentration of nuclei spins, or long acquisition times with signal averaging or reduced temperatures can also be used to deliver the required signal levels. However, these methods might not be practical to use for in-vivo measurements.[5]

More recently, a number of different techniques, to increase spin polarisation via chemical or physical means, have been established. These have been collectively named "hyperpolarisation" and refer to a situation where the distribution of magnetic spins deviates from that predicted by the Boltzmann distribution. Whilst a number of hyperpolarisation techniques have been developed, in this thesis I use one technique named Signal Amplification by Reversible Exchange (SABRE) to investigate hyperpolarisation of ^{13}C labelled pyruvate for easier detection with NMR/MRI.

In this thesis, the imaging potential of hyperpolarised $^{13}C_2$-pyruvate via SABRE is discussed. The main aims of this study are to apply methods for the optimisation of the catalytic hyperpolarisation of pyruvate. Understanding the effects of T_1 will be critical, and hence the quantification of both T_1 relaxation times and overall signal enhancement as a function of various catalysts containing NHC ligands (IMes, SIMes, IPr, SIPr), pyruvate concentration and the temperature at which the measurements are undertaken will be made.

It is important that these parameters are quantified to assess whether necessary time delays between preparation and detection will compromise final signal detection. Hence, the hypotheses of this research is that by developing optimised methods with increased magnetic state lifetimes and highest polarisation gains, signal detection will be possible over a longer time frame and this can provide significant advantages for tracer analysis.

1.1 Nuclear Magnetic Resonance (NMR)

Nuclear Magnetic Resonance (NMR) is a powerful and versatile spectroscopic tool used to determine both chemical and physical properties of materials in both liquid and solid states. NMR involves the interaction between nuclei' magnetic moments and magnetic fields. The NMR technique has undergone rapid development since its discovery by Felix Bloch and Edward Mills Purcell in 1946 from both an experimental and instrumental design viewpoint.[6] NMR has become an essential and routine tool in organic, inorganic, biological, and materials

science research, as well as medicine. It is quickly expanding into a vast interdisciplinary field in its own that is highly collaborative in practice rather than being a small part of the subjects as chemistry or physics. [7]

At the starting point, we need to look at the name of this method: Nuclear Magnetic Resonance. “Nuclear” is linked with properties of the nucleus. “Magnetic” is related to the behaviour of the nucleus in the presence magnetic field. By “Resonance”, we mean that we are manipulating atoms within magnetic fields through a modulation frequency corresponding with the nuclei’s characteristic frequency. To interact with NMR, atoms should have particular properties. Atoms with an odd number of nucleons have a quantum mechanical property known as a magnetic moment. This property will be explained in the next section (1.2 Spin Physics).

1.2 A brief history of Magnetic Resonance

As stated in the earlier section, NMR is a low-sensitivity technique, that is to say it requires a sample with high number of nuclei in order to create a bulk magnetisation vector that is detectable (for instance, 10^{-4}-10^{-6} moles of spins). A simple NMR experiment collect the information in a static homogeneous magnetic field and therefore macroscopic signal is detected. This signal provides overall information on microscopic dynamics and surroundings of the spins; however, the precise location of signal is impossible to detect.[8]

Nevertheless, if the NMR signal is boosted, it will give the opportunity to collect a signal from a particular area. In addition, the signal can be coordinated allowing spatial reconstruction.[9] This feature is now used in Magnetic Resonance Imaging technique for construction of the NMR local functions[10] and has increased in importance to image biological substances in the human body as well as in various research.

In terms of history, in 1973 Mansfield and Lauterbur represented 2D and 3D images in NMR which brought the Nobel Prize in 2003.[11] In the next decades, MRI developed in the new approaches as functional (fMRI) and anatomical imaging (DTI).[12]

Starting from the early development of computer-based scanning, over 120 years, there have been many steps in taking 3D images of the body. On the 8th of November 1895, Wilhelm Conrad Roentgen discovered "X-rays" during an experiment with a Crookes cathode ray tube.[13] X-ray absorption depends on tissue density, so absorption by bones is higher than softer tissues,[14] these qualities helped him to create an image which revolutionised diagnosis as it enabled medicine to see morphological structure of the body.[15]

The next ground-breaking investigation was based on emission tomography performed in 1963 by David Kuhl and Roy Edwards.[16] The single photon emission computed tomography (SPECT) data linked the results to a radionuclide concentration in vivo.[17] Nowadays, it tests real-time blood flowing within tissues and organs by using radioactive tracers. The radionuclide derived tracer releases a positron upon decay which ultimately creates two high energy photons through collisions with electrons present in neighbouring tissue. Detection of these photons forms the basis through which localisation of the positron emitter is possible thereby enabling the production of an image providing information about concentration and spatial location.[18] Over the last decades this imaging technique has been merged with Computer Tomography (CT), that is to say, the structural information from CT and functional signal from SPECT have been providing the improvement on anatomical localization.[19]

In 1973, Mike Phelps and Ed Hoffman[20] invented the improved version of Positron Emission Tomography (PET) scanner, which detects pairs of high-energy photons from a positron-emitting radionuclide. The principles of this detection provide high sensitivity and accuracy to estimate the concentration of radiotracer in vivo.[21] PET is applied for diagnosis of several diseases in oncology, cardiovascular and neurological systems. Moreover, the combination of PET and CT, since the beginning of the 2000, gives morphological and metabolic information about tissues,[22] which increases the sensitivity and the accuracy in clinical oncology.[23] Fluorine-18 fluorodeoxyglucose (FDGPET-CT)[24] is the most used tracer in oncology. Cells, which use glucose, bind to these tracers, then they are phosphorylated by hexokinase enzymes. This technique gives medicine capabilities to reveal the location of a cancer as well as its stage.[25,26] That means doctors might assess therapy response and how well treatment is working.

MRI benefits PET and SPECT as Magnetic Resonance does not need any injections. However, merging PET and MRI systems in 2010[27] enhanced the qualities of both sides by providing structural and quantitative information (MRI) and physiologic strengths (PET). This acquisition provides a more clear understanding of the functional and metabolic abnormalities in tissues.[28] Nevertheless, these hybrid imaging sequences are not broadly validated and that is why it requires further research.

Magnetic Resonance Spectroscopy (MRS) technique provides a non-invasive way for the presence and concentrations of metabolites within tissues.[29] This method allows for the biochemistry assessment such as choline (Cho), N-acetyl aspartate (NAA), creatine (Cr) and lactate determination. Particularly, choline and other choline containing compounds as metabolites displayed in Proton MRS have physiological significance through links to cell membrane turnover, rapid

cell division and/or breakdown.[30] Additionally, Proton MRS is a key for tumour metabolism's characterisation, especially in detection and monitoring brain, prostate, and breast cancers.[31] For instance, MRS might help to evaluate brain lesions by offering information on metabolites as lipids, alanine (Ala), glutamate-glutamine (Glx or GABA) and myoinositol (ml).[32]

The combination of ^{1}H-MRS and MRI might enhance the detection signal of breast cancer by 1.3%.[33] Since there is MRS, this detection is related to an increased metabolism such as decreasing signal-to-noise of choline resonance.[34] ^{1}H-MRS is a noninvasive biomarker of biochemical changes in tissues which are related to tumours. It can be useful in monitoring in a way choosing treatment and analysing the future steps with cancer patients. However, due to poor signal strength and low quality in special resolution, MRS is having limitations.[35] Future work with the development of this technique could also consider the facts of time-consuming and high complexity as well.

Nevertheless, the emergence of MRS and dissolution dynamic nuclear polarisation (DNP) as hyperpolarisation method can provide not only to assess ^{13}C related biochemical processes in real time, but also can enhance the sensitivity. There are few interrogations that have been done to evaluate normal and pathological tissue detected by this method owing to the increased signal intensity. Scientists believe that it is essential to continue studying hyperpolarisation with MRS, as it may expand application of, for example, hyperpolarised [1-^{13}C]pyruvate at investigating metabolic abnormalities[36].

Next parts of this section briefly describe the key features and principles of MRI. An overview of image sequences and image formation are presented in 1.4.5 and 1.4.6 sections.

1.3 Spin Physics

To fully explain nuclear spin and magnetic field interactions an in-depth understanding of quantum mechanics is required. To simplify, this thesis uses a mixed classical and quantum approach to discuss spin physics.

Nuclear spins can have a magnetic moment (μ) which interacts with an external magnetic field and results in the magnetic resonance phenomenon. This magnetic moment is caused by the spin angular momentum (I) of the nucleus (equation 1.1). Placing such magnetic dipoles in a constant magnetic field causes it to precess at a constant angular frequency that is highly stable (Figure 1.1(a)). Classical understanding of this would compare the magnetic moment, or nucleus, to a spinning bar magnet with north and south poles along the spin axis of the nucleus (classical model) (Figure 1.1(b)).[37] Importantly each nucleus has a

unique magnetic moment, and so a characteristic gyromagnetic ratio (Table 1) whose magnitude and sign ultimately determines the precession frequency and the sense of precession for a given spin quantum number.

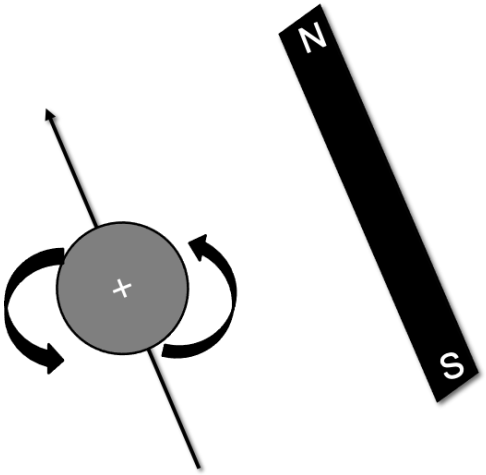

Figure 1.1. (a) when a rotating nucleus spins with positive charge, it creates a magnetic field oriented parallel to the axis of rotation known as the magnetic moment; (b) The rotating nucleus is comparable to a bar magnet in which the magnetic field is oriented from south to north.

$$\boldsymbol{\mu} = \gamma \boldsymbol{I} \quad (1.1)$$

A spin (*I*) is quantized into discrete values based on the atomic number and atomic weight of the particular nucleus. Nuclei with no spin (*I=0*): for instance, ^{12}C or ^{16}O cannot be investigated with MR since they do not interact with external magnetic field. In the case of odd atomic weights, a nucleus has a half-integral value for *I* (e.g., 1/2, 3/2, 5/2). Several elements common to biological systems are outlined in the Table 1 based on their spin and isotopic composition.

Table 1.1 Biologically relevant constants for certain nuclei.

Element	Nuclear composition		Nuclear spin, I	Gyromagnetic ratio, γ (MHz T^{-1})	% Natural abundance	ω at 1.5 T (MHz)
	Protons	Neutrons				
^{1}H, protium	1	0	½	42.5774	99.985	63.8646
^{2}H, deuterium	1	1	1	6.53896	0.015	9.8036
^{6}Li	3	3	1	6.26613	7.5	9.39919
^{12}C	6	6	0	0	98.90	0
^{13}C	6	7	½	10.7084	1.10	16.0621
^{14}N	7	7	1	3.07770	99.634	4.6164
^{15}N	7	8	½	-4.3173	0.366	6.4759
^{16}O	8	8	0	0	99.762	0
^{17}O	8	9	5/2	-5.7743	0.038	8.6614

^{19}F	9	10	½	40.0776	100	60.1164
^{23}Na	11	12	3/2	11.2686	100	16.9029
^{31}P	15	16	½	17.2514	100	25.8771

MR signal sensitivity also depends on gyromagnetic ratio (γ). According to the equation 1.2, the magnetisation (sum of magnetic moments in bulk matter – see below) is directly proportional to γ, the number of spins N, and the polarisation, P (relative population difference between spin states) :

$$M = \frac{\gamma \hbar N}{2} P, \quad (1.2)$$

where $\hbar$ is Planck's constant divided by 2π.[38] By this equation it is clearly seen that the higher the gamma the higher NMR signal sensitivity.

The ^{1}H nucleus, which consists of a single proton, is thus a perfect choice for investigating the body using MR. It has spin ½, the largest gyromagnetic ratio and it is the most abundant hydrogen isotope (high N). The body consists mainly of water and fat which contain hydrogen, and therefore normal tissues are very amenable to MR measurement by probing proton resonance.[39,40]

1.3.1 Production of Net Magnetisation

Within bulk matter the direction of magnetic moments of protons are randomly orientated (Figure 1.2 (a)). Individual magnetic moments cancel each other out, thus there is no net magnetisation.[41] However, when an external field is applied, the magnetic moments will align and precess parallel or anti-parallel to the field (Figure 1.2(b)).

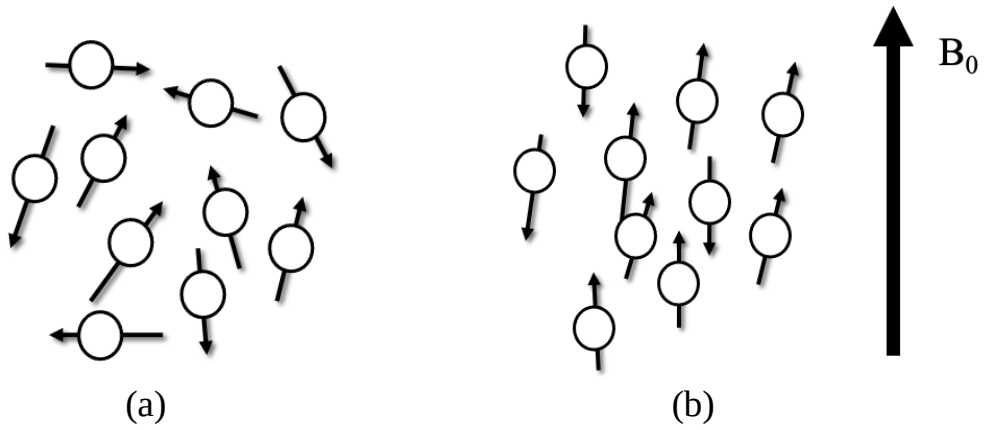

Figure 1.2. (a) If there is no external magnetic field, the orientation of spins may be random, and the total magnetic moment is therefore zero. (b) In the presence of a static magnetic field B_0, protons tend to align either parallel or anti-parallel to that magnetic field.

Figure 1.3 shows two different spin states with different energies (quantum theory) for protons arranged parallel and anti-parallel (classical theory) relative to their magnetic moments. As shown, in a static magnetic field, B_0, a proton can exist in just two energy levels. The resonance, i.e. the energy necessary for the spin to move from a low to a high energy state, is defined by the difference ΔE between these two states. This difference in energy is proportional to B_0 (equation 1.3) i.e. the higher the static magnetic field, the greater the energy separation between protons.[42]

$$\Delta E = \hbar \gamma B_0 \quad (1.3)$$

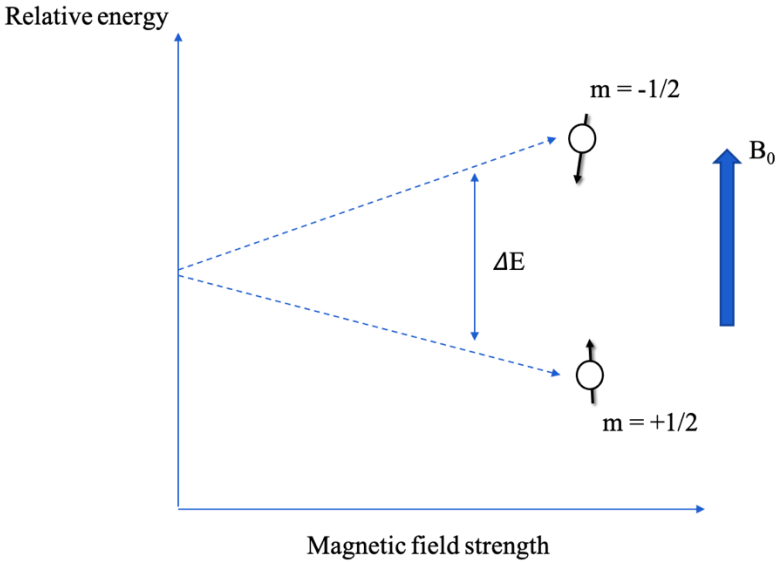

Figure 1.3. As a result of their spin state, protons can vary between the low- (spin-up) or high-energy (spin-down) states. This difference in energy increases with the static magnetic field B_0.

Basically, the spins precess at a constant rate and their overall vector is parallel to B_0. This precession is created owing to the interaction between magnetic field and the positively charged nucleus. By prevailing convention, in a coordinate system, *z* direction is the axis where B_0 and the spins precession will be oriented. The precession, therefore, is represented by coordinates perpendicular or transverse (x and y) and parallel or longitudinal (z) to the main magnetic field (Figure 1.4). The frequency of presession (ω) is proportional to the strength of the magnetic field, and the equation 1.4 is known as Larmor equation.

$$\omega_0 = \gamma B_0 \quad (1.4)$$

In an external magnetic field, according to $2I+1$ rule, for the spin -1/2, two states are possible: +1/2 and -1/2, at an angle defined by the nuclear magnetic moment's original orientation before the field was applied. Figure 1.4 illustrates that the

angle of spin polarization versus an external magnetic field remains constant over time, regardless of external perturbations that lead to relaxation. According to the Boltzmann distribution, parallel orientations to the field tend to be more likely, and the reason for that this orientation it is simply more energetically favourable.

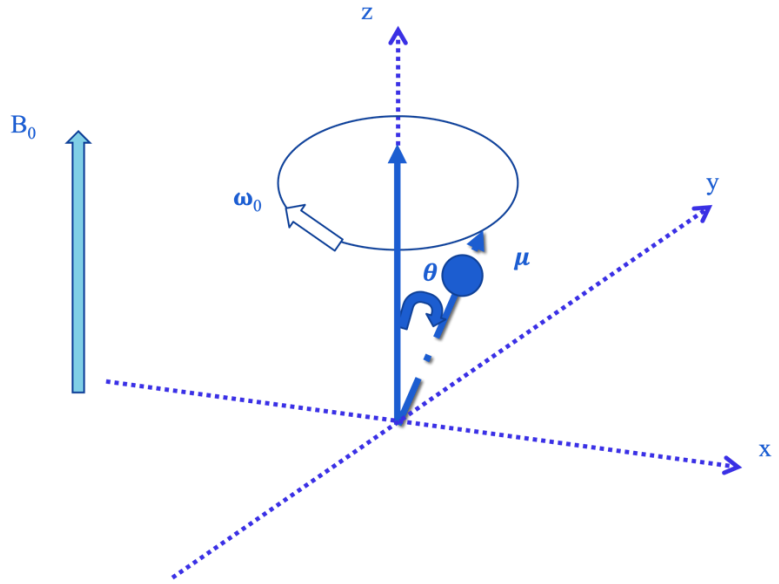

Figure 1.4. The precession of a magnetic moment **μ** in an applied magnetic field B_0 at Larmor frequency ω_0.

As long as there is thermal equilibrium between the system and its environment, the distribution can be calculated using Boltzmann law. If n_u and n_l are the number of particles in the upper and lower levels, respectively, and T equals absolute temperature, then,

$$\frac{n_u}{n_l} = e^{-\frac{\Delta E}{kT}} \quad (1.5)$$

where k is the Boltzmann constant ($k = 1.38066\times10^{-23}$ JK^{-1}) and ΔE the energy gap between the two levels. Considering equation 1.3 for protons in a field B of 9.4 Tesla (T), the unit of magnetic field equal to 1 kg s^{-2} A^{-2}, which is a typical magnetic field strength for NMR, at a temperature of 300 K, one finds that $\Delta E = 2.65 \times 10^{-25}$ J, $kT = 4.14 \times 10^{-21}$ J and $\Delta E/kT = 6.4 \times 10^{-5}$. Hence, reorienting the spins requires less energy than thermodynamic energy kT. Due to such small values of ΔE/kT, equation 1.5 may be simplified using $e^{-x} \approx 1-x$, the normalized population difference is calculated as following:

$$\frac{n_l - n_u}{n_l + n_u} = \frac{\Delta E}{2kT} \quad (1.6)$$

Based on these numbers, equation 1.6 corresponds to a population difference of $3.2\text{x}10^{-5}$ or one spin in every 31029 spins. For nuclei with lower gyromagnetic ratios (which are most of the nuclei in Table 1) or in a weaker field, the difference

will be even smaller. An overall magnetization, M_0, is the result of a population difference along the z axis direction.

It is also noted that nuclei with high gyromagnetic ratios and abundances are also preferred (equation 1.3), which explains the popularity of the ^1H nucleus in NMR.[41]

1.3.2 Concepts of Magnetic Resonance

Unfortunately, in practice an accurate determination of net magnetisation M_0 of tissue is not possible. The net magnetisation is instead perturbed, orthogonally to B_0 into the x-y (transverse) plane, and then detected as a result of continued precession around B_0. Perturbation requires a time-varying magnetic field B_1, as shown in Figure 1.5, in order to tip the net magnetization through some angle (flip angle). The exact frequency ω_0 at which B_1 oscillates is essential for causing spin transitions from the low to the high energy state. As the Larmor frequency is in the megahertz range(if the field strengths is higher than around 0.1T), B_1 is called a radiofrequency field (RF). As soon as the net magnetization moves into the transverse plane, the RF field is switched off and the excitation is completed.

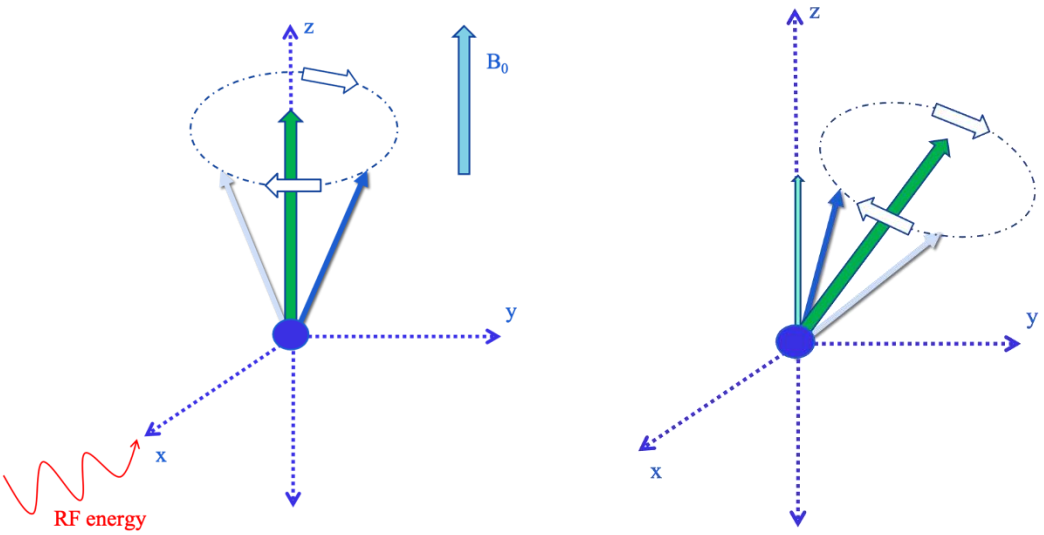

Figure 1.5. The application of RF energy to excite a magnetic nucleus

The net magnetization continues to precess about the static magnetic field, B_0 (z axis). This 'rotating magnetisation' will induce (Faraday's law) a time oscillating current in an antenna placed near a tissue sample. Therefore, the MR signal is also affected by the rotation frequency, which itself is linearly influenced by the static magnetic field B_0. In this regard, it becomes clear that increasing the static magnetic field B_0 may lead to an increase in both net magnetisation M_0 and induced MR signal through the Larmor frequency ω_0.[42,43]

The detected signal is known as a Free Induction Decay (FID) and it is generated solely by transverse magnetization (following RF excitation).

1.4 Relaxation

When the RF pulse is turned off, the spin system 'slowly' returns or relaxes back to its original equilibrium state. Two different relaxation processes are involved for the two components of the net magnetisation: the longitudinal (z) and transverse (x-y) processes. Longitudinal (spin-lattice) relaxation (T_1) is required for recovery of the z component of the magnetisation to its equilibrium state along the longitudinal (z) axis. In short, this process represents energy loss as protons lose energy to their surrounding lattice and drop from a high energy to low energy state.

The second relaxation process, transverse (spin-spin) relaxation, is responsible for decaying the component x-y as it precesses about the z axis and reduces the MR signal correspondingly. It represents the loss of spin coherence over time as local interacting spins affect local magnetic fields and therefore alter the precession frequency randomly.

Both longitudinal and transverse relaxation occur simultaneously, but the transverse relaxation process tends to be much faster in human tissue (on the order of ms compared to s for longitudinal relaxation). This means that the NMR signal decays (dephases) long before the spin system reaches equilibrium for repeat measurment.[44]

1.4.1 Relaxation time

To gather useful information that can be applied to a variety of clinical and neurological applications, the longitudinal relaxation time must be accurately measured in magnetic resonance imaging.[45] A sample's longitudinal relaxation time (T_1) is important for NMR and MRI analysis since in many cases the rate at which experimental observations can be repeated is determined by the rate of this time.[46]

Both relaxation times depend on the following factors:[47]

- Dipole-dipole coupling: this occurs when nuclei within the same molecule exhibit small magnetic fields due to rotating nuclei; since the molecule's position changes when it tumbles, these interactions vary in magnitude and direction. Magnetic field fluctuations that occur close to the Larmor frequency will cause relaxation to increase.

- Residual chemical shift anisotropy: Each chemical shift caused by the tumbling of a molecule is reflective of changes in the local magnetic field experienced by the nuclei.
- Spin rotation: In terms of importance, this is the least important mechanism, as it is the fluctuation of the magnetic field experienced by individual nuclei. The main magnetic field is too strong compared to individual nuclei' fields, so the influence of these rotations to relaxation times is marginal.

1.4.2 Longitudinal Relaxation Time

Known as the spin-lattice relaxation time, T_1 measures the time taken for the net magnetisation vector to return to its ground state in the direction of B_0. The process of relaxation follows an exponential decay and the time constant that tells how much time it takes to recover 63% of the magnetisation vector (Figure 1.6).[48]

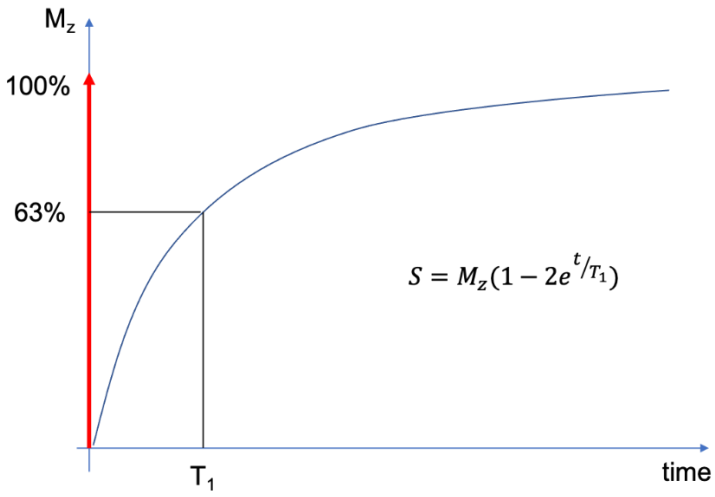

Figure 1.6. The recovery of M_z is an exponential process with a time constant T_1. This is the time at which the magnetization has recovered to 63% of its value at equilibrium

T_1 relaxation is an exponential process with a time constant T_1. For example, if a 90° pulse is applied at equilibrium, the z-magnetisation is saturated (reduced to zero) immediately after the pulse, but then recovers along the z-axis towards its equilibrium value, initially rapidly, slowing down as it approaches its equilibrium value (Figure 1.7). The shorter the T_1 time constant is, the faster the relaxation process and the return to equilibrium. Recovery of the z-magnetisation after a 90° rf pulse is sometimes referred to as saturation recovery.[44]

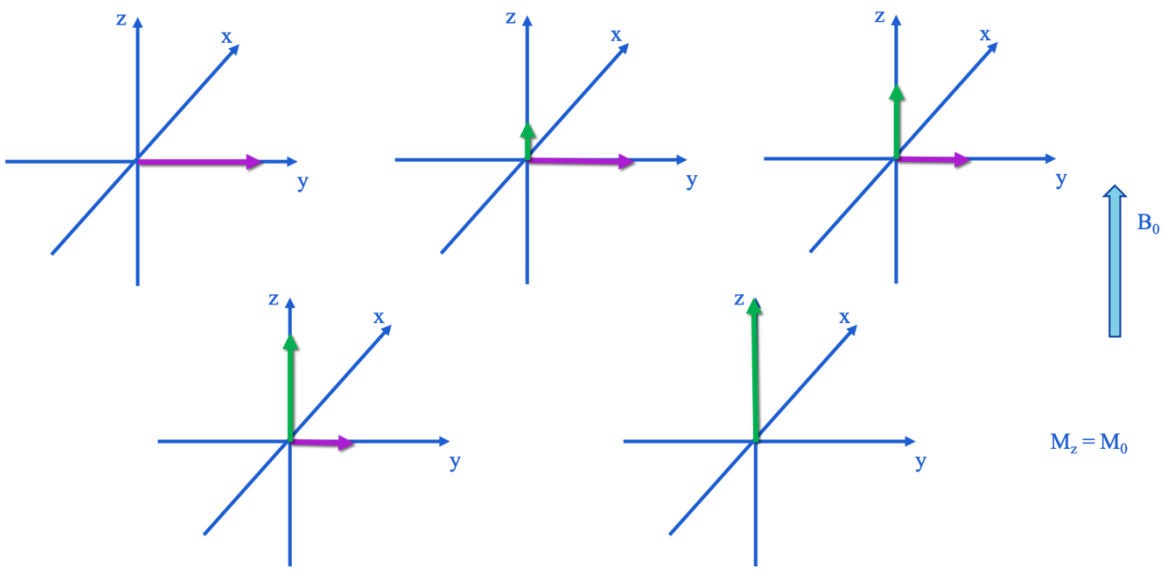

Figure 1.7. Diagram shows the process of T_1 relaxation after 90° rf pulse is applied at equilibrium. The z component of the net magnetisation, M_z is reduced to zero, but then recovers gradually back to its equilibrium value if no further r.f. pulses are applied

To measure T_1, the spin-lattice relaxation time, a 180° pulse is first applied to the sample so that the z -component of the total magnetization vector is rotated into -z. Then another 90° pulse is applied after a certain time t to rotate the magnetization back to the xy-plane, where precession of the magnetic moment becomes measurable. This sequence can be repeated to obtain a clearer signal through averaging.

Mathematically, this process can be described by a simplified version of the Bloch equations in the z -component:

$$\frac{dM_z}{dt} = \frac{M_0 - M_z}{T_1} \quad 1.7$$

This first-order differential equation has a solution of:

$$M_z(\tau) = M_0(1 - e^{-t/T_1}) \quad 1.8$$

Linearizing this equation gives:

$$\ln\left(1 - \frac{M_z(t)}{M_0}\right) = \frac{t}{T_1} \quad 1.9$$

M_z is directly related to the signal strength of the FID, and M_0 can be measured from the FID by applying a 90° pulse after allowing the sample to settle for

several seconds. Therefore, by plotting $\ln\left(1-\frac{M_z(t)}{M_0}\right)$ versus t, T_1 can be derived from the slope of the linear fitting function.[49]

1.4.3 Transverse relaxation time

Besides the longitudinal relaxation back to the equilibrium net magnetisation M_0, the magnetisation components in the transverse plane undergoes relaxation too. This process of the transverse relaxation is due to the interaction of the magnetic moments of protons within the same molecule leading to so-called dephasing and a resultant reduction of the transverse component of the net magnetisation. The transverse relaxation times, which are denoted T_2 and T_2*, also depend on the tissue type and are in the order of a few 10 ms (compare with a few 100 ms for T_1 relaxation). In the process of relaxation, tissue magnetisation is decomposed into its transverse (T_2/T_2*) and longitudinal (T_1) contributions.[42]

Transverse relaxation can be understood by remembering that the net magnetisation is the result of the sum of the magnetic moments (spins) of a whole population of protons. Immediately after the r.f. pulse they rotate together in a coherent fashion, so that as they rotate they continuously point in the same direction as each other within the xy plane. The angle of the direction they point at any instant is known as the phase angle and the spins having similar phase angles are said at this initial stage to be 'in phase' (Figure 1.8). Over time, for reasons explained in a moment, the phase angles gradually spread out, there is a loss of coherence and the magnetic moments no longer rotate together and they are said to move 'out of phase'. The net sum of the magnetic moments is thus reduced, resulting in a reduction in the measured net (transverse) magnetisation. The signal that the receiver coil detects (if no further rf pulses or magnetic field gradients are applied) is therefore seen as an oscillating magnetic field that gradually decays (known as a Free Induction Decay or FID). There are two causes of this loss of coherence. Firstly, the presence of interactions between neighbouring protons causes a loss of phase coherence known as T_2 relaxation.

This arises from the fact that the rate of precession for an individual proton depends on the magnetic field it experiences at a particular instant. While the applied magnetic field B_o is constant, it is however possible for the magnetic moment of one proton to slightly modify the magnetic field experienced by a neighbouring proton. As the protons are constituents of atoms within molecules, they are moving rapidly and randomly and so such effects are transient and random. The net effect is for the Larmor frequency of the individual protons to fluctuate in a random fashion, leading to a loss of coherence across the population of protons. i.e. the spins gradually acquire different phase angles, pointing in different directions to one another and are said to move out of phase with one

another (this is often referred to as de-phasing). The resultant decay of the transverse component of the magnetisation (M_{xy}) has an exponential form with a time constant, T_2, hence this contribution to transverse relaxation is known as T_2 relaxation (Figure 1.8). As it is caused by interactions between neighbouring proton spins it is also sometimes known as spin-spin relaxation. Due to the random nature of the spin-spin interactions, the signal decay caused by T_2 relaxation is irreversible. The second cause for the loss of coherence (de-phasing) relates to local static variations (inhomogeneities) in the applied magnetic field, Bo which are constant in time. If this field varies between different locations, then so does the Larmor frequency. Protons at different spatial locations will therefore rotate at different rates, causing further de-phasing so that the signal decays more rapidly. In this case, as the cause of the variation in Larmor frequency is fixed, the resultant de-phasing is potentially reversible. The combined effect of T_2 relaxation and the effect of magnetic field non-uniformities is referred to as T_2* relaxation and this determines the actual rate of decay observed when measuring an FID signal. T_2* relaxation is also an exponential process with a time constant T2*. [44,48]

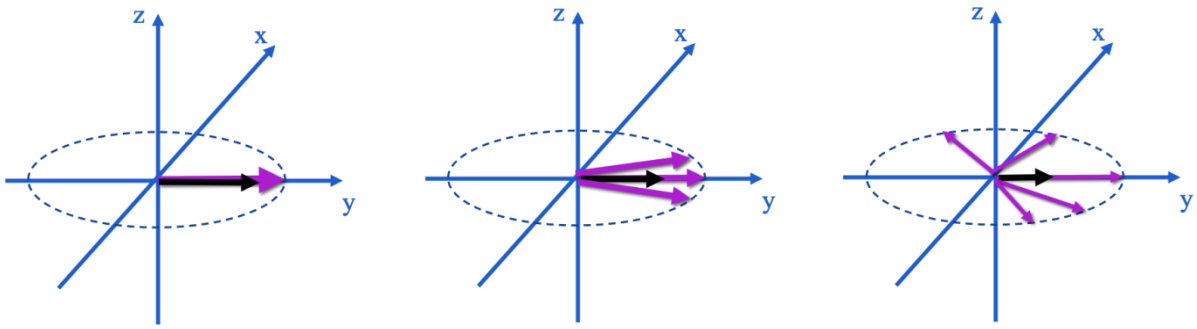

Figure 1.8. De-Phasing (Loss of Phase Coherence) During T_2

In theory, T_2 can be measured by examining the envelope of the FID directly. However, inhomogeneity in the magnetic field applied causes the individual magnetic moments of the nuclei to precess at slightly different frequencies and de-phase, where they will begin to partially cancel each other, as the signal decays. This will reduce the component of the total magnetization vector in the xy-plane faster than by T_2 alone. This effective decay time is termed T_2 inhomogeneous and is always less than the pure T_2. To solve this problem, a 180^o pulse is applied after a time t after the initial 90^o pulse. This reverses the phase of the individual magnetic moments of the nuclei so that the higher frequency moments now lag the lower frequency ones and vice versa. After a time t following the 180^o pulse, the magnetic moments will be in-phase again and generate a signal, a spin echo, whose strength depends solely on the pure T_2 and the time that has elapsed since the 90^o pulse (2t).

Mathematically, this process can also be described using a simplified version of the Bloch equations in the transverse direction:

$$\frac{dM_{xy}}{dt} = -\frac{M_{xy}}{T_2} \quad 1.10$$

This equation has a solution of:

$$M_{xy}(t) = M_{xy0}(e^{-t/T_2}) \quad 1.11$$

Linearizing this equation gives:

$$\ln\left(\frac{M_{xy}(t)}{M_{xy0}}\right) = \ln\left(M_{xy}(t)\right) - \ln\left(M_{xy0}\right) = -\frac{t}{T_2} \quad 1.12$$

By plotting ln (M_{xy} (2t)) versus 2t, T_2 can be obtained from the slope of the linear fitting function. [49,50]

1.4.4 Importance of the T_1 value

T_1 relaxation involves the release of energy from the proton spin population as it returns to its equilibrium state. The rate of relaxation is related to the rate at which energy is released to the surrounding molecular structure. This in turn is related to the size of the molecule that contains the hydrogen nuclei and in particular the rate of molecular motion, known as the tumbling rate of the particular molecule. As molecules tumble or rotate they give rise to a fluctuating magnetic field which is experienced by protons in adjacent molecules. When this fluctuating magnetic field is close to the Larmor frequency, energy exchange is more favourable. For example, lipid molecules are of a size that gives rise to a tumbling rate which is close to the Larmor frequency and therefore extremely favourable for energy exchange. Fat therefore has one of the fastest relaxation rates of all body tissues and therefore the shortest T_1 relaxation time. Larger molecules have much slower tumbling rates that are unfavourable for energy exchange, giving rise to long relaxation times. For free water, its smaller molecular size has a much faster molecular tumbling rate which is also unfavourable for energy exchange and therefore it has a long T_1 relaxation time. The tumbling rates of water molecules that are adjacent to large macromolecules can however be slowed down towards the Larmor frequency shortening the T_1 value. Water-based tissues with a high macromolecular content (e.g. muscle) therefore tend to have shorter T_1 values. Conversely, when the water content is increased, for example by an inflammatory process, the T_1 value also increases. [44,51]

In NMR, relaxation time enables the user to measure average signal. In hyperpolarisation, since the non-equilibrium state is involved, it must be measured before this state disappears. The other consideration on using HP analytes should be the factors that affect T_1-relaxation. In order to yield a long T_1, a number of research have been considered. For example, perdeuteration of samples[52–54] or long-lived singlet states (LLS)[55–57] were found to prolong the T_1.Significant research have been done by Levitt's group by creating nuclear spin order in high field,[58,59] and they also displayed a singlet decay time constant of more than an hour.[60] Levitt and co-workers have demonstrated that singlet order is available from the hyperpolarised [1,2-$^{13}C_2$]pyruvic acid containing coupled spin ½ pairs giving a decay constant of 70 s using DNP.[61] Several studies have demonstrated a longer T_1-relaxation can be measured at higher temperature.[62–65] Concentrations and the magnetic field strength have also influence on hyperpolarized signal lifetimes as David M. Wilson discussed in their review article.[66] pH dependence of T_1 has shown that when H_3O^+ concentrations is increased, T_1 of hyperpolarised pyruvate declines by approximately 2.5-fold compared to physiological pH.[67] Field dependence of T_1 have been also studied and concluded that presumably due to increased influence of chemical shift anisotropy, a shortening T_1 of hyperpolarized ^{13}C pyruvate was observed at higher fields.[68,69]

Since this thesis is focused on pyruvate polarisation, its lifetime will be also considered in Results and Discussion section **(Chapter 5)**.

1.4.5 Free Induction Decay

As indicated, when an RF pulse is switched off, T_1 and T_2 relaxation occur simultaneously and independently. The protons continue to precess and the sum magnetisation vector follows a spiralling path whereby its direction and magnitude are constantly changing. Hence, an electrical signal is generated in a suitable receiver coil. The MR signal generated from the spiralling sum magnetisation vector is termed FID. It has its greatest magnitude immediately after the RF pulse is switched off and then decreases as both relaxation processes occur. It also has a constant frequency (resonant frequency) and consequently the FID signal takes the form of a sine wave with a rapidly decaying envelope (Figure 1.9).

An FID is most commonly depicted with a 90° pulse but a RF pulse of any flip angle can create an FID because some components of the longitudinal magnetisation are always tipped into the transverse plane. Theoretically, a 180° RF pulse should refrain from generating an FID. However, in practice, all 180° pulses are imperfect and produce FID signals. FID is subjected to further disruption (de-phasing) by the magnetic field gradients that are used to localise

and encode the MR signal. Consequently the signal generated by FID is not usually measured in MRI. Instead, it is common practice to generate and measure the MR signal in the form of an echo: typically a spin echo (SE) or a gradient echo (GRE). Echoes can be appreciated by considering how T_1- and T_2-weighted images are formed.

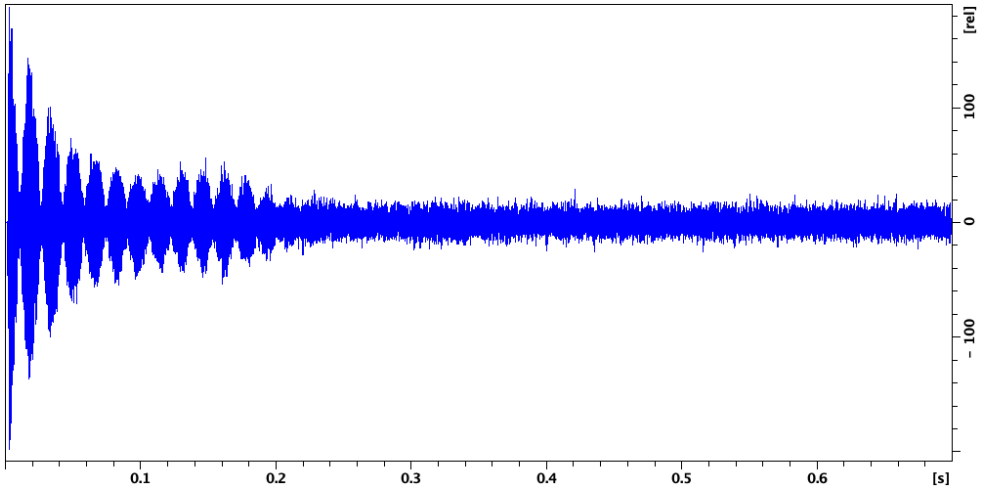

Figure 1.9. The received signal detected by the receiver coil, the FID, decreases over time when the net magnetization vector returns to its original orientation. The image taken from the experiment with [IrCl(COD)(IMes)] (2mg), DMSO-d_6 (1.5uL), $^{13}C_2$ pyruvate (2 mg) in MeOD from TopSpin (Constant Flip Angle Experiment with 5° Pulse and 5 seconds delaying time).

1.5 Principles of Magnetic Resonance Imaging

The development of MRI in medicine has allowed precise investigations of disease states without exposure to ionising radiation and thus, the use of this tool is becoming prevalent.[70] Understanding how this technology works and its applications can be informative to see its advantages and limitations. In this part of the thesis, the principles of MRI are reviewed, with further discussion of slice selection, magnetic field gradient, frequency and phase encoding. MR spectroscopy is also considered, with an overview of Fourier Transform Imaging Principles.

Figure 1.10 depicts a block diagram of the main components of an MRI system (setup for imaging the human head). It consists of a superconducting magnet (generating B_0), gradient systems/coils (for spatial localisation), shim coils (for making the magnetic field homogeneous) and a radiofrequency (RF) coil system (for excitation of magnetisation).[51]

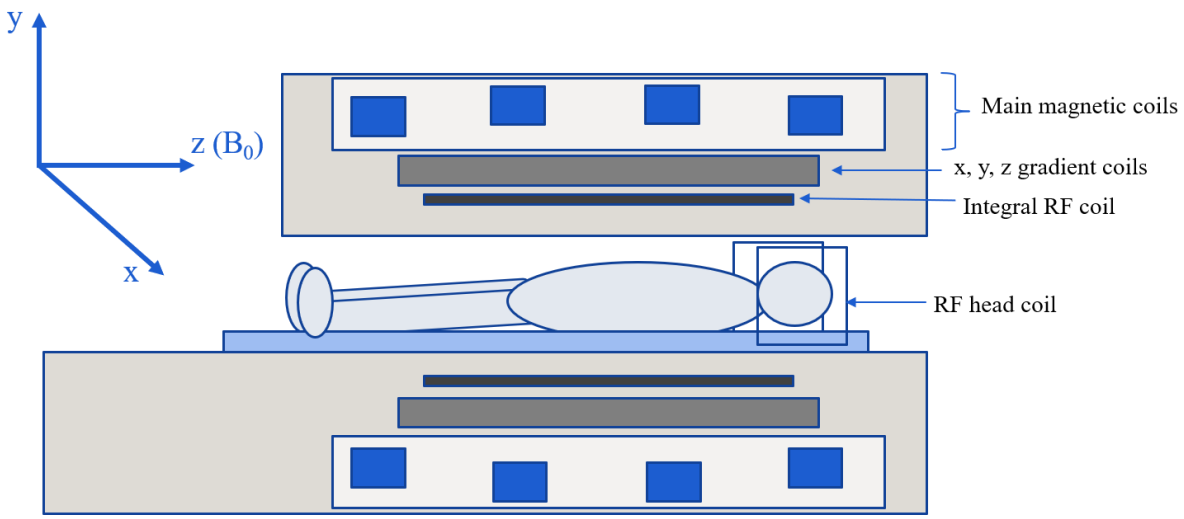

Figure 1.10. The relative locations of magnetic coils in MRI scanner. These coils positioned by the following order (from the furthest to closest to the patient): the main magnetic coils; x, y and z gradient coils and RF coils. RF head coils are used for neuroimaging.

Maxwell's equations determine that when a current flows in a wire, it induces an orthogonal magnetic field. Lowering the resistance of the wire allows for effective use of high electric currents to generate high strength magnetic fields. By this principle, in MRI superconducting solenoids are used to generate magnetic fields, B_o, in the Tesla range. The superconducting alloy must be cooled to around 4 K by cryogenic liquid helium.[71]Nowadays, the majority of clinical scanners work at 1.5 T or 3 T and higher strengths which reach to 9.4 T are used mostly in research.[72]

To encode spatial information three orthogonal gradient coils are used to produce a linear gradient change in magnetic field along the principle Cartesian axes (x, y and z directions)[73] (Figure 1.10). Further explanation how these gradient coils operate can be found in section 1.5.1.

The RF coil produces the orthogonal B_1 field required to excite the nuclear spins. Once the system is excited, the same RF coil can be used to measure the time oscillating current, induced by precessing magnetisation. In simple terms the RF coil acts like a "broadcasting station" of the MRI system: they transmit RF energy and receive signals back from the sample.[74] There are many types of RF coils, for example, some of them play a transmitting and receiving role, while others can perform only one of these functions. To illustrate, in neuroimaging applications, RF excitation is done by a body sized coil. An additional, much smaller RF receiver coil applied around the person's head in order to increase the signal from brain. (Figure 1.10). Smaller RF detectors/receivers are much more sensitive.

Producing high quality signals requires spatial homogeneity. Unfortunately, the main magnetic field is distorted by materials with high magnetic susceptibility. Field distortions, particularly enhanced around air-tissue interfaces,[75] can cause high intensity artefacts, geometrical image distortions, signal voids or other issues linked with magnetisation refocusing or receiving of the signal.[76] To avoid these problems a set of current carrying shim coils are deployed. They generate specific/localised magnetic fields to correct field distortions and homogenise B_0 across the sample.[77]

1.5.1 Magnetic Field Gradients

In 1973, Lauterbur's article introduced the idea of a spatial variation of magnetic field to locate the spins in three-dimensional space.[78] To illustrate, if a linear magnetic field gradient (G_x) is applied along the *x*-axis it will causes a linearly varying change in frequency while it is on. Assuming, the magnet isocentre is the centre point of the main magnetic field B_0, the resulting resonant frequency ω_x *is*:

$$\omega_x = \gamma(B_0 + xG_x) = \omega_0 + \gamma G_x \qquad (1.13)$$

Thus, the measured frequency, will be dependent, or 'encoded', its position x. Appropriate coils are orientated to affect such changes along the three Cartesian axes through the application of appropriate linear gradients or through their trigonometric combination (figure 1.11a). Application of these gradient coils allows slice, phase and frequency encoding for spatial localisation as described below.

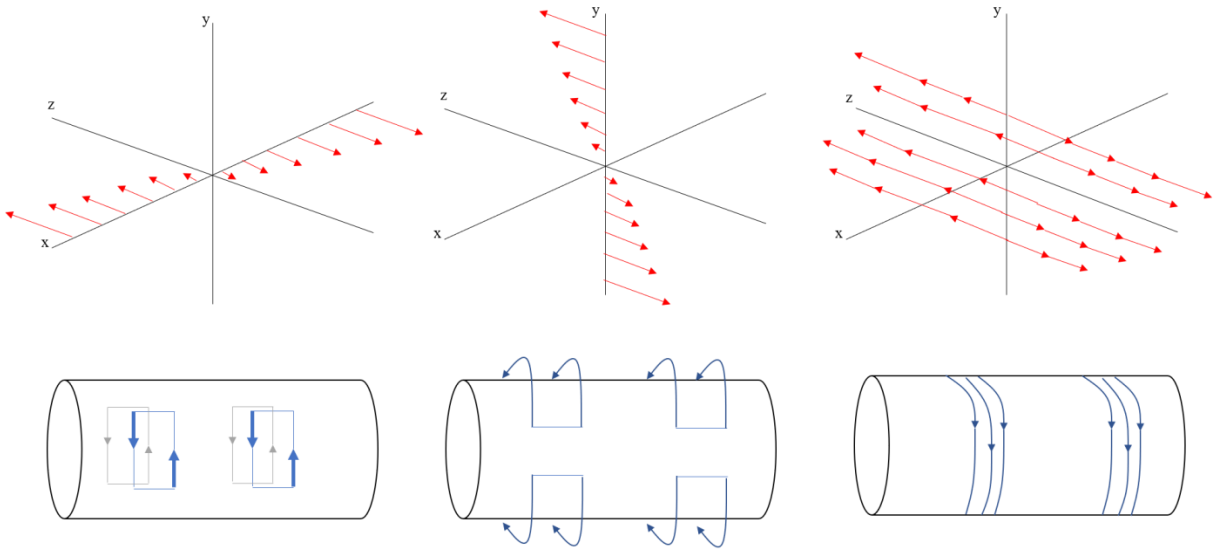

(a)

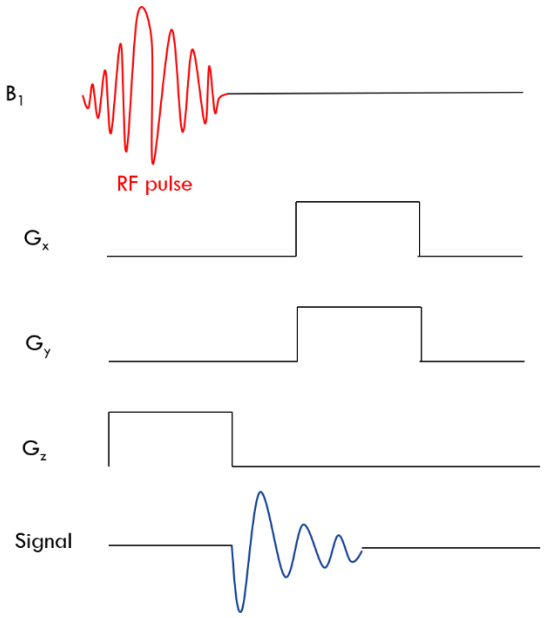

(b)

Figure 1.11. (a) Diagram represents the x, y and z field gradients and saddle coil configurations in a magnet bore. Arbitrarily oriented magnetic field gradients can be produced by turning on several gradient coils simultaneously; (b) RF pulse (90º) is activated by G_z which is a slice selective gradient, and the spins which are positioned in a particular slice perpendicular to the direction of the gradient will be rotated. In the plane, the readout gradient (in this case G_ω, is a linear combination of gradients along x and y axes.[79]

Importantly, the imaging plane can either be placed in a coronal (perpendicular to the *y*-axis), axial (perpendicular to the *z*-axis) or sagittal (perpendicular to the *x*-axis) orientation. By convention the z-axis extends from head to foot, the y-axis runs along the back to the abdomen and the x-axis from side-to-side axis.[80]

1.5.2 Slice Selection

For 2D imaging (i.e. capturing a single slice of MRI data) a gradient is first applied in conjunction with a narrow bandwidth RF pulse ω_{pulse}. Herein, only spins that precess in the frequency range $\omega_{pulse} \pm \Delta\omega_{pulse}$ are affected and thus a plane of spins are excited. The thickness of the excited slice is determined by the gradient strength and this RF bandwidth. This is known as a slice selection gradient (G_{slice}) and it is most commonly applied in the z direction (G_z). It is turned off when the RF pulse is turned off (see figure 1.12).

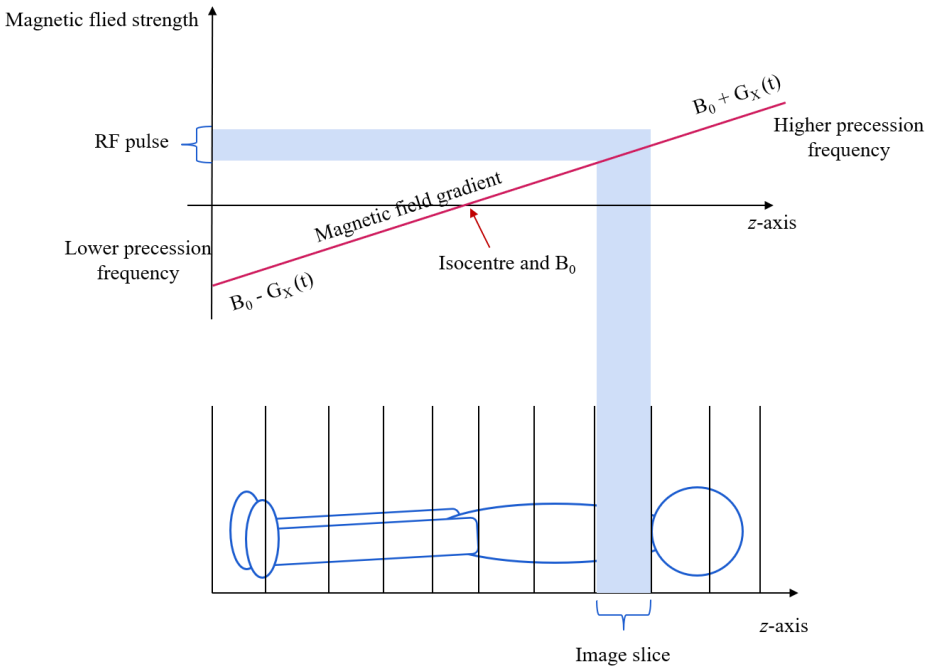

Figure 1.12. Slice selection. It is applied by combination a magnetic field gradient G_{slice} and RF pulse. The Larmor frequency used is determined by the location along the gradient (here along the z axis) and excitation only occurs where the tissue frequency matches the RF pulse.[81]

[94]The source of the signal is now located to a certain slice, but further encoding gradients are needed to identify the location of that signal in that selected plane.

1.5.3 Back Projection

Following slice selection a simple back-projection technique can then be used to recover spatial information within this 2D plane by recording multiple frequency spectra under varying directions of the applied gradient.[82] A linear combination of the two remaining gradients (G_x and G_y) control the angle θ of the frequency encoding gradient (G_ω)[83] by following equations:

$$G_x = G_\omega \cos\theta \quad (1.8(a))$$
$$G_y = G_\omega \sin\theta \quad (1.8(b))$$

Based on the spatial variation of ω, an NMR spectrum is recorded which shows peaks for each angle. Afterwards, for example, the inverse Radon transform can be used to back project the data of NMR spectra.[84] Back projection methods have now been superseded through a process known as phase encoding.

1.5.4 Phase Encoding

After the slice selection and RF pulse, but before the main acquisition time of signal, a phase encoding gradient (G_P or G_y) nominally along *y*-axis, is applied. (Figure 1.9a).[85] This again creates a different rotation frequency according to position along the y axis. In areas of increased magnetic field protons to precess at a higher rate, whereas in areas of lower magnetic field, the protons will precess at lower frequencies. Turning this gradient off after a short period therefore induces relative phase differences across the sample dependent on position along that gradient (figure 1.9b).[86] The level of the phase shift between any two positions along the axis is determined by the steepness/strength of the gradient G_P's. Thus, a shallow phase-encoding gradient results in a smaller shift in phase.[87]

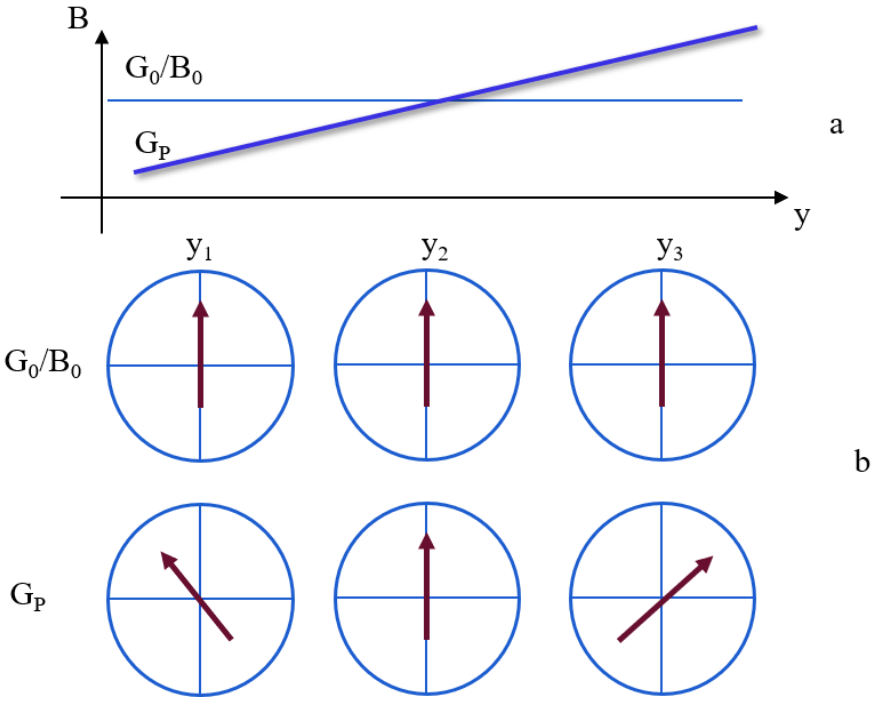

Figure 1.9. (a) Application of phase encoding gradient (G_P) and the magnetic field offset without field gradient (G_0/B_0); (b) diagrams representing rotating frames for the spins located at three different points in space without and with applied field gradient

This procedure is repeated (for instance, 128 or 256 times) whilst changing the phase encoding gradient amplitude to encode varying phase shifts in each step.[88,89] When the amplitude of these signals are plotted, they form a wave with precise frequency[90] (Figure 1.10) which will be discussed in the next section. The computing technique called Fourier transform is used to convert this information into an image.[91] These phase encoding steps control the resolution along the *y*-axis, and when coupled with a need to wait for magnetisation to return to equilibrium (order of seconds) between subsequent encoding steps lengthen the total acquisition processes.[92]

1.5.5 Frequency Encoding

A further gradient is applied after phase encoding to introduce frequency encoding (G_F or G_x) in the *x*-direction. It changes the frequencies of the protons relative to their position along that x-axis[93] (Figure 1.10). The recorded signal (time oscillating current) will be a super position of these frequency responses which encodee x position.

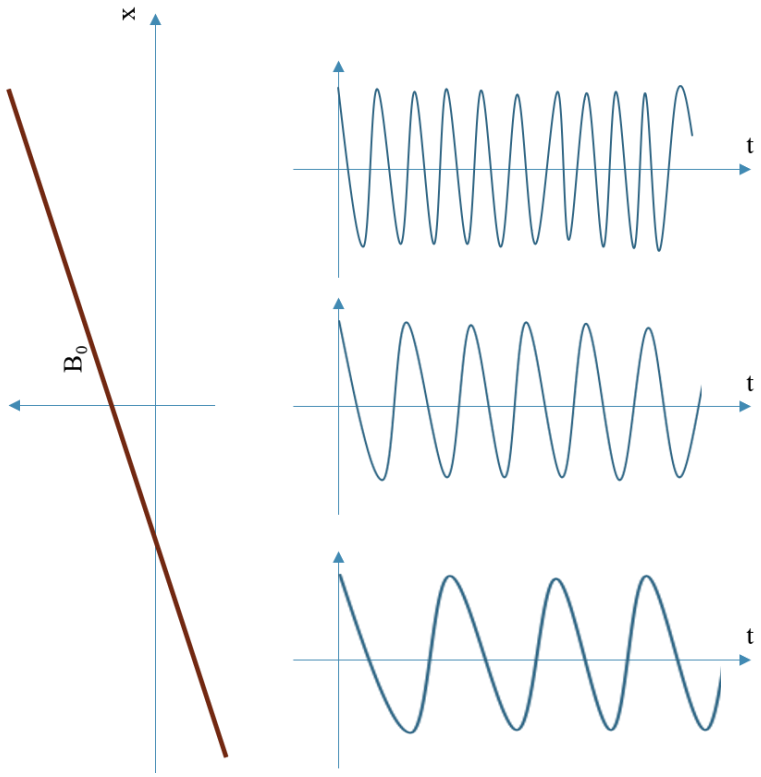

Figure 1.10. The frequency encoding gradient is applied in the plane of the selected slice and perpendicular to the phase encoding direction.

This information is again extracted by Fourier transform (FT).

Spatial frequency data encoded by the phase an frequency gradients form k-space. The Fourier transform of k-space reveals the target image. Further discussion about this process are beyond the scope of this work.

1.5.6 Imaging Sequences and Image formation

Imaging sequences contain a number of RF pulses and gradients and result in images that possess certain characteristics. Such sequences are therefore defined by a set of varying of gradients and these are combined in several ways. This section will briefly describe common sequences, such as the spin echo and gradient echo.

The spin echo sequence is used as an alternative to a single pulse to excite spins in a particular slice. For instance, there is an alternating 90°- and 180°-pulses every TR (repetition time) and TE (echo time) respectively, this causes the rephasing of the spins and consequently generating an echo signal.[94] Several various phase encoding complete the k-space lines. Constant field heterogeneities are compensated by 180° rephasing pulse, resulting in weighting the echo that in T_2 and rather in T_2*.[95]

The first of 90-degree and 180-degree pulses produces an FID by turning magnetisation into the transverse plane. As the FID signal decays according to T_2* this signal is dependant on magnetic field inhomogeneity. Hence if another 180-degree pulse is added to produce an echo; this pulse will "reverse" the sense of precession of the protons, and consequently refocus the proton signals regardless of their precession rate. The protons return to the same point after the same period of time elapses as they did before 180° pulse. The time when the scanner receives the echo signal is called the echo time (TE), and 180° pulse should be applied at TE/2 (Figure 1.11). As it discussed earlier, such sequences must be repeated for each time interval to produce the image. This time is known as the repetition time (TR) (Figure 1.11). [96]

The second common sequence is the gradient echo sequence (GRE). There is no application of a 180° pulse and therefore T_2* effects will present. To form an echo in this sequence, a reversing gradient will be acquired. By this reversing, the peak occurs in the middle of the signal, thus, the protons rephase forming an echo as represented in the next diagram. The initial pulse excites the spins by flipping them less than 90°. This flip angle allows longitudinal magnetisation to remain visible for as long as possible; therefore, its leaves magnetisation available for the next repetition and avoid poorness of the sequence's signal. [97]

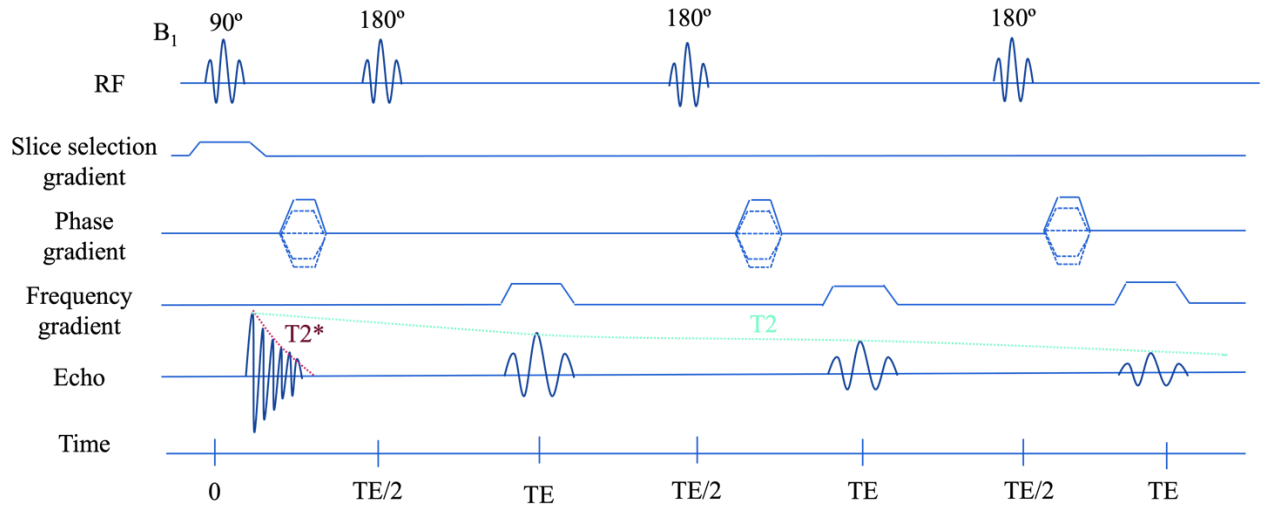

Figure 1.11. A common scheme for MRI pulse sequences. It includes spin echo and special localisation gradients, each of which is applied along a specific axis to create a certain echo, a different phase encoding gradient is applied.

Owing to the various phase encoding steps, a k-space line is completed for each repetition with TR; also, the "reverse" 180° pulse improves homogeneity and therefore leaves only T_2 effects by cancelling out T_2*. The number of k-space's lines is referred to as the matrix size by its dimension (for instance, 128 x 128). That is to say, 128 signal and 128 phase encoding repetition steps are required. This matrix is then processed by Fourier transform to generate the image. The matrix size is directly proportional to the final image size in pixels.

All acquired signals can be depicted as a combination of sine and cosine waves. Each of which then reflects a certain frequency contribution within the combined signal. A French mathematician, Joseph Fourier, discovered an approach to decode these measurements into their component frequencies. A detailed explanation of spatial resolution in MRI can be read in "Principles of MRI" by Friedman et al.[98]

Chapter 2. Literature review

2.1 Hyperpolarisation

The low sensitivity in NMR and MRI is due to the very low effective concentration of some nuclei and thlow thermal polarisation of spin states that can be represented by equation 1.4. The population of these spin states is determined by the Boltzmann distribution. A number of solutions exist to overcome low sensitivity including the use of stronger magnets, reduced temperature or high sample concentration. However, owing to high cost (stronger magnets) or impracticality (lowering temperature or increasing sample concentration), these approaches cannot be readily used in human body detection measurements.

Therefore, one of the most promising methods which could overcome low signal sensitivity is hyperpolarisation. Hyperpolarisation enhances a signal by forcing spins into the low energy state, thus increasing the difference between spin populations, and so the signal polarisation (Figure 2.1). This process might contribute to an enhancement in sensitivity of NMR/MRI between 4 and 8 orders of magnitude over what is normally available.[99]

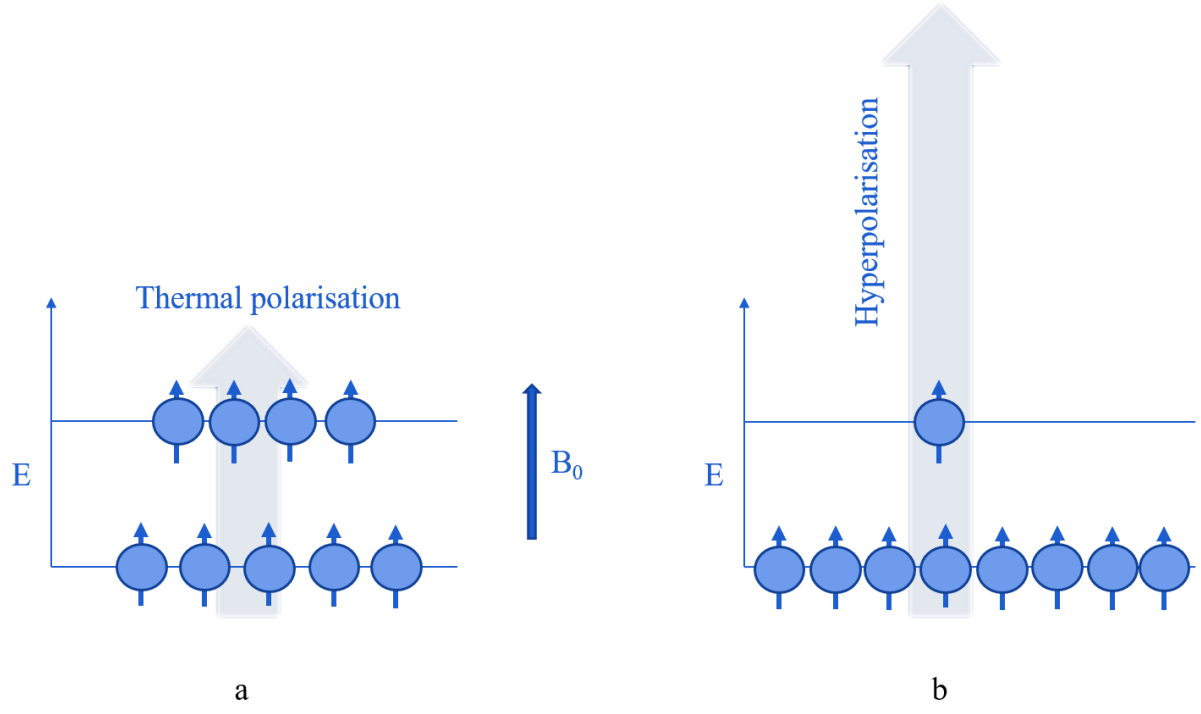

Figure 2.1. a) Boltzmann distribution of spins at thermal state; b) the distribution at hyperpolarisation state.

In this thesis, hyperpolarisation methods, such as Spin Exchange Optical Pumping (SEOP), Dynamic Nuclear Polarisation (DNP) and Para-Hydrogen

Induced Polarisation (PHIP) will be briefly described. A PHIP derivative known as Signal Amplification by Reversible exchange (SABRE) is the main technique that was utilised to enhance Pyruvate peaks in this project.

2.1.1 Spin Exchange Optical Pumping

Spin Exchange Optical Pumping (SEOP) is mostly used for the hyperpolarisation of noble gases such as ^{3}He and ^{129}Xe. In the past 20 years, these gases have been used to probe the interfaces associated with lung ventilation.[100] Additionally, due to the high solubility of xenon-129 in red blood cells, lipids[101] and other biological tissues, its inertness and large and loosely bound electron cloud through van der Waals forces, which is the reason for its large chemical shift sensitivity,[102] its hyperpolarisation has allowed the measurement of gas exchange mechanisms within the lungs,[103] brain[104] and kidneys.[105]

In SEOP, the valence electrons of an alkali metal (basically, Rb) vapour which are in a glass cell, enable polarisation through their absorption of circularly polarised photons. This results in the depopulation of one of the electronic states and thereby causes a polarisation of its electron spin. Afterwards, through the hyperfine interactions that exist between the alkali-metal and inert gas atoms some of this polarisation is transferred to the xenon-129 or helium-3 nuclei.[106] There is a severe shortage of helium-3 though,[107] while extraction of xenon-129 from liquified air is far more available. Hence, SEOP with this noble gas reflects the cheaper and more environmentally friendly option for imaging.

However, most hyperpolarised ^{129}Xe research uses expensive naturally abundant xenon (NAXe) gas mixtures; moreover, both noble gases require a polariser to prepare and process them, which leads to an increase in cost. In recent years, MR lung imaging has developed as a cheaper technique through inhaling fluorine-19 as inert fluorinated gases such as sulfur hexafluoride (SF_6) or per-fluoropropane (C_3F_8). There is no need to polarise ^{19}F due to its high gyromagnetic ratio.[108] Scientists have been utilising this method to acquire functional measurements in animal lungs: wash-in and wash-out kinetics of inhaled SF_6;[109] the lung's volume measurements over the course of the respiratory cycle via SF_6;[110] obstructed ventilation using inert fluorinated gases[111] and quantitative mapping of ventilation-to-perfusion ratios in the lung.[112]

2.1.2 Dynamic Nuclear Polarisation

Development of Dynamic Nuclear Polarisation (DNP) as a hypeprolarisation technique is connected with Albert E. Overhauser's research (in 1953)[113] . He found that microwave (MW) irradiation of electrons can enhance the NMR signal by transferring its polarisation to a target nuclear spin system. In 1956, Carver

and Slitcher gave evidence to the Overhauser effect by the first DNP experiment with observations in ^{7}Li enhancement[114] and thereafter, in 1956, in Na^{+} in NH_3 solutions.[115] The maximum theoretical enhancement for protons that can achieved is about 660 (given by the gyromagnetic ratio of γ_e/γ_{1H}).[116]

The turning point of this method was the 1997 idea of dissolution-DNP by Abragam.[117] The idea was that low temperatures can enhance polarisation. It allowed for the preserving of polarisation while transitioning between the solid and liquid state and thus generating high polarisations, of more than 10,000-fold over thermal equilibrium in several nuclei such as ^{13}C and ^{15}N.[118]

In the dissolution-DNP technique, nuclear spins are polarized in solid state at low temperatures (typically 1-2K) in high magnetic fields (3-7T). The electron spin polarization is close to unity at these temperatures and fields that are easily obtained. Nuclear spin populations are redistributed upon MW irradiation which is close to the paramagnetic resonance frequency of an unpaired electron and thereby approach those of the electrons spin polarization. It takes many minutes to hours at low temperatures to complete this transfer, but the sample can be dissolved once the solid state polarisation is high enough. The process of nuclear relaxation is relatively quick. Although the polarisation remains intact during the transition to the liquid state, the high polarisation relaxes to the thermal state of equilibrium.[119] Nevertheless, nowadays, with high signal sensitivity by dissolution-DNP, real-time metabolic flux which is linked with ^{13}C-enriched biomolecules, is practical.

Dissolution-DNP samples are prepared by dissolving ^{13}C compounds in a so called glassing matrix or solvent. The most commonly used ^{13}C-agent is [1-^{13}C]pyruvate as it relaxes relatively slowly and this long time is beneficial to assess metabolic processes. Typically, a combination two of the following solvents are used: DMSO, water, ethanol, methanol, glycerol, sulfolane, ethyl acetate depending on the solubility of ^{13}C-compound.[120] Next, a small amount of organic free radicals are added (such as the water-soluble polarising agents trityl OX063 and TEMPO).[121] The sample is then cooled down to 1.4 K. The polarisation process involves an MW source irradiating this mixture, usually at 3.35 T. As soon as the sample achieves its highest polarisation level, the mixture will be dissolved in a heated solvent (at about 200°C) where fluid transfer is driven by a high pressure (10 bar) of He gas. This HP sample will be then be ready for injection into tissues, organs of interest or in the human body for the observation of metabolic flux.[122]

Dissolution-DNP allows the production of high nuclear polarisations suitable in vivo research. ^{13}C-labelled solutions have been utilised to track “real-time” metabolic flux in vivo. Most significantly, d-DNP has been showing the high

sensitivity in increased glycolysis process which helps to diagnose, assess the tumour stage as well as its therapies.[123] Investigations using hyperpolarisation of ^{13}C allows dynamic imaging of metabolic changes that offers contrast between normal and disease tissues.[124] Moreover, d-DNP-enhanced NMR is able to increase the sensitivity on detection by 44.400 for ^{13}C solution of [^{13}C]urea.[125] As with any hyperpolarisation methods, this approach also needs long relaxation time (T_1) and in case of [1-^{13}C] pyruvate, its T_1 is about 40 s in vivo.[126] The d-DNP technique includes dissolution, injection and imaging, that is why to measure pyruvate to lactate conversion, it requires more than that time. However, since the discovering this method, there were a number of investigations on detection abnormalities within the tissues in animals[127] and humans.[128]

Measurements of early tumour responses to chemotherapy by measuring hyperpolarised [1-^{13}C]pyruvate to lactate conversion were studied, where the reaction was driven by lactate dehydrogenase as the catalyst.[129] The research has shown a decrease in the monitored flux after therapy and that the loss of NAD(H) co-enzyme pool might cause a murine lymphoma cancer cells reduction. The same tumour cells have been studied via injection of hyperpolarised [1,4-$^{13}C_2$]fumarate and it has been shown that fumarate to malate conversion might be diagnostic of cancer cell death and therefore can help monitor disease response to therapy. [130] Other research has shown that utilising hyperpolarised [1-^{13}C]pyruvate and [1,4-$^{13}C_2$]fumarate enables DNP to detect chemotherapy response in a model of human breast adenocarcinoma cancer.[131] Since many cancers are accompanied with the high rise in glucose uptake,[132] the DNP approach has been particularly applied to in vivo glycolysis reaction. The higher rate of the pyruvate to lactate pathway in tumour cells is known as the Warburg effect.[133,134] This phenomenon is explored further in the section 2.2.

d-DNP, however, has several limitations: the requirements a high sophisticated and expensive polariser, which is why it is not widespread tool to use.[135]

2.1.3 Para-Hydrogen Induced Polarisation

Para-Hydrogen Induced Polarisation (PHIP) is a rising field of research that has been shown to create 4-5 orders of magnitude of signal enhancement which is much better than the result of advances in hardware and/or imaging reprocessing methods.[136] The PHIP approach involves the correlation between parahydrogen's nuclear spins to hyperpolarise the desired molecules.[137] This method allows NMR spectroscopy to identify and characterise intermediates of catalytic processes.[138] Moreover, this method has been used in imaging and the metabolic tracking of a ^{13}C nucleus as well as other nuclei such as ^{15}N and ^{29}Si. Demonstrations of PHIP hyperpolarisation for enhanced MR signal in vivo have been recently documented.[139–141]

It builds on the fact that hydrogen exists as two nuclear spin isomers: *para*-hydrogen (pH_2) and *ortho*-hydrogen (oH_2).[142] The hydrogen atoms in a molecule of H_2 are bound together by a single σ-bond. Hydrogen nuclei contain a single fermion (proton) and possess a half-integer spin. When they combine together to form H_2, two possible spin isomers result as detailed in Figure 2.2. By the convention, when referring to alignment with an external magnetic field, spin states are represented α (parallel) or β (antiparallel). Although there are 4 simple spin state combinations, αα, αβ, βα and ββ, linear combinations must be taken for the αβ, βα forms in order to distinguish them. This is done as the linear combinations $(\alpha\beta + \beta\alpha)/\sqrt{2}$ and $(\alpha\beta - \beta\alpha)\sqrt{2}$.

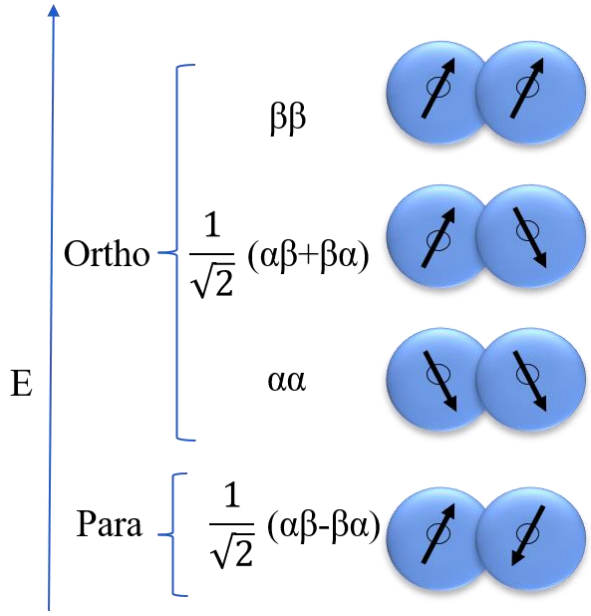

Figure 2.2. The four possible orientations of nuclear spin in a molecule of hydrogen

This reveals that we are really talking about wave functions. For a two particle system made up of identical fermions, this, total, wave function must be antisymmetric. There is no straightforward explanation for this requirement which builds from the Pauli exclusion principle which states that whenever two equivalent nuclei are interchanged, the overall wave function much change sign. This total wavefunction, ψ, though is the product of multiple parts which are distinct in energy: nuclear (discussed), translational, vibrational, rotational and electronic, as expressed in the following equation:

$$\Psi = \Psi_{\text{nuclear}}\, \Psi_{\text{translational}}\, \Psi_{\text{vibrational}}\, \Psi_{\text{rotational}}\, \Psi_{\text{electronic}} \quad (2.1)$$

The translational, vibrational and electronic functions are symmetric to particle exchange. Thus when the nuclear spins are parallel, to obtain an overall wavefunction with different sign, the rotational form should change sign.

Consequently, if the spins are paired parallel, $\Psi_{rotational}$ is symmetric. That is to say, for the parallel state, there must be an odd rotational quantum number (*J*) value while for an antisymmetric spin state there must be even values. In these cases, similarly as described above, what is known as the *ortho* isomer's spin state needs quantised angular momentum values of J = 1, 3, 5, 7, etc. to acquire an antisymmetric wave function. The singlet $(\alpha\beta - \beta\alpha)\sqrt{2}$ state in what is *para*-hydrogen is antisymmetric, and so only even numbers (0, 2, 4, 6, etc.) for $\Psi_{rotational}$ are allowed. Since singlet hydrogen has the lowest potential energy, it is the most stable spin isomer of hydrogen. It should be noted that it is not difficult to enrich hydrogen in the *para*-form, because of the large energy gap (0.34 kcal mol^{-1}) between J = 0 and J = 1 rotational spin states.

At room temperature, the ratio between *ortho/para* forms of hydrogen is therefore about 3:1. However, by lowering the temperature, the enrichment of hydrogen in the *para* isomer is favoured.[143] However, formally interconversion between these isomers is forbidden, that is why the enrichment reaction is catalysed by a paramagnetic substance such as iron(III) oxide. By reaching set-point temperature at ~20 K (the boiling temperature of hydrogen) under an iron oxide catalyst, hydrogen gas in the *para* state will be generated at almost 99% purity. After the conversion step, *para*-hydrogen in gaseous state can be warmed to room temperature in the absence of a paramagnetic catalyst and stored for weeks or months as it is stable to spin-reequilibrium.[144] Consequently, a key benefit for PHIP and SABRE is that *para*-hydrogen can be generated by relatively easy and at low-cost.

As the *para*-hydrogen nuclei' spins are opposed (↑↓) and cancel each other out, it has a net magnetic moment of zero; therefore, pH_2 is NMR silent. Nevertheless, there are chemical processes that convert this spin order to the enhanced NMR signal by destroying its symmetry before detection. Commonly, this is achieved by molecular-hydrogen addition to unsaturated but magnetically/chemically non-equivalent parts of an acceptor molecule and this produces a visible hyperpolarised molecule.[145] These reactions are often referred as hydrogenative PHIP (hPHIP). D.P. Weitekamp and C.R. Bowers reported the theory underlying this in the late 1980s and a year later they provided experimental evidence using the catalyst ($RhCl(PPh_3)_3$ - tris(triphenyl-phosphine)rhodium(I)chloride) for hydrogenation reaction of acrylonitrile.[146] In this reaction, the propionitrile product and the hydride regions of the active catalytic meionites showed the large signal. In 1987, Richard Eisenberg and his colleagues observed the great sensitivity in the detection of catalytically significant hydrides by the hydrogenation of phenylacetylene with $[Rh_3Cl_2H_2(CO)_2((Ph_2PCH_2)_2PPh)_2]^+$ as a catalyst.[147]

To understand these experiments' results we need to refer to Boltzmann distribution (the energy difference between the populations). By the equation 1.4, considering normal H_2, there is only 1 in 32,000 protons can be detected in at 9.4 T (400 MHz) as all four isomer states have relatively small energy gap between each other. If we look at the Figure 2.3, it shows changes in these energy levels in the presence of magnetic field. Hydrogenation reaction with normal hydrogen results in distribution of hydrogen protons (*ortho* and *para*). When protons are transformed to a molecule (hydrogenation of unsaturated bond), they are no longer chemically equivalent. This causes the αβ and βα spin state terms to be distinct and is revealed as two doublets.

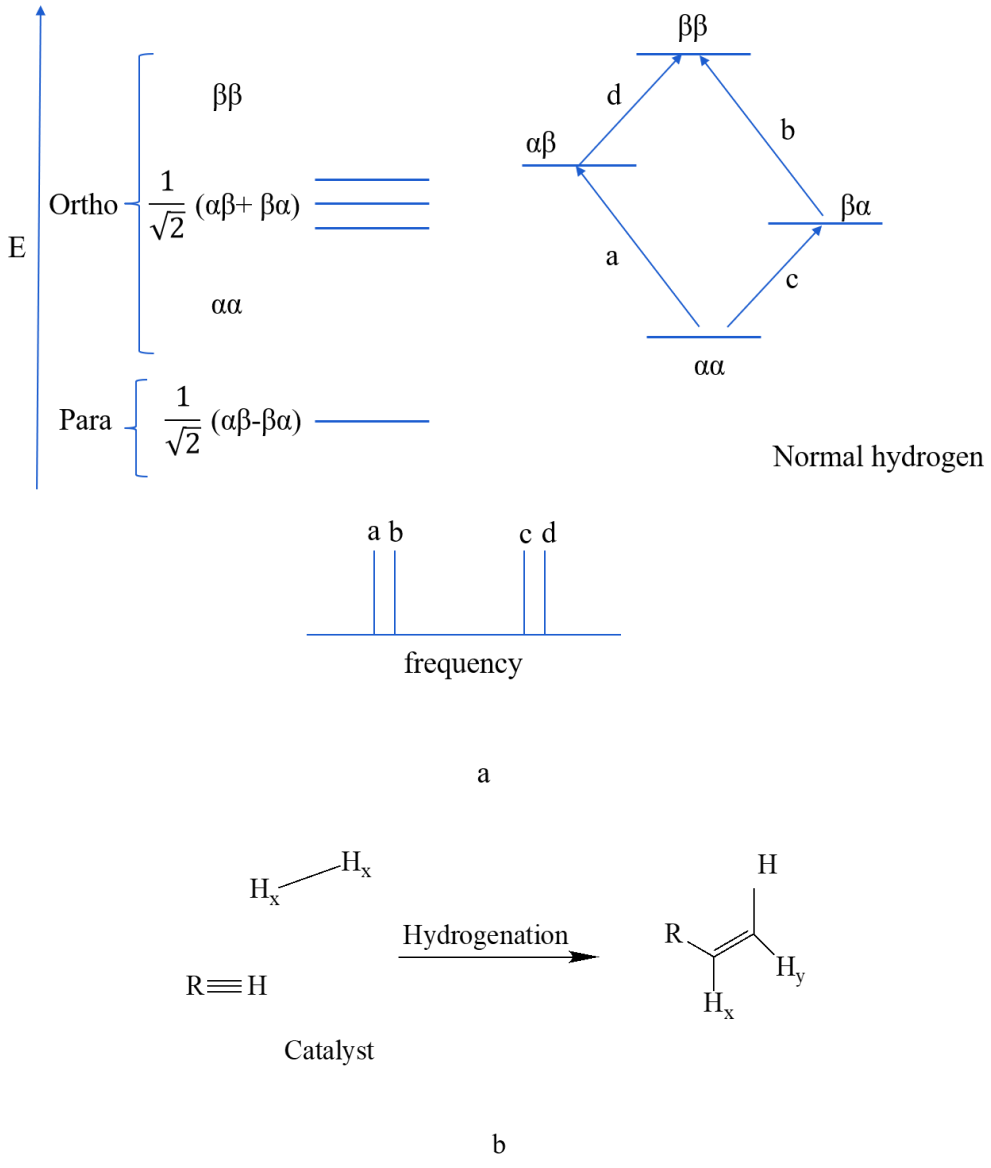

Figure 2.3 (a). Changes in the energy levels are showing the four possible spin states of hydrogen after hydrogenation. a, b, c and d transitions are represented by arrows; (b) H_{2x} spin system is added to unsaturated compound (hydrogenation reaction) by evolving to H_x and H_y.

In the case of *p*-H_2, two types of experiment can be considered: PASADENA and ALTADENA. These two methods' are differentiated by the magnetic environment during *para*-hydrogen addition. These methods are summarised in Figures 2.4 and 2.5. It can be concluded that the detection and the usage of the enhancement derived from *para*-hydrogen requires breaking of the added hydrogen atoms' equivalence. The first method that is described in this section is *para*-hydrogen and synthesis allow dramatic enhancement of nuclear alignment (PASADENA). This approach utilises p-H_2 derived protons who end up at magnetically inequivalent sites on the substrate molecule whilst under the high field of the NMR spectrometer.[147] A large signal enhancement in the NMR spectrum makes it possible to observe intermediate species during this step, their spatial configurations, and hydrogenation reactions kinetics in the liquid form. In the PASADENA method, only the αβ and βα spin states of the products *p*-H_2 derived protons are populated if the initial spin configurations symmetry is maintained (Figure 2.4).

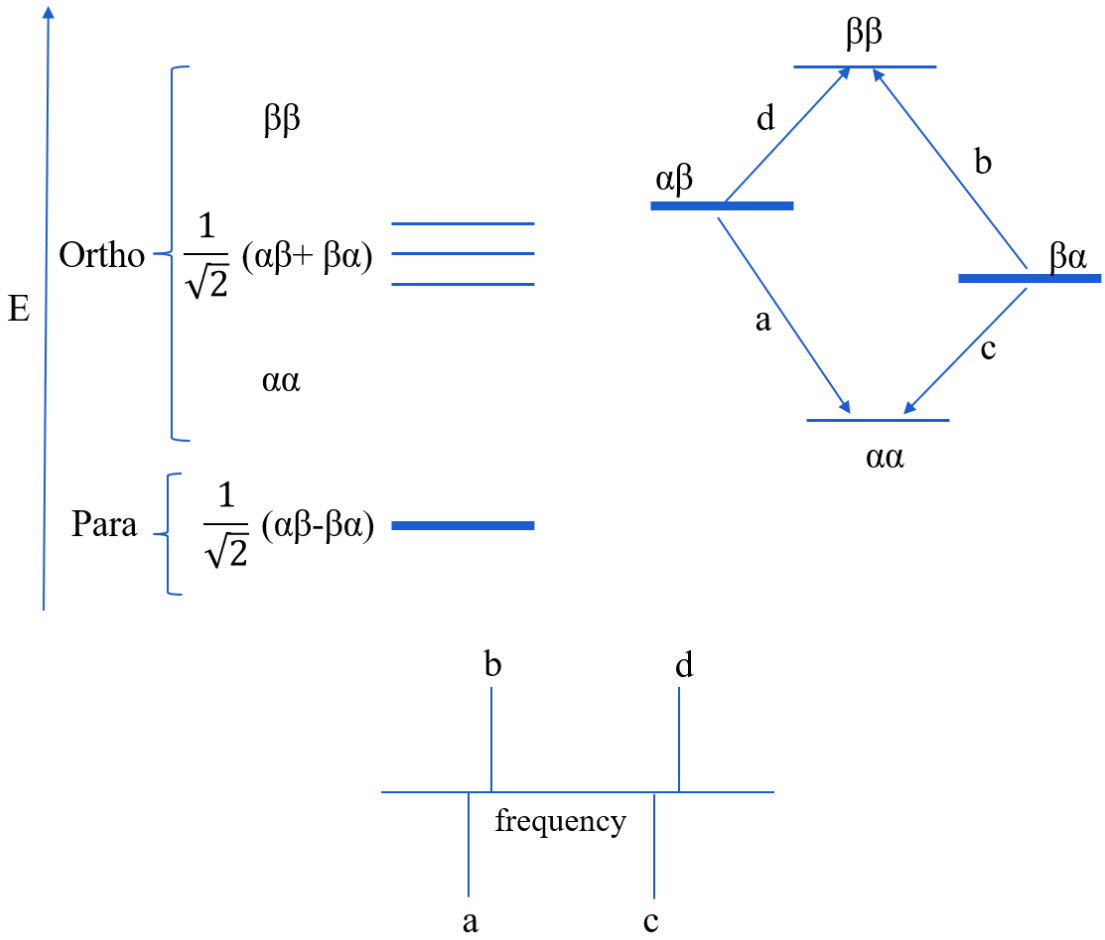

Figure 2.4. Changes in the energy levels of the spin states of *para*-hydrogen at high magnetic field. a, b, c and d transitions are represented by arrows (at the top); Proton NMR spectrum of the enhancement by PASADENA effect (at the bottom).

The PASADENA method therefore gives rise to anti-phase (opposite amplitudes) doublets in the NMR spectra of the products. Since there are a great population difference, these two lines at each chemical shift are extremely enhanced.

Generally, the adiabatic longitudinal transfer after dissociation engenders nuclear alignment (ALTADENA) experiment is similar to the previous one (PASADENA), but instead of high magnetic field, the reaction takes place at low fields.[148] However, this is followed by a subsequently changing to high magnetic field as the sample is inserted into the NMR. The effect is completely different as we can observe in Figure 2.5. At low magnetic fields, there is a great effective coupling difference between spins. This process is followed by adiabatically transitioning the product to high magnetic field. In this step, the occupation of only a single spin state within the product molecule is observed. Overpopulation of βα or αβ states at high filed results according to the sign of the *J*-coupling constant. Therefore, b and c transfers will be possible and the spectrum includes two lines in emission (spin "up") or absorption (spin "down"). (Figure 2.5).

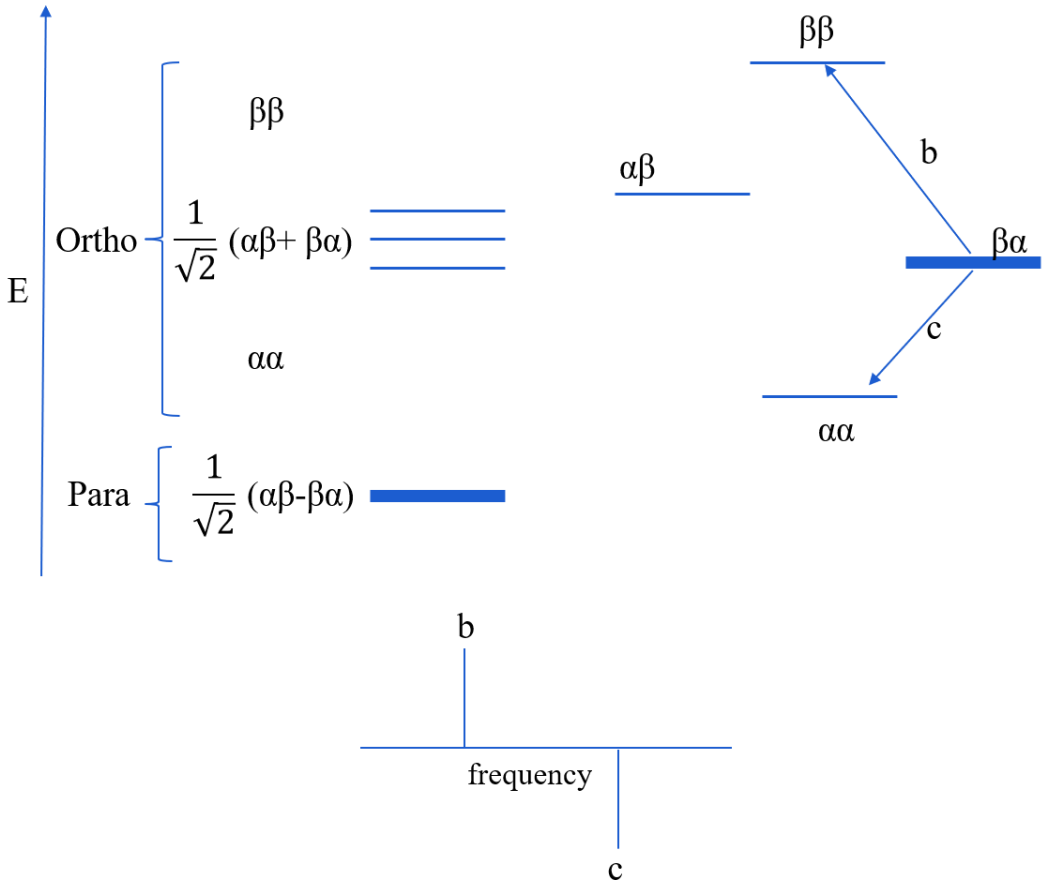

Figure 2.5. Changes in the population of the spin states of *para*-hydrogen at low magnetic field. The polarisation of a spin system (βα) after adiabatic transition of the product from low to high magnetic fields (at the top); Proton NMR spectrum of the enhancement by ALTADENA effect (at the bottom).

These approaches (PASADENA and ALTADENA) have several disadvantages:

- in the hydrogenated product, when the atoms of *para*-hydrogen occupy equivalent positions, their symmetry is preserved and a signal cannot be detected. So, an unsaturated PHIP substrate is only applied with appropriate assymmetry. For instance, in a hydrogenation of magnetically equivalent protons in symmetric molecules, the enhancement can be observed as result of a formation of an asymmetrical intermediate or the breaking of symmetry by coupling with ^{13}C atoms.
- due to the need to add *p*-H_2 pairwise to the substrate, the choice of catalyst is generally limited. Specifically, homogeneous catalysts, such as Wilkinson's[149] or the Crabtree[150] catalyst, are possible used. The reaction is primarily driven by the Horiuti-Polanyi mechanism;[151] thus, heterogeneous catalysts like palladium on charcoal are ineffective. Some exceptions have also been noted[152], and PHIP catalysis has been shown when nanoparticles are capped with ligands.[153]
- the short longitudinal relaxation time is also one of the main drawbacks. The reaction rate must be fast and therefore, there is a need of extremely active catalysts; moreover, the products and intermediates' longer relaxation times are beneficial for the enhancement and the detection. These limitations in catalytical reactions, their mechanisms and kinetics have been studied by Duckett S. B. and co-workers.[154,155]
- it is also essential that *p*-H_2 is incorporated into a molecule through a chemical hydrogenation process. For this technique, the substrate must contain an unsaturated bond and therefore limits the substrate scope.

Molecular tags with unsaturated functionality that could be cleaved were developed to avoid these limitations. Para Hydrogen Induced Polarization Side Arm Hydrogenation (PHIP-SAH) was introduced to identify metabolites of vital biomolecules (for example, pyruvate).[156] Particularly, the first experiment utilising the PHIP-SAH hyperpolarised [1-^{13}C]pyruvate *in vivo* has been demonstrated. It has shown metabolic flux of pyruvate to lactate by detecting the response of the heart to altered metabolism in real time.[157] Researchers found that heart muscle metabolic dysfunction occurring as a result of dilated cardiomyopathy may be detected by comparison of ^{13}C label exchange rates between pyruvate and lactate. The usage of a magnetic field cycle for polarisation transfer from the *para*-hydrogen protons to the ^{13}C carboxylate spin provided a 6.2 ± 0.3% increase of the ^{13}C in the carboxylate signal of allyl-pyruvate. The carboxylate's ^{13}C's longitudinal relaxation time was measured as 68 ± 0.5 s which was viable to detect its signal in vivo by MRI system. The diagram of chemical pathway of this process and the images taken from this experiment will be shown in the 2.4 Pyruvate metabolism section.

2.1.4 Signal Amplification by Reversible exchange

The modification of a target structures chemical identity through a hydrogenation reaction is one of the main limitations of the PHIP method.[158] The one feasible solution for this can be the recently provided using a PHIP method called Signal Amplification By Reversible Exchange (SABRE). This was first demonstrated by Duckett S.B. and co-workers in 2009, who showed that the polarisation via *para*-hydrogen can occur without any chemical modification of the hyperpolarised material.[159]

2.1.4.1 Basic Principles

SABRE is based on the reversible binding of *p*-H_2 and the substrate to an octahedral iridium organometallic catalyst (which is a magnetisation transfer) in solution (Figure 2.6). Consequently, the *p*-H_2 derived hydrides are no longer chemically or magnetically equivalent, thereby breaking the symmetry in a *p*-H_2-nascent proton pair. The spin polarisation can be delivered spontaneously from the *p*-H_2 to the ligated substrates (for example, pyridine) via the scalar coupling of the iridium catalyst at low magnetic field. In the presence of an excess of substrate, bound polarised ligands constantly exchange with the free agent, giving rise to rapidly building up solutions of hyperpolarised agent. Moreover, in contrast with hydrogenative PHIP, SABRE provides multiple polarisation of substrate after relaxation thanks for reaction's reversibility and this does not allow the enhancement to be lost.[160]

The information about NHC (N-heterocyclic carbene) ligand with IMes which is shown in the following diagram, will be described in details in the Section 2.1.4.3 Chemistry of SABRE.

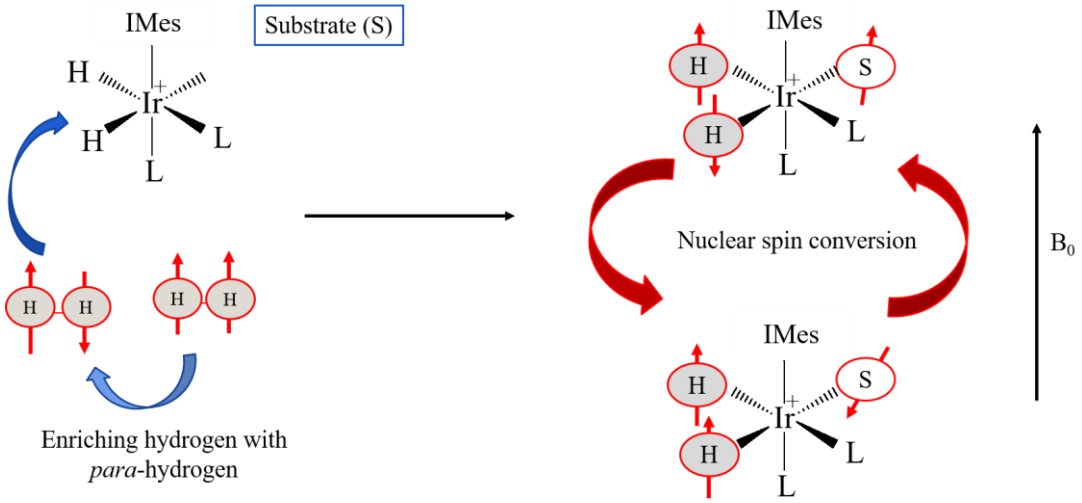

Figure 2.6. Schematic representation of hyperpolarization transfer from *para*-hydrogen-derived hydrides to a nuclear spin of substrate (represented as "S") through an Ir-based organometallic catalyst.

2.1.4.2 Instrumentation

The most commonly used SABRE catalysts are of the type [Ir(COD)(NHC)Cl] (where NHC = N-heterocyclic carbene and COD = cycloocatdiene). These are typically not sensitive to air and they are usually stored under room atmosphere. All procedures before NMR experiments are performed in situ. First of all, the iridium catalyst and substrate are dissolved in an organic solvent (for instance, methanol). Afterwards, a sample is placed into a 5 mm J. Young's tap NMR tube. The solution is degassed using a high vacuum Schlenk line techniques and the NMR tube is subsequently filled with *p*-H_2 (4 bar). The NMR tube then is forcefully shaken for 10–20 s in order ensure the *p*-H_2 is able to freely exchange into solution. This manual shaking happens in a low magnetic field, typically, in the stray field of the NMR magnet. In order to detect the sample and obtain a spectrum, the sample is placed into an NMR tube in an NMR spectrometer and integrated by RF pulses. In some experiments, an automated process might be applied using an NMR flow system.[161]

2.1.4.3 Chemistry of SABRE

There are a number of chemical aspects of the SABRE method that can be understood and therefore optimised:

- hydrogen and the polarised substrate should be able to exchange with the free substrate and fresh *p*-H_2 from the polarisation transfer complex. This requires a complex of suitable stability.
- the stability of this complex should be related also to the period of time of the experiment.
- magnetic equivalence of *para*-hydrogen protons should be destroyed via the orientation and shape of the catalyst complex.
- this complex's lifetime should be similar to the inverse of the spin-spin coupling ($1/J$). Owing to relaxation time, very long lifetimes could cause loss of hyperpolarisation, whereas short lifetimes do not allow *para*-hydrogen protons to transfer the polarisation.

In order to fit all the requirements, a number of research steps were taken.

The first complex that matched these SABRE requirements was reported to be Crabtree's catalyst, [Ir(COD)(PCy_3)S]BF_4 (COD is *cis,cis*-1,5-cyclooctadiene, Cy is cyclohexyl and S is pyridine). This catalyst was originally discovered and studied for hydrogenation reactions.[162] In SABRE, the catalyst is activated by exposing to hydrogen and excess amount of pyridine; as a result, an octahedral complex, [Ir(PCy_3)S_3($H)_2$] BF_4 is formed.[159,163]

Michael J. Cowley et al. (2011) reported an improved type of catalyst system containing an N-heterocyclic carbene (NHC) ligand.[164] Since then NHC ligands such as [Ir(IMes)(COD)Cl] (IMes is 1,3-bis(2,4,6-trimethylphenyl)-imidazol-2-ylidene and COD is cyclooctadiene) have been used widely to produce SABRE active catalysts. It is hypothesised that the increase in polarisation transfer is due to the effect of superior steric and electronic properties. For example, NHCs are strong electron donors.[165] [166] Also, the dependency of the hyperpolarisation levels rise on the lifetime of the metal complex over which polarisation transfer takes place.[167] This was experimentally confirmed by Lyrelle S. Lloyd and co-workers.[168] They have shown that for iridium complexes with NHC ligands react with *para*-hydrogen and pyridine and give an optimal ligand exchange process.

One commonly used NHC ligands, [Ir(SIPr)(COD)Cl] (SIPr = 1,3-bis(2,6-diisopropylphenyl)-4,5-dihydroimidazol-2-ylidene), and its reaction with H_2 and substrate is shown in Figure 2.7. These reactions occur by cycle (known as catalytic cycle), where spin polarisation is transferred to a target analyte. To begin with, polarisation transfer from *para*-hydrogen derived hydride ligands to the hydrogen nuclei in an analyte will occur. This analyte then unbinds from the complex, providing a vacant site for hydrogen atoms, so para-hydrogen-derived hydride ligands can be replaced. Oxidative addition of the incoming dihydrogen molecule and reductive elimination of the pre-existing hydride ligands, enables a pyridine ligand to bind so that the process can begin again (Figure 2.7).[169]

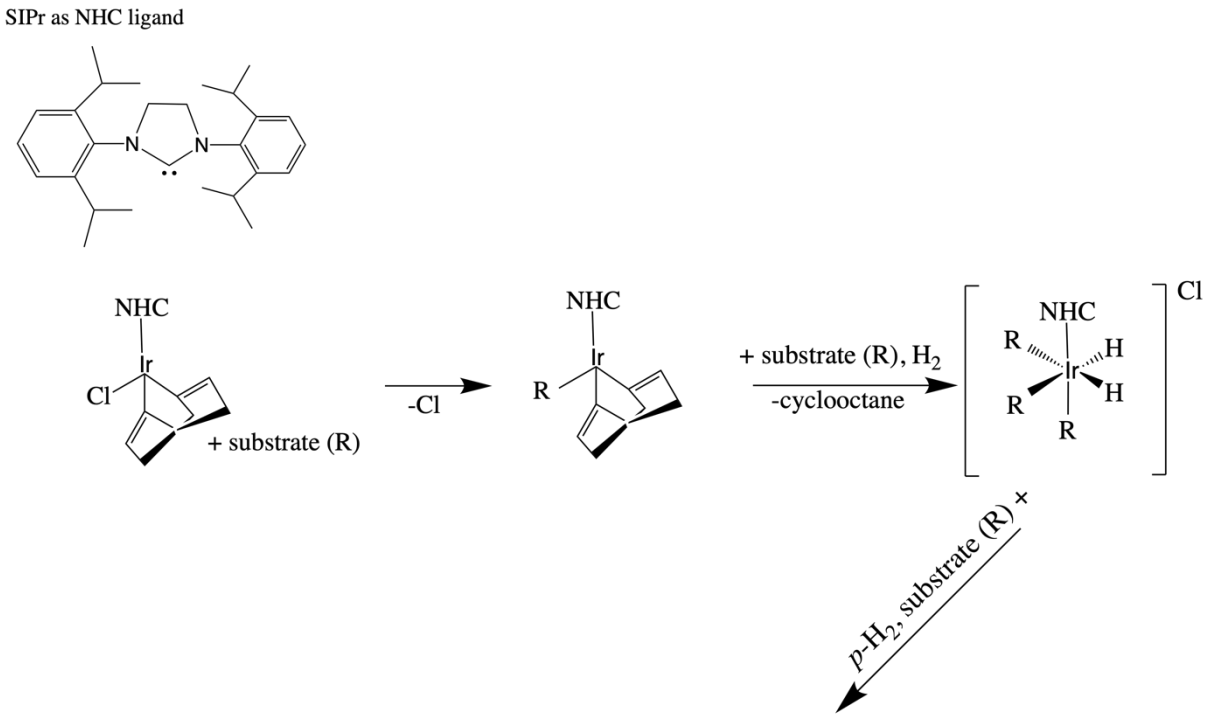

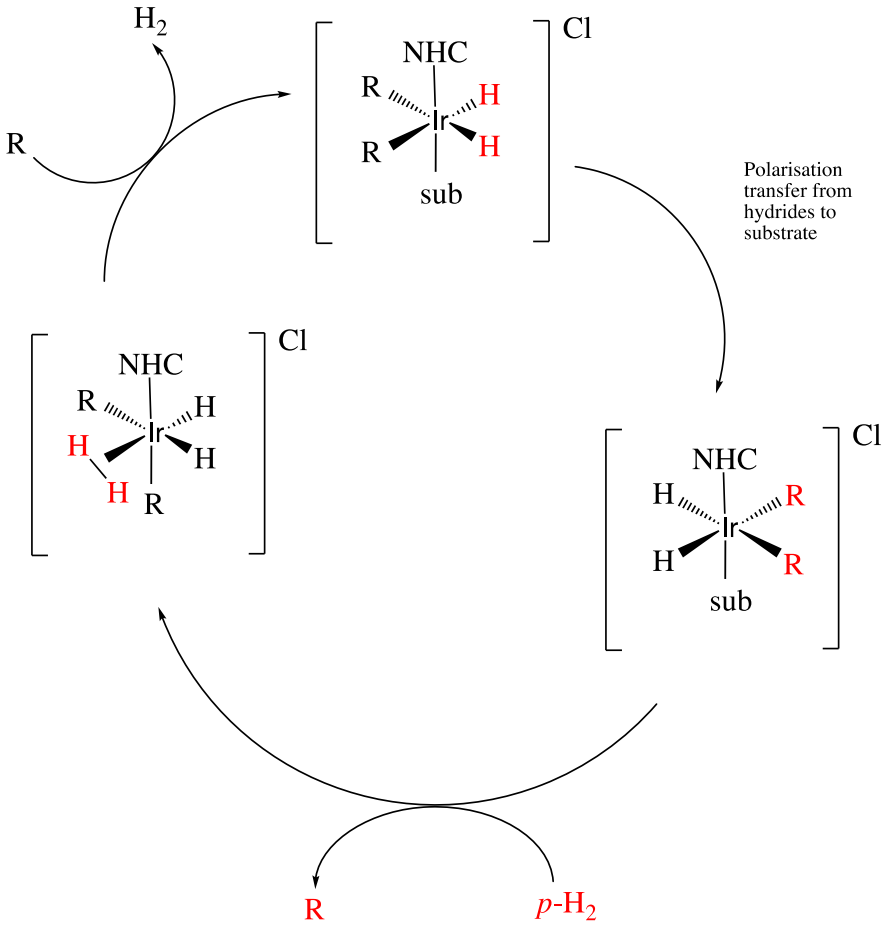

Figure 2.7. The process of the formation of SABRE catalyst complex with hydrogen via hydrogenation of COD ligand. In this hyperpolarisation method, catalyst binds reversibly to *p*-H_2 and target molecule(s). Reversibility of SABRE enables regeneration of the chemical exchange through continuing supply of fresh *para*-hydrogen. In this diagram SIPr as NHC ligand is illustrated.

2.1.4.3.1 Design of the catalyst

Since the SABRE catalyst enables a cyclic reaction to transfer polarisation, the ligand structure around Iridium is crucial in providing analyte binding to the metal centre. During the catalytic cycle, there must be enough empty sites for the binding of analyte and parahydrogen-derived hydride ligand. Moreover, the overall architecture of the catalyst must enable the complex to exchange hydride ligands and analyte molecules freely at a metal centre. Initially, iridium complexes with phosphine ligands were studied.[170,171] As it has been long known that a phosphine or carbene ligands behave differently when their substituent groups are changed.[172,173] The most studied factors that affect to the exchange rate have been ligand electronic and steric effects. Electrons moving along chemical bonds result in an electronic effect, whereas non-bonding forces between ligands cause steric effects. It was observed that electron rich and most sterically demanding phosphine PCy_2Ph provided the highest enhancement of the three ^1H

sites of pyridine,[171] presumably due to varied exchange rate. It is the most electron rich and most sterically demanding ligand among investigated series of molecules (Figure 2.8.) to form the SABRE complex $[Ir(PR_3)(py)_n(H)_2][BF_4]$.

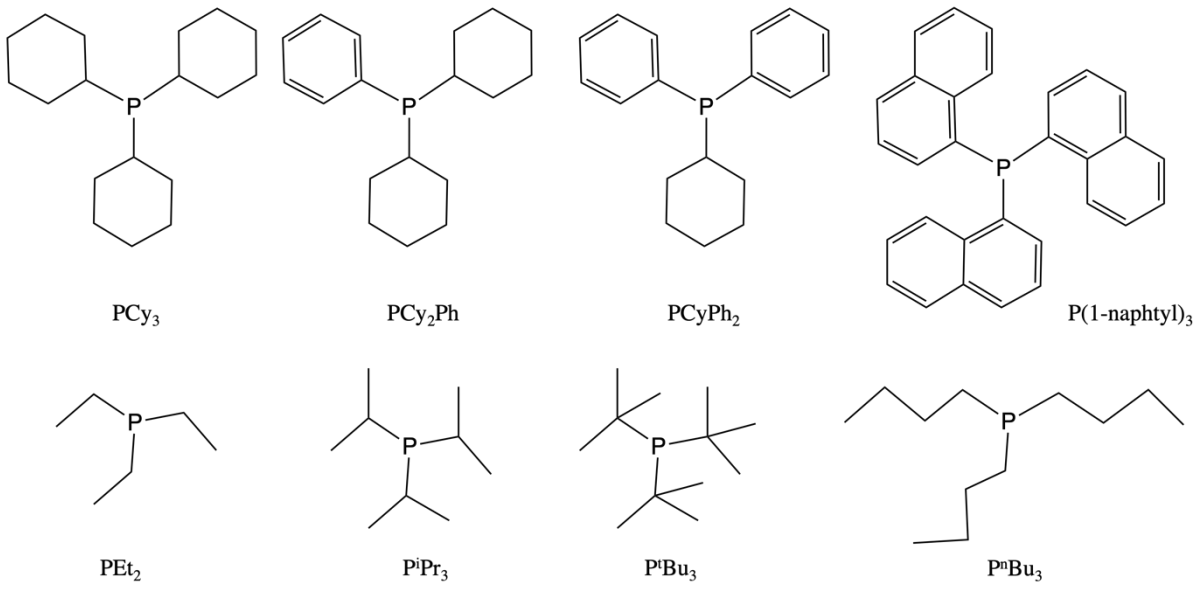

Figure 2.8. Chemical structures of the phosphines that were utilised to form SABRE complexes by Kevin D. Atkinson *et al*.

After assessment of the phosphine ligands for electron density and steric properties, which influence to the SABRE enhancement, carbene chemistry, which is also might affect the polarisation transfer, has been established.[174–176] As it was previously described, the first carbene complex in SABRE was focused on IMes in the complex [Ir(IMes)(COD)Cl]Cl. And the derived signal from the meta nuclei of analyte (in this case, pyridine) increased by 266-fold, while an analogous phosphine complex provided only 18-fold enhancement.[164] By convention, the electron donation characteristics of ligands are measured by the Tolman Electronic Parameter (TEP),[177] which is related to weakening the CO bond and therefore lowering the carbonyl stretching frequency measured via infra-red (IR) spectroscopy. The second property, the steric factor, is usually quantified using the volume of a sphere centred on the metal of various NHCs (V_{Bur}, %).[178,179] However, the group of C.Feiters (van Weerdenburg, B. J. A. et.al)[175] studied the structures of the NHCs in order to obtain the best possible signal enhancement, which obviously have shown that electron donation properties by the TEP and actual SABRE hyperpolarisations demonstrate no correlation. Although they bore no correlation with the TEP, they have observed that pyridine's exchange rate increases with the growing steric bulkiness. There have been various iridium carbene complexes studied (Figure 2.9) related to the polarisation process of pyridine. The highest enhancement up to 680 was observed with pre-catalyst IMes; associated polarisation level was 1.11%. Further

research has demonstrated similar 1.16% polarisation levels of the NHC ligand with IMes.[164] The saturated analogue SIMes performed the second highest signal enhancement at 369-fold. The inclusion of an alkyl groups instead of aromatic groups of the NHC has led to a considerable decline of the enhancements to lower than 100-fold. Table 2.1 illustrates the correlation between the enhancement and the electron donating properties of studied NHC ligands.[175,180,181] Although the unsaturated ligands of NHCs have more electron donating properties than their saturated analogues, the difference in donation between the two substituent pairs (mesityl and diisopropylphenyl) is not seen. That is to say, electronic effects among various catalysts have small influence on the polarisation level.

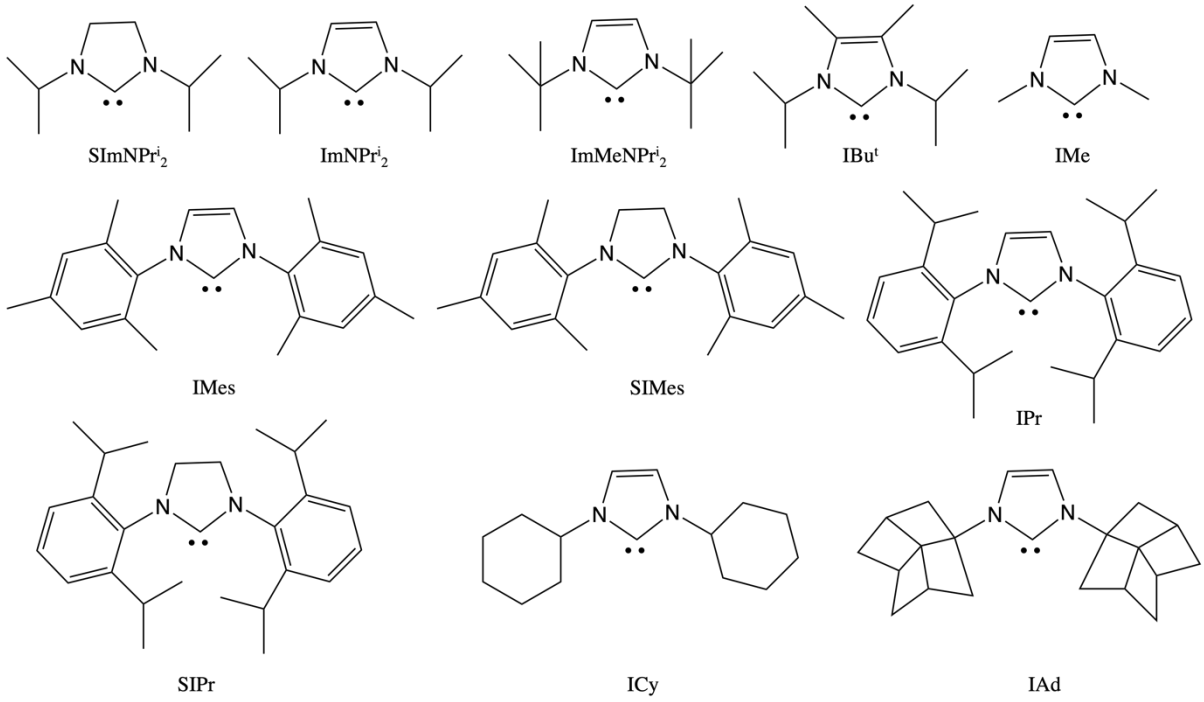

Figure 2.9 Ligands used for the SABRE experiments by C.Feiters and co-workers.

Table 2.1 The comparison between the obtained signal enhancements, the Tolman Electronic Parameter and steric properties of the NHC ligands.[175,180,181]

NHC ligand	TEP value (cm^{-1})	Buried volume (V_{Bur}, %)	Signal enhancement factor at 200 MHz (pre-polarisation field about 80 Gauss
SImNPr	2024.5	28.5	43
ImNPr	2024.1	26.4	72
SIPr	2024.9	35.7	103
IPr	2023.9	33.6	125
SIMes	2024.6	32.7	369
IMes	2023.1	31.6	680
ICy	2023.0	27.1	18
ItBu	2022.3	35.5	11

On the other hand, steric parameters might have more effects on the signal enhancement. It was concluded that the unsaturated samples which are showing higher enhancements, have less bulkiness than their saturated counterparts (Table 1.2). It is noteworthy that the enhancement factor is also affected by exchange rate constants between the target analyte and H_2 as it was demonstrated by a dissociative mechanism.[164] Saturated NHCs tend to have considerable higher exchange rates, which depicts that the larger steric bulk – the higher exchange rate (Table 2.2). However, having a moderately slower exchange rate and buried volume, the unsaturated ligands demonstrate the higher signal enhancements. This indicates that for successful polarisation, the optimum value of exchange rate is required.

Table 2.2 The comparison of the exchange rate of pyridine, buried volume of NHCs and the signal enhancement.[175]

NHC ligand	Buried volume (V_{Bur}, %)	Exchange rate of Py (s^{-1})	Signal enhancement factor at 200 MHz (pre-polarisation field about 80 Gauss
SImNPr	28.5	28.5	43
ImNPr	26.4	26.4	72
SIPr	35.7	35.8	103
IPr	33.6	33.6	125
SIMes	32.7	32.8	369
IMes	31.6	31.7	680
ICy	27.1	27.1	18
ItBu	35.5	35.5	11

In this thesis, unsaturated and saturated NHC ligands' properties which linked to the signal enhancements were observed. In the Results and Discussion section **(Chapter 5)**, the connection between exchange rate, V_{Bur}, % and the electron richness will be considered.

PHIP does not provide the route where the pyruvate molecule has available unsaturated precursor that can be hydrogenated. Therefore, an alternative route has been developed to prepare hyperpolarised pyruvate in aqueous solutions. It involves the side arm that is quickly hydrogenated and consequently hydrolysed.

The work in this report based on the non-hydrogenative PHIP derived signal amplification by reversible exchange (SABRE) process to hyperpolarise of pyruvate. This approach has achieved considerable levels of polarisation in materials that bind by nitrogen centres to a metal catalyst for polarisation transfer, without altering the chemical identity of pyruvate.

Using SABRE, p-H_2 binds to a transition metal centre to form a dihydride complex which polarises the nucleus if the hydrides that receive the polarisation are different (Figure 2.10).[182]

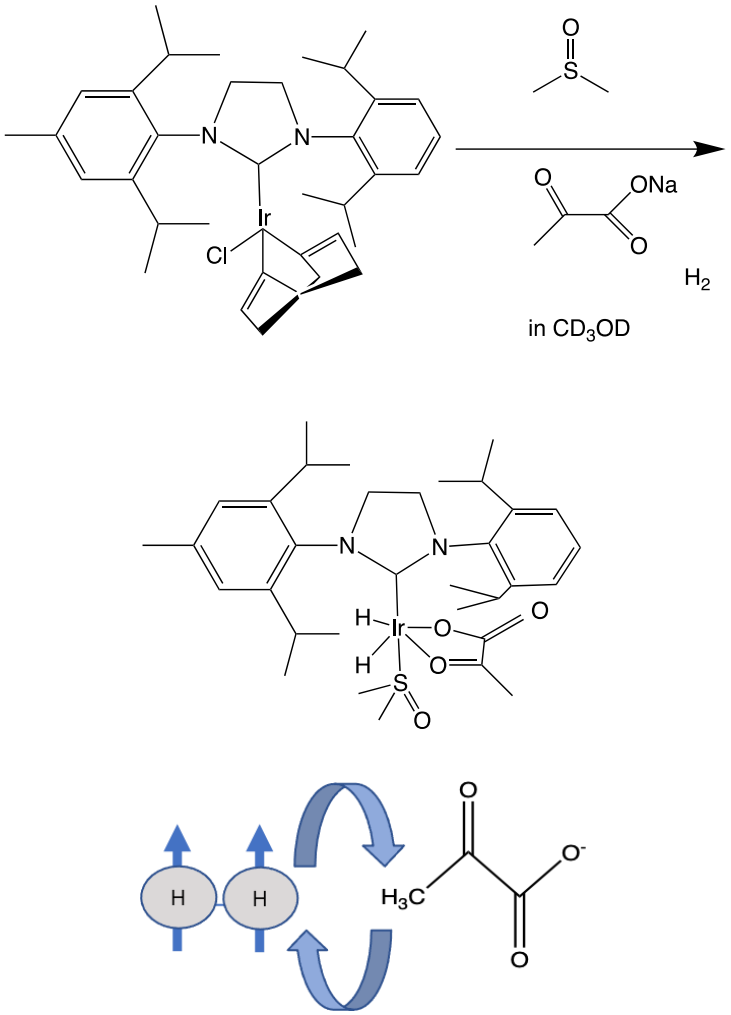

Figure 2.10. Schematic representation of the SABRE hyperpolarisation process, where pyruvate is hyperpolarised by catalyst $[Ir(H)_2(pyruvate)(DMSO)(SIPr)]$.

It can be seen from Figure 2.7 that the original SABRE catalyst has the form $[Ir(H)_2(NHC)(sub)_3]Cl$ and is therefore charged. Both hydride ligands are chemically identical being *trans* to sub, but they are magnetically distinct by virtue of the *cis*/*trans* coupling pathway across the metal centre into sub. This complex is also charged and consequently, the SABRE process is dramatically affected by solvent. More recent results (Duckett and Fekete) have demonstrated that in none polar solvents like dichloromethane, the actually form of the catalyst changes to neutral $Ir(H)_2(NHC)(sub)_2Cl$. Now the hydride ligands are *trans* to halide and sub and therefore both chemically and magnetically distinct.

It is the size of the propagating hydride-substrate coupling that determines the speed of magnetisation transfer, and this depends on the nature of the substrate, the form of the catalyst and its ligands, and the number of bonds between the interacting groups. For example, for pyridine, the coupling is ~1.2 Hz and therefore an optimal lifetime of 0.25 s has been suggested. However, for ^{15}N the resulting 2-bond coupling is much higher and a 22 Hz value appropriate. This

would mean that the optimal lifetime of the interaction reduces to around 10 ms and thus a completely different catalyst is needed. One further way to control this behaviour is to change temperature, while another is to change the solvent. However, in protic solvents, hydrogen isotope exchange confuses the situation as this leads to deuteration of suitable protons within the substrate in solvents like methanol-d_4.

2.1.4.4 Physics of SABRE

SABRE catalysts must have a sufficient lifetime in order to ensure that efficient polarisation transfer has occurred. Accordingly, a scalar coupling must occur between the hydride ligands and the target spins in the bound substrate whose reciprocal is large when compared to the relative rate of ligand loss. In order to obtain optimal catalysis, the polarisation transfer field (PTF) must also reflect the matching condition that is associated with polarisation transfer.[183] The optimum magnetic field for polarisation transfer to ^{1}H, ^{13}C, and ^{15}N nuclei is relatively low in magnitude, and when matched it allows the transition of spin order from para-hydrogen derived protons to, for example, pyridine with approximately 100-fold ^{1}H NMR signal enhancements.[164]

In the beginning of the SABRE process, *p*-H_2 is free and in the singlet state and can be represented by a density matrix. Following binding of the *p*-H_2 to an Ir based complex its behaviour may be described by the Liouville-von Neumann equation.[167] The density matrix's evolution is analysed mathematically by applying operators to the Hamiltonian. Hamiltonian theory considers a time dependent Larmor frequency, time-independent/field-independent scalar couplings between proton nuclei and the resulting evolution. As a result of these calculations, it was proven that under spin-spin coupling between these in equivalent hydrogen nuclei transfer of polarisation is possible through the magnetically-active nuclei of the SABRE complex. However, these works did not consider optional ligand exchange and multiple visits to the catalyst where long effective lifetimes result. Hence this approach could be further investigated.

In contrast, the next approach provides for a greater understanding of mechanisms of polarisation transfer in SABRE process and utilises Level Anti-Crossings (LACs). Based on the strength and frequency of B_1 fields, it can be useful to predict which spin orders will be transferred.[184] Generally, the complex spin dynamics can be uncovered with the LAC concept, and can be used to optimise the performance of hyperpolarisation methods. LACs arises at magnetic fields where two energy levels tend to approach or cross; however, owing to spin-spin coupling the level crossing point is lifted and there will be no crossing.[185] In relation with this avoidance, the theory is named "anti". LACs provides information on field areas where there is the possibility of the coherent mixing

between spin states. The efficient mixing is crucial as the polarisation transfer is highly dependent on it.

LACs can also explain the SABRE effect through the typical NMR parameters of the complex: two spins are considered weakly coupled if the difference in their precession frequencies, $\Delta\nu$, exceeds greatly the spin-spin coupling, J, between them. This is the so-called AX-spin system. The opposite to the AX system is an AB-system (strong coupling limit), where the coupling J strength exceeds or is similar to $\Delta\nu$. An A_2 system, as in H_2, arises in case of exceedingly small $\Delta\nu$.

Since now eigenstates are a mixture of both spins, an AB-system has properties that are very different from those of an AX-system. In low-field where $J >> \Delta\nu$ case, the two states of an AB-system become S and T_0 states. Whereas, in high-field where $J << \Delta\nu$ case, these are now the $\alpha\beta$ and $\beta\alpha$ states seen under Pasadena. Consequently, during spin mixing at low field, both spins' energy become close; and they are no longer polarised independently but together. This strong coupling enables polarisation transfer between them at the low field.

These considerations using LACs allows:

- to identify the magnetic fields where SABRE polarisation's characteristic features appear;
- to understand the spin dynamics and to formulate sign rules for the expected polarisation;

Furthermore, performing the LAC analysis is not particularly challenging from a computational standpoint, as it only requires diagonalising of the SABRE complex's Hamiltonian. To conclude, LAC provides the methodology of coherent polarisation transfer fields' models and allows SABRE for the efficient and selective spin mixing. Despite the effectiveness of these calculations, LAC needs further study as to estimate the polarisation transfer field needed for unstudied ligands practical measurements are necessary. These must define the chemical shifts and couplings that operate within the bound complex. Even if both exchange effects and relaxation are mapped, a fully defined understanding of the process is still hard to achieve as H_2 exchange is itself impossible to model to the level of accuracy needed from NMR alone as it involves an invisible dihydride-dihydride whose dynamics are ambiguous at best. Hence the prediction of precise enhancement levels goes far beyond current models.

Based on what has been discussed, it is important to know that the magnetic field dependence derived from SABRE may be estimated by polarisation transfer processes. However, there is not only dependency of SABRE on magnetic resonance characteristics, but also on the chemical characteristics' such as

kinetics of the exchange reactions. In this thesis the rate of reactions is discussed widely as it is crucial for predicting and explaining the lifetime of the substrate on the complex catalyst. This time has to match to the time period of building-up of polarisation and to avoid this polarisation loss within longitudinal relaxation time. Recently, the investigations on the parameters that might affect the rate of exchange processes have been illustrated. Studies on the exchange rates of the bound ligand with free ligand using various temperature and substrates,[163] different concentrations of ligands and reagents,[164] also *p*-H_2 concentrations' changes[168] have proven the dependency of the exchange rate on these conditions. In addition, it has also been shown that polarisation transfer might be influenced by the time taken to transfer the sample to the magnet (the polarisation transfer time)[168] and the magnetic field where the sample is shaken (the polarisation transfer field).[186] Different iridium *N*-heterocyclic carbene complexes have been synthesised and examined for efficient SABRE catalysis. Nevertheless, each unstudied carbene ligand and even substrates that have been analysed require considerable studies of certain conditions for SABRE efficiency.

2.1.4.5 Studies in SABRE

In the past decade, SABRE has provoked at a lot of interest in the research community. There have been a number of demonstrations for efficient strategies to develop polarisation levels and also, methods for polarisation of SABRE catalysts in the NMR machine have been developed. In this thesis the research that have utilised SABRE polarisation particularly in biologically relevant substrates are focused on.

To start with, studies of biologically relevant substances, especially in *vivo* is always strongly linked with the pharmaceutical industry. This industry is widely discussed in corporation with Process Analytical Technology since its official introduction in the USA.[187]PAT in this guidance was defined as "a system for designing, analysing, and controlling manufacturing through timely measurements (i.e., during processing) of critical quality and performance attributes of raw and in-process materials and processes, with the goal of ensuring final product quality". The technology may utilise NMR spectrometers to monitor reactions, optimisation of synthesis and controlling of quality at industrial level (as reviewed by A. S. Rathore).[188] For these purposes, 7 T to 23 T NMR spectrometers have high potential, the big size and the high price, however, unable their applications.[189,190] That is why low-field and compact NMR instruments allows monitoring and controlling of the reactions at the manufactures. On the other hand, these spectrometers exhibit an inherently poor sensitivity in the detection. This limitation is typically related to low concentrations of samples.

The practical way to solve this issue might be the hyperpolarised NMR techniques.[191–193] For example, the recent study in 2020 showed that the products obtained by esterification of glycine were also active in SABRE at 60 MHz and thus giving possibilities for using that to study organic reactions with glycine; also opening the way of discovery drugs and monitor their pathways.[194] The clinical treatment for coronavirus pneumonia worldwide (COVID-19) has been studied using this hyperpolarisation technique. Antiviral drugs such as chloroquine, hydroxychloroquine, ritonavir, lopinavir, and favipiravir were successfully tested at various magnetic field's strength including Earth's magnetic field.[195] Their target isotope labelled ^{13}C and ^{15}N molecules were monitored. About 2 years ago, a signal enhancement via SABRE was illustrated on hydrogen protons, where the polarisation increased to approximately 3.3% over the Earth's magnetic field in *situ*.[196]

Since SABRE was discovered, the study of various biological NMR active nuclei have been shown. The method was initially focused on ^{1}H polarisation.[57,159,197–199] If we look back to the Table 1, hydrogen-1 has the highest natural abundance and the highest gyromagnetic ratio and by putting these numbers to the equation 1.2, it is clearly seen that NMR sensitivity depends on these characteristics. They allow NMR hyperpolarisation methods, especially SABRE, to reach high enhancement levels. Furthermore, unlike biological agents with the nuclei such as ^{13}C-labelled or ^{15}N-labelled, hydrogen-1 does not need costly labelling; and most of these agents have hydrogen atoms inside their molecules. In MRI considerations, ^{1}H coils are standard on all scanners and therefore they are available on all clinics, unlike the coils which are based on ^{13}C, ^{23}Na or ^{31}P, which are not provided by the manufacturer and require to be ordered separately making the procedure more expensive.

Hyperpolarisation by SABRE has mainly utilised nitrogen-containing heterocyclic compounds due to activity, efficiency, economic and environmental scope.[200] Nitrogen has lone pairs and donation by the lone pairs is can stabilize the SABRE catalyst making them effective ligands.

To illustrate, the report has shown the importance of hyperpolarising the sites adjacent to the nitrogen centre of pyridine in efficient polarisation transfer.[201] Other studies have shown the signal enhancement of drugs that are effective for the treatment of tuberculosis. [170] Other various biologically relevant molecules such as amino acids, peptides,[202] amines,[203] and other drugs[204–206] have been hyperpolarised. The detailed characteristics which make pyridine rings play a vital role in drug motifs are explained in some review articles.[207,208]

2.1.4.5.1 SABRE at high field

It has already been described in this chapter (section 2.1.4.2 Instrumentation) that polarisation transfer usually occurs at low magnetic fields followed by transferring the sample to high magnetic fields where detection and measurement happens. Theoretically, the studies on this process have initially shown that based on all known parameters (magnetic and kinetic), the SABRE effect may be estimated by the reported theory.[167] However, this theory might not be suitable practically and thus the SABRE effects will not be precisely forecast. To describe the optimal magnetic-field regions the LAC concept can be used as it was previously discussed in the section 2.1.4.4 Physics of SABRE. By Pravdivtsev,[209] this theoretical approach based on LACs might be able to define optimal value of the prepolarisation field and the hydrides spin-spin coupling in the SABRE complex identifies the efficiency of polarisation transfer. In 2015, the combination of LACs and analysis of SABRE parameters (concentrations of the catalyst, pH_2 and substrate; *J*-couplings; the relaxation and reaction's kinetics) gave a formula that might be useful to design optimal system for SABRE experiments.[210] Pravdivtsev *et al.*[211] has also investigated the application of RF fields in high field SABRE, which has shown fast transfer of the *para*-hydrogen spin order by carefully setting the amplitude and frequency of the RF field. However, therein, the NMR enhancements are 100-fold for a range of substrates at 4.7 T have been observed. That is to say, the enhancement was lower than magnetic field cycling approach.

Another high field SABRE method is ADAPT-SABRE (ADAPT= alternating delays achieve polarisation transfer). SABRE hyperpolarisation of ^{15}N spin-1/2 heteronuclei was illustrated using this method.[212] There has been produced approximately 3 orders of ^{15}N signal enhancement in 1.6 s of RF pulsing. The method might be easily adjust for any NMR active nuclei (for instance, ^{13}C, ^{19}F and ^{31}P), which requires optimal field for efficient spin mixing weaker than the earth's magnetic field due to the huge difference in chemical shift between the hydrides and these heteronuclei.

There are several benefits of high field methods over the low-field SABRE process: RF-SABRE allows NMR to generate hyperpolarization in a continuous way with high efficiency[211] and ADAPT method provides constant field shuttling and losing of unnecessary signal during transport.[212] However, these methods require further investigations to achieve in *vivo* SABRE-MRI hyperpolarisation rather than sample testing.

Another high field magnetic methodology was introduced in 2014 which is widely known as LIGHT-SABRE (LIGHT = Low Irradiation Generation of High Tesla).[213] This method works with simple pulse sequences and very low power

deposition. It can produce high polarisation transfer at any magnetic field considering chemically equivalence and magnetically inequivalence of the *p*-H_2.

2.1.4.5.2 Hyperpolarisation of heteronuclei by SABRE

Whereas the proton is the most common SABRE nucleus of interest, the polarisation transfer has also been utilised for X nuclei (^{13}C, ^{19}F, ^{31}P, etc.). These nuclei can either be directly polarised by coupling to the hydride ligands in the catalyst or indirectly by intramolecular transfer from hyperpolarised ^{1}H resonances.

Following up on the first Nitrogen-15 under SABRE by Duckett et al in Science, the method was refined in 2015 by Theis *et al.*[214] They demonstrated efficient polarisation transfer to ^{15}N in pyridine (Py) and nicotinamide (vitamin B_3 amide) at micro-tesla magnetic fields. The enhancement achieved was 30,000-fold when measured at 9.4 T, corresponding to a polarisation induction of 10%. In these experiments, free ^{15}N-pyridine molecules' spectral pattern was shown clearly, emissive in-phase triplet due to strong ^{2}J-coupling between ^{15}N in the enriched substrate and the ortho-Py-protons. The method is commonly known as SABRE-SHEATH (SHEATH= in shield enables alignment transfer to heteronuclei, which may be beneficial to polarise heteronuclei as it is straightforward and inexpensive way. ^{15}N polarisation is found to be useful for in *vivo* research owing to the longer hyperpolarisation lifetimes in contrast to ^{1}H nuclei, absence of background signal, and wider chemical shift discrimination.[215] Hyperpolarization on ^{15}N has few important limitations as well. For example, the low natural abundance of this isotope (Table 1) requires the high-cost enrichment of the agents. In addition, the ten times lower gyromagnetic ratio (Table 1) in comparison with ^{1}H results in low detection sensitivity.[216]

The high field approaches in hyperpolarisation have been promising usage in *vivo* as well. The pharmaceuticals imidazole has been polarised reaching the signal enhancement of 2,000-fold at 9.4 T using SABRE-SHEATH. The conditions used are highly expected to be biocompatible in terms of pH sensing.[217] This method also has enabled ^{15}N hyperpolarisation of metronidazole up to 24% showing high potential in applications in vivo imaging to monitor mechanisms of activity or hypoxia sensing.[218] Biomolecular imaging with hyperpolarized diazirines has been studied to develop their biocompatibility and providing establishment for real-time in *vivo* imaging.[219,220]

The hyperpolarisation of ^{13}C by SABRE has been less popular and challenging in comparison with d-DNP studies, which is currently the leading technique on hyperpolarisation of that heteronuclei. The approach of SABRE has achieved the 116-fold signal gain,[221] while DNP is able to reach over 10,000-fold

enhancements with 37% polarisation for carbon-13 nuclei.[125] However, DNP requires long polarisation times, they can be last hours; moreover, this method is costly. If considering the high field method of SABRE in enhancement of ^{13}C enriched samples, SABRE-SHEATH has proved 10-fold enhancement of ^{13}C isotope nuclei in pyridine at 9.4 T.[222] The highest polarisation level of ^{13}C heteronuclei was achieved by Barskiy and co-workers in 2017 using micro-Tesla SABRE. This efficient polarisation was about 4.4% and 6700-fold of enhancement in the test molecular framework-pyridine-^{15}N using SABRE-SHEATH experiments.[223]

In 2021, a temperature cycling method for SABRE-SHEATH was introduced that enables 10 per cent polarisation on [1-^{13}C]pyruvate. This enhancement has high probability of successful usage in *vivo* experiments and can be combined with inexpensive MRI systems to achieve a broadly available, yet highly sensitive metabolic imaging platform.[224] Initially, at lower temperatures, ~20% polarisation is achieved on pyruvate which is bound to SABRE-catalyst, afterwards pyruvate is released into free form in solution at elevated temperatures. The first ^{13}C pyruvate images with a cryogen-free MRI system operated at 1 T was illustrated by these scientists.

Discussing about pyruvate images using SABRE approach, all α-keto acids were incompatible with that hyperpolarisation method until 2018. SABRE hyperpolarisation of molecules such as pyruvate had limitations, one of them the poor iridium and pyruvate ligation.[182] The new method which is called SABRE-Relay has been illustrated the potential to extend SABRE approach to a wide range of biologically relevant molecules, that are not amenable to the traditional SABRE hyperpolarization route.[225–227] These methods use chemical exchange pathways to cascade polarisation into substrates via a coherent carrier. To illustrate, approximately 109-fold signal enhancement of ^{13}C in ^{13}C-labeled sodium pyruvate was achieved by this methodology.[227] However, pyruvate rapidly condenses with the amine carrier to form products [$Ir(H)_2(\eta^2$-α-carboxyimine(amine)(NHC)], which deactivate the system, leading to further pyruvate polarisation.[228] To overcome that limitation, suitable ligands which stabilise the SABRE complex and consequently, strengthen pyruvate's weak ligation to iridium have been studied (see in the following section).

2.1.4.6 Pyruvate as the substrate of interest in this thesis

Given the success of d-DNP for the application of hyperpolarised pyruvate, a significant breakthrough in the SABRE method came with the report of SABRE hyperpolarisation of ^{13}C labelled pyruvate.[182] Up until this point, α-keto acids were not thought to be amenable to the SABRE method due to the weak ability of them to bind to iridium centres.

This new method, coined SABRE-Relay, has illustrated the potential to extend the SABRE approach to a wide range of biologically relevant molecules, that are not amenable to the traditional SABRE hyperpolarization route.[225–227] SABRE-Relay uses chemical exchange pathways to cascade polarisation into substrates via a proton transfer agent. To illustrate, approximately 109-fold signal enhancement of ^{13}C in ^{13}C-labeled sodium pyruvate was achieved by this methodology.[227] However, under these conditions, which typically involve a primary amine, pyruvate rapidly condenses with the amine to form products like [Ir(H)$_2$(η^2-α-carboxyimine(amine)(NHC)], which deactivate the system, leading to no further pyruvate polarisation.[228] Thus, in order to overcome this limitation, an alternative approach was sought.

It was hypothesised that utilising a co-ligand in conjunction with an iridium catalyst and sodium pyruvate may lead to the formation of a suitable SABRE catalyst.[229] Co-ligands had previously been widely used to improve polarisation outcomes in a number of other substrates.[182,230] The requirements for the co-ligand were that it would not be able to fully outcompete the binding of pyruvate to the metal centre, whilst also providing suitable electronic stabilisation of the catalyst. It was found that the co-ligand dimethyl sulfoxide (DMSO) fulfils this role and provided a highly enhanced NMR spectrum of pyruvate.[182] The active complex was characterised to be [Ir(H)$_2$(η^2-pyruvate)(DMSO)(IMes)] in this process. These novel sulfoxide containing SABRE polarisation transfer catalysts exhibit rapid hydrogen exchange which give strong SABRE hyperpolarisation.[231]

In 2021, a temperature cycling method for SABRE-SHEATH was introduced that enables 10% polarisation on [1-^{13}C]pyruvate.[224] This enhancement has high probability of successful usage for in *vivo* experiments and can be combined with inexpensive MRI systems to achieve a broadly available, yet highly sensitive metabolic imaging platform. Initially, at lower temperatures, ~20% polarisation is achieved on pyruvate when bound to SABRE-catalyst, afterwards pyruvate is released into free form in solution at elevated temperatures. The first ^{13}C pyruvate images with a cryogen-free MRI system operated at 1.5 T was illustrated by these scientists (TomHon et al. 2021).[224]

In this research project the hyperpolarisation of sodium pyruvate via SABRE is considered in detail. Whilst SABRE has predominantly focused on pyridine and its derivatives,[232] the application of this method to polarise biologically relevant substrates such as nicotinamides and methyl nicotinates,[233] pyrazine, nicotinate and pyridazine,[234] vitamin B3[235] and pyruvate is clearly an important ambition.

The early work in York examined C_1, C_2 and C_1,C_2 pyruvate. Pyruvate-1,2-[$^{13}C_2$] was the target substrate here as we can use this approach to create singlet pyruvate, whilst understanding how best to enhance this material. It might be

expected though that the C_1 form would be the easier substrate to select though as there will be a simpler spectrum due to the missing J_{CC} scalar coupling and the T_1 is longer due to reduced dipole-dipole coupling to the neighbouring ^{13}C. We expect these results to port directly to this material. It is worth remembering, that during anaerobic conditions associated with cancer, there is high conversion rate of pyruvate into lactate, giving a way to diagnose abnormal cellular function through a hyperpolarised response.[236] This effect will be discussed in the section 2.2 Pyruvate metabolism. The SABRE hyperpolarisation methods are being tested in clinical trials to diagnose cancer by magnetic resonance imaging,[237–241] giving a huge advantageous promise to studying metabolic function in real time. If the SABRE hyperpolarisation of pyruvate can be developed to comparable levels as d-DNP then its route to the clinic is already defined. Furthermore, SABRE has the advantage of the ability to produce rapid, continuous levels of polarised agent.

2.1.4.7 The aims of the thesis and its structure

This thesis outlines studies of the imaging potential of SABRE hyperpolarised $^{13}C_2$-pyruvate.

Methods for the optimisation of the catalytic reaction for pyruvate are developed and applied. I aimed to quantify both T1 relaxation time and overall signal enhancement as a function of various NHC ligands (IMes, SIMes, IPr, SIPr) present in the sample, pyruvate's concentrations and the temperature at which the measurements were obtained on the level of delivered hyperpolarisation.

It is important that these parameters are quantified to assess whether necessary time delays between preparation and detection will compromise final signal detection. By developing optimised methods with increased magnetic state lifetimes and highest polarisation gains, signal detection will be possible over a longer time frame and can provide significant advantages for tracer analysis and metabolism.[230]

Chapter 3 describes Pyruvate metabolism within the cell cytoplasm and mitochondrial matrix (i.e. importance for the tricarboxylic acid cycle). Moreover, the Warburg effect, a modified form of glycolytic flux that offers a route for cancer diagnosis with hyperpolarisation is also discussed. In this chapter, longitudinal relaxation time (T1), the importance of its determining and extending are detailed. **Chapter 4** provides methods for errors calculations; **Chapter 5** provides observations of experimental results and their analysis; estimates potential future works to improve these measurements, biocompatibility, and imaging of pyruvate using SABRE method.

Chapter 3. Pyruvate and cancer

3.1 Pyruvate metabolism

Pyruvate is an essential molecule in eukaryotic and human metabolism. Pyruvate is the final product of glycolysis. It is produced in the cell cytosol. It is then transferred into mitochondria where through oxidation processes it fuels the citric acid cycles carbon flux.[242] Consequently, pyruvate is crucial to the synthesis of mitochondrial ATP and plays critical role in several biosynthetic pathways that intersect with the TCA cycle (Figure 2.8).

Cytosolic pyruvate molecules are generated from several sources. In most differentiated cells, pyruvate is converted from glucose,[243,244] where pyruvate kinase catalyses phosphoenolpyruvate (PEP) and Adenosine diphosphate (ADP) to pyruvate and Adenosine tri-phosphate (ATP). The process generates 2 molecules of ATP and two molecules of pyruvate from one molecule of glucose. Pyruvate could also be formed from lactate by lactate dehydrogenase (LDH) and from the catabolism of alanine by alanine aminotransferase (ALT).

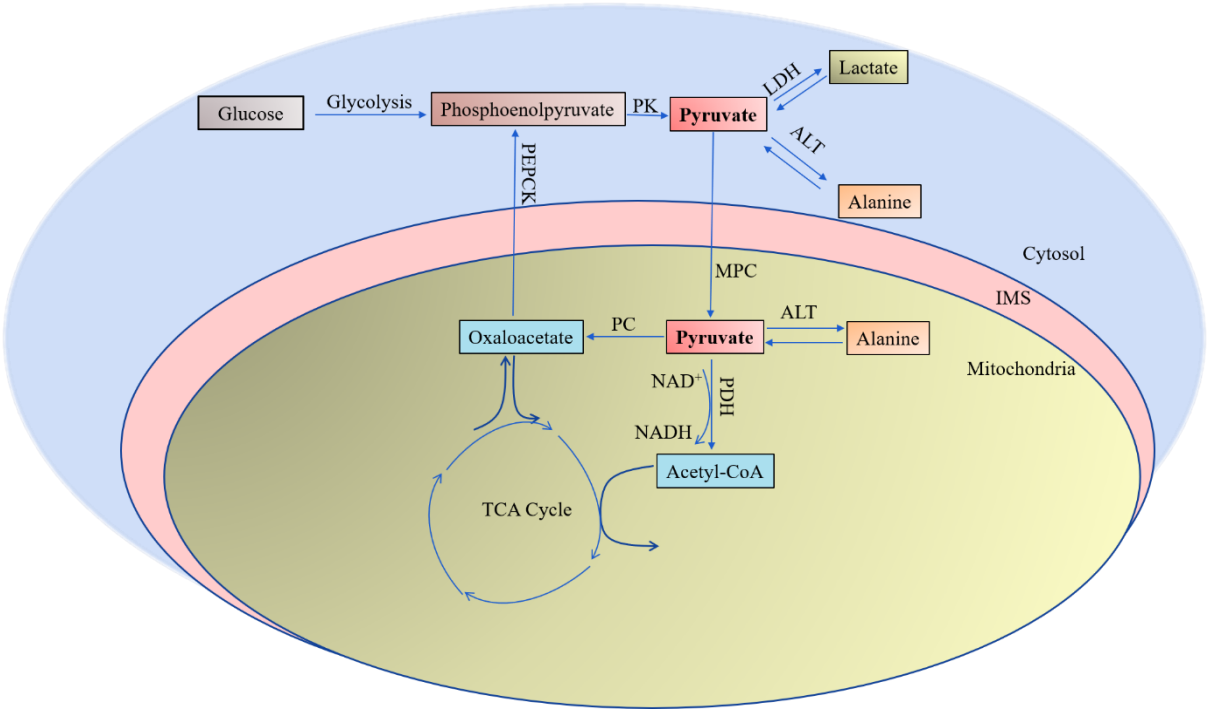

Figure 3.1. The overall mechanism of Pyruvate metabolism. The final step of glycolysis using PK yields molecules of pyruvate. Pyruvate is also produced from the oxidation of lactate by LDH or the transamination of alanine. Pyruvate then is into the mitochondrial matrix via the MPC. Once in the mitochondria, pyruvate can be converted to acetyl-CoA via PDH or oxaloacetate. Pyruvate and names of related metabolites as well the enzymes are illustrated.

The pyruvate kinase reaction is strongly favourable because PEP is the most energy rich phosphometabolite.[245] The dephosphorylation of

phosphoenolpyruvate to pyruvate is an irreversible reaction which forms two molecules of pyruvate with two net molecules of ATP. Therefore, glycolysis is the main metabolic pathway for energy generation. Particularly, this process is critical in the maintenance of erythrocytes' cell functions during intense period of work. Due to the lack of mitochondria and nuclei, red blood cells are not able to generate energy (in this case, ATP) by oxidative phosphorylation to power muscle contraction.

Once produced in the cytoplasm, pyruvate is mostly imported into the mitochondria. This entry to the mitochondria from the mitochondrial intermembrane space is accompanied with the recently discovered mitochondrial pyruvate carrier (MPC).[246,247]

In the matrix, pyruvate depending on the microcellular environment, has several metabolic routes. However, most of pyruvate under aerobic conditions is oxidised to CO_2 by the Krebs cycle to support the ATP production by oxidative phosphorylation. First of all, pyruvate (and NAD^+ (nicotinamide adenine dinucleotide)) in oxidative tissues is irreversibly converted into acetyl-CoA (and NADH (reduced nicotinamide adenine dinucleotide)) by the pyruvate dehydrogenase complex (PDH) complex. Acetyl-CoA then enters the citric acid cycle by releasing carbon dioxide molecules in the reaction. The conversion of pyruvate to carbon dioxide generate energy which is used to produce the reducing equivalent NADH and FADH2. By entering the electron transport chain 32 ATP molecules per a molecule of glucose are generated by these reducing equivalents. This electron transport chain needs oxygen to accept an electron in the final step, called oxidative phosphorylation. NADH and FADH2 play a crucial role in the generation of the proton gradient required for oxidative phosphorylation and ATP production.

Pyruvate can also be converted by pyruvate carboxylase to oxaloacetate (OAA) in the matrix as well. Oxaloacetate can afterwards enter the tricarboxylic acid cycle or be decarboxylated and phosphorylated to produce phosphoenolpyruvate via phosphoenolpyruvate carboxykinase (PEPCK).

Overall, the process of oxidation of glucose following by pyruvate metabolism in the mitochondrial matrix generates 36 molecules ATP, consequently, being the main energy source for eukaryotes' cells.

Since this thesis is focused on pyruvate to lactate conversion, it is relevant to note that detailed information about the metabolic pathway in the mitochondria matrix can be read in referenced articles and reviews.[242,248,249]

In addition to entering the matrix for use as a substrate in the TCA cycle, pyruvate is converted to lactate or ethanol by fermentation processes in normal mammalian tissues under anaerobic conditions. The pyruvate to lactate conversion is not a direct energy source for tissues, however, the reaction regenerate NAD^+ by oxidising NADH. As it was previously mentioned above, during intense workouts, the muscles require a large amount of ATP as energy in the absence of oxygen. That is to say, ATP is used up during exercise and the muscle cells cannot provide oxygen for respiration, consequently NADH accumulates. So, regeneration of NAD^+ here is essential to continue glycolysis undergoing and producing more ATP. To supply NAD^+, pyruvate is converted into lactate by accepting electron from hydrogen proton in NADH. Although this reaction generates only two net molecules of ATP, it is a fast and relatively efficient in terms of short-term energy aims. The chemical reaction associated with lactate production is illustrated below (Figure 2.9).

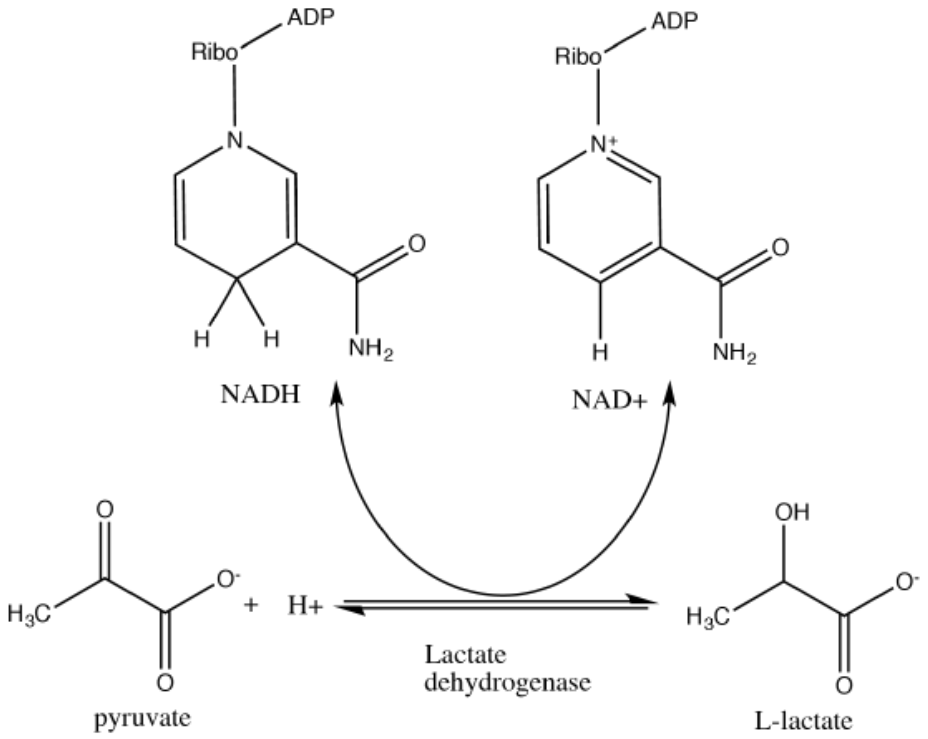

Figure 3.2. The pyruvate to lactate conversion. During this process NAD^+ is produced by the oxidation of NADH.

These reactions occur in the absence of oxygen and that is why the process is called anaerobic glycolysis. Until recent times, the product of fermentation, lactate has been identified as a waste product of this reaction, and hyperlactatemia has been linked to several diseases, such as sepsis and septic shock.[250,251] However, last few decade's of study have demonstrated that lactate might be utilised as a preferential energy source in brain interstitial tissue, especially, it might able to affect positively on cerebral energy metabolism injured human

brain.[252] Moreover, it was reported that a rise in extracellular lactate levels is beneficial for long-term memory generation,[253] ability to act as a neuroprotective substrate against excitotoxicity,[254] and for evoking glucose-sparing responses.[255] Lactate's potential neuroprotective characteristics have been illustrated and proven *in vivo* and therefore, it is clearly seen that it has more positive roles than a metabolic waste product.

The analysis of these metabolic fluxes provides precious information on biochemical mechanisms and their abnormalities which are led by many diseases. The next section will discuss the effect of these abnormalities on the earlier described pathways which are caused by oncogenes.

3.2 Warburg effect

3.2.1 Nature of metastatic inefficiency

Tumour metastasis is a multiple stage process where malignant cells spread from the original tumour to distant organs of the human body. This metastasis is the main reason of cancer mortality and morbidity. The successful development of tumour cells requires a completion of a series of sequences and then a cancer will be detectable. The metastasis cascade involves the following common steps:[256]

- the detachment from the main cancer tissues;
- invasion of the host tissue towards lymphatic or blood vessels;
- intravasation through penetration the vessel walls and entry into the circulatory system;
- spreading through the bloodstream as single or clumps form cells, which are known as circulating tumour cells (CTCs);
- arrest in the vessel's beds of the target organ;
- extravasation into the organ;
- colonisation of extravasated cells and proliferation.

Some clinical experiments have observed that the patients with initial stage of the breast cancer demonstrate tumour progression have been spread before the first diagnosis.[257] It has been shown that CTC is an essential prognostic factor of many types of cancer, especially at completed metastatic points.[258–260]

The research of the breast cancer in *vivo* has demonstrated that 1-4 million cells are able to shed from a lesion into the vessels every 24 hours.[261] There are studies that suggest cancer shells are shed actively[262–264] and/or passively.[265,266] It is possible for cancer cells in the host tumour to actively invade vessels. Moreover, abnormal angiogenesis, arteriogenesis and venogenesis can cause the tumour secretion to become unbalanced and leaky, allowing cancer cells to escape.[267]

It is rather common for cancer cells to enter the bloodstream; however, their presence does not necessarily indicate metastasis. Successful metastatic processes are caused by only a small percentage of these cells. Most of the CTCs in the blood and organs are quickly eliminated and poorly used as evidenced by an experimental metastasis model in mice. In 2 weeks time, viable cancer cells could be observed only in the lungs.[268] Using real time in vivo observations, proportions of survived B16F1 melanoma cells after injection has been determined.[269] In the liver model, only 3.5% of lesion cells survived in the form of micrometastases in the third day; 1 per cent of them then proved to evolve to macroscopic form in two weeks, while the rest stayed as dormant cells.

3.2.2 Warburg metabolism

Coming back to anaerobic glycolysis, almost 100 years ago Otto Warburg assumed that tumour cells obtain the energy for their growth and proliferation by respiration and fermentation.[134] It was hypothesised that tumour cells, even in the available amount of oxygen, have high rates of glucose consumption and lactate excretion; that results in dysfunctional of mitochondria metabolism.[133,270] Under intensive growth of cancer cells and providing a microenvironment for their growth, pyruvate is readily converted to lactate via LDH in the cytoplasm rather than undergoing oxidation in the mitochondria. This results in losing the tight connection between the citric acid cycle and glycolysis. The phenomenon is known as aerobic glycolysis or the "Warburg effect". This effect is a common term which is directly related to a cancer trait, that empowers diagnosis and treatment.

Although glycolysis processes produce only two molecules of ATP, defining it as a less efficient metabolism in terms of energy, these processes are chosen by cancer cells for proliferation. All proliferating cells adapt to facilitate the uptake and incorporation of nutrients to biomass (e.g., synthesis of amino acids, lipids and nucleic acids) which result in cell division and growth (Figure 2.10). So, oncogenic tissues' proliferation demands are more than satisfied with intermediates and glycolytic metabolites during the pathway of Warburg metabolism.[271]

3.2.3 Cancer metabolic heterogeneity

Since discovering of Warburg effect, many results have been re-examined for Warburg's observations which illustrated that mitochondrial metabolic capacity is not diminished and the high aerobic glycolysis is not the dominant metabolic pathway of tumour cells.[272–274] Undoubtedly, all cancer cells demonstrate a high uptake of glycolytic flux; however, ATP generation by mitochondrial flux is also

their important proliferation fuel source (Figure 2.10). To illustrate, data from some experiments have shown that the energy to proliferate MCF-7 breast cancer cells was driven 80% by ATP from oxidative phosphorylation.[275] Some researchers have proven that depending on tumour types, there is a reliance on this mitochondrial function for both survival as well as proliferation.[276,277]

In addition, enzyme inhibitors such as pyruvate dehydrogenase kinases (PDKs) are produced in the matrix metabolism. In the TCA cycle, as previously mentioned, acetyl-CoA and NADH are formed. These compounds inhibit the pyruvate dehydrogenase complex (PDC). Furthermore, the immediate products acetyl-CoA and NADH activate PDKs, which leads to inhibition of PDC activity. However, PDC plays a vital role in connecting glycolysis to the tricarboxylic acid cycle by irreversibly decarboxylating pyruvate to acetyl-CoA. There are also feedback inhibitions of some enzymes such as isocitrate dehydrogenase and α-ketoglutarate dehydrogenase that use ATP and metabolic intermediates of the TCA cycle.[278,279] These inhibitions impair the citric acid cycle processes. Thus, tumour tissues might be able to satisfy their biosynthetic and bioenergetic demands by consuming more glucose. Other studies have experimentally proven that by knocking out specific serine and tyrosine residues, the Warburg effect is promoted via phosphorylating PDH, which, in turn, again causes inactivation of PDC via direct phosphorylation of tyrosine residues (Figure 2.10).[280,281]

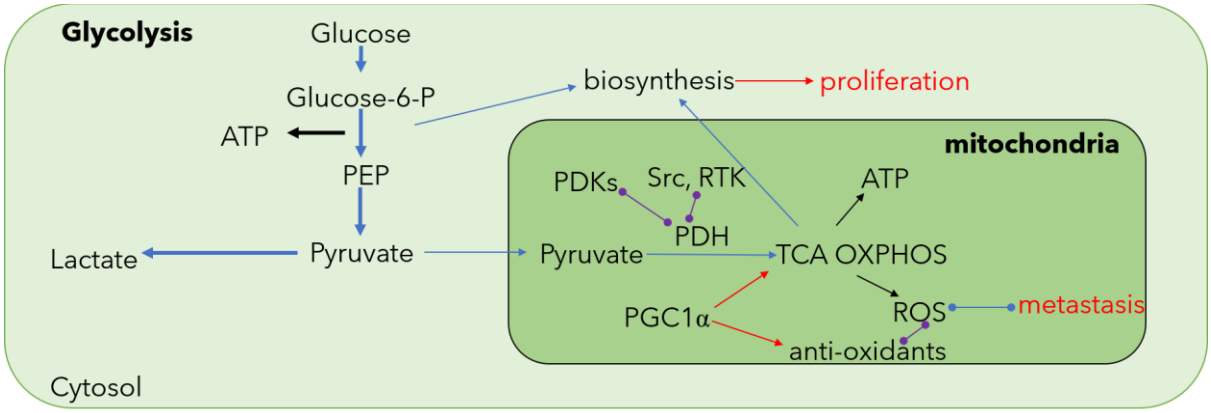

Figure 3.3. The diagram of glucose metabolism in cancer cells.

Schematic illustration of glucose metabolism in cancer cells. A portion of glycolytic intermediates is diverted to biosynthetic pathways for cell proliferation, resulting in glucose being converted to pyruvate. Although the oxidative metabolism continues, it is hindered (at least partly because Src, PDKs and receptor tyrosine kinase (RTK) inhibit PDH) and pyruvate is mostly forcibly pushed to lactate production.

Cancer is in fact, a complex disease where multiple structural alterations, contribute to metabolic cellular metabolism heterogeneity. The metabolic switch from oxidative phosphorylation to aerobic glycolysis is governed by intrinsic factors: oncogenes and tumour suppressor genes.[282] Altered cancer metabolism does not need to be cell-autonomous. Indeed, following the heterogeneity of metabolism, cancer effects the cellular surroundings. Extrinsic properties such as the presence of oxygen, nutrient availability and pH also influence cancer metabolism. Although cancer cells cause upregulation of glycolysis known as Warburg effect, changes of other many pathways are also highly heterogeneous.[283]

The majority of cancer cells' metabolism is highly flexible in the adaption to different microenvironments. To illustrate, under long periods of low-glucose conditions these cells generate energy by OXPHOS for maintaining proliferation.[284]

There are substantial energy demands associated with the metastatic cascade, making it highly selective. Some results suggest that owing to oxidative stress during the migratory, only a few malignant cells survive and proliferate.[285]

In order to survive, normal cells must adhere to extracellular matrix. If cells detach from extracellular matrix, it causes an increase in reactive oxygen species (ROS). An excess amount of these species leads to anoikis which is a barrier to tumor metastasis.[286] An interesting finding depicts that the level of ROS is crucial for normal cells as well as cancer cells. The role of ROS in tumorigenesis was discovered,[287] but there are still many arguments. The small amount of ROS levels might prevent tumorigenesis, whereas the balanced level of that species support proliferation. However, due to metabolic and signalling aberrations, cancer cells may cause a rise in ROS amount, which is, in turn, causes a cell death.[288] As a means of maintaining their viability, cancer cells develop an enhanced antioxidant capacity to keep ROS levels below the critical threshold for cytotoxicity.

The peroxisome proliferator-activated receptor coactivator 1 (PGC1α) proteins family is strong regulator of mitochondrial processes and oxidative metabolism.[289] The generated signals from the PGC1α provide metabolic switch from glycolysis to OXPHOS in glioma cells, thus, inhibiting tumour growth. PGC1α might supress prostate cancer[290] and melanoma model metastasis,[291] whereas it can activate breast cancer metastasis.[292] It is also noteworthy that PGC1α stimulates a broad anti-ROS program which include enzymes such as MnSOD and glutathione peroxidase 1 (GPX1).[293] By protecting from ROS accumulation, excessive PGC1α leads to cell survival during oxidative stress.[294]

Overall, in addition to providing abundant metabolites for proliferating cancer cells, the Warburg effect can reduce oxidative stress, allowing cells to survive the strenuous metastatic pathways. Despite the prevalence of Warburg metabolism in cancer cells, most of them maintain functional mitochondria and can switch between aerobic glycolysis and oxidative metabolism depending on the metabolic treatment. As a result, for Warburg cancer cells to be effectively targeted, combination therapies are needed.

3.2.4 Cancer diagnosing HP techniques

Pyruvate is a substance that has been used very widely for the research of cellular metabolism and its abnormalities connected with diseases such as cancer, heart failure and stroke.[295] Since its increase conversion into lactate offers a route to diagnose cellular abnormalities.

Clinical trials testing this approach for the diagnosis of cancer by magnetic resonance imaging (MRI) have been developing for decades. For example, the hyperpolarization technique dynamic nuclear polarisation (DNP), has allowed the hyperpolarisation and subsequent in *vivo* detection of pyruvate, or other metabolites by MRI (as reviewed by P. Dutta).[124]

Unfortunately, owing to the high cost of this machine the application of this powerful diagnostic tool is limited to few laboratories around the world. The second issue of using DNP technique is the relatively low speed of the hyperpolarization process, it might vary from 0.5 to 3 hours relying on the choice of substrate.

Hyperpolarisation can also be provided by parahydrogen induced polarization (PHIP). Molecules hyperpolarised using PHIP have been widely used in NMR spectroscopy, and there are examples that feature in vivo imaging.[296] Using the spin order of hydrogen enriched in the para isomer, PHIP obtains an unbalanced population of spin states for the hyperpolarization products, based on thermal equilibrium. It is necessary to pairwise transfer both protons from a hydrogen molecule to an unsaturated substrate in hydrogenative PHIP. Rhodium(I) complexes are commonly used as catalysts for this process, as they allow pairwise addition of two hydrogen protons to the substrate molecule through very short-lived intermediates.[146,297] Since the beginnings of hyperpolarization techniques, high nuclear spin polarization of 13C in organic molecules through PHIP have been applied in vivo[298,299] and there have been recent advancements both in hydrogenative[300,301] and non-hydrogenative[183] approaches. The most studied hyperpolarized metabolite is pyruvate, which has been used to study the metabolism of various diseases.[302–305] A number of cancer trials are currently taking place (prostate cancer and breast cancer).[306]

One of the most efficient method to hyperpolarise metabolites such as pyruvate is ParaHydrogen Induced Polarisation Side Arm Hydrogenation (PHIP-SAH). It is an easy-to-operate and lower-cost approach than d-DNP, and PHIP creates highly visible biological products in a few seconds. The method can be described by the following steps (Figure 1): [1-^{13}C]pyruvate (a) is bonded to a side-arm with a triple bond, esterification reaction (I); then the parahydrogenation of this intermediate product occur in an organic solvent (II); in the result the nuclear spin order is shifted from *p*-H_2 to the carboxylate (III); this process finishes by hydrolysis of ester providing the target metabolite in an aqueous solution (IV).[307,308]

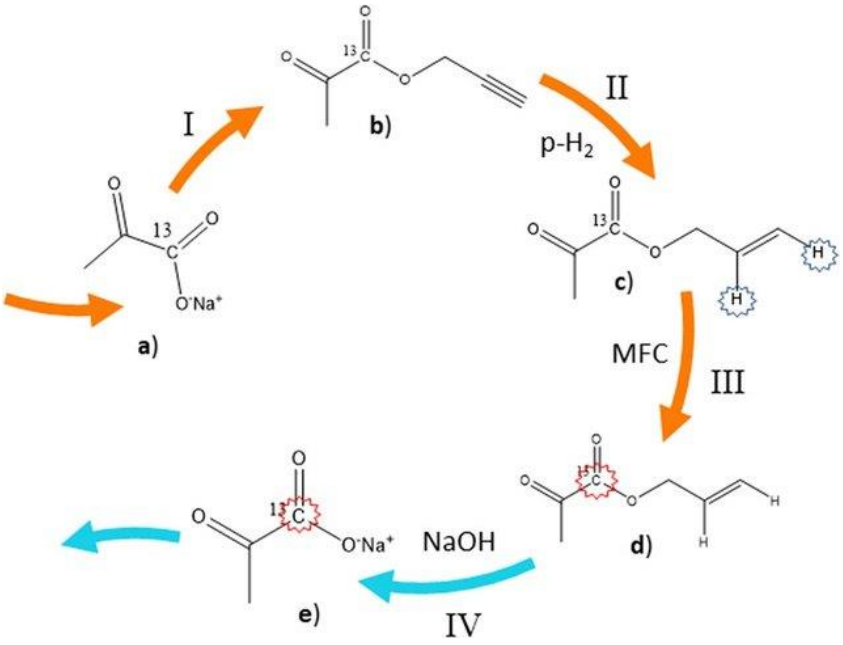

Figure 3.4. Diagram of ParaHydrogen Induced Polarisation Side Arm Hydrogenation process. Image taken from [296]

Many methods have been proposed for the PHIP hyperpolarization of heteronuclei and the polarization transfer step has been studied in detail. [309,310] There have been presented methods such as optimised pulse sequence which maximizes the efficiency of transfer between a nuclear pair and heteronuclei,[311–313] or the ambient magnetic field by using several concentric mu-metal cylinders.[314] Polarisation transfer efficiency is directly related with the scalar coupling asymmetry between 13C and the parahydrogen protons.[315] In RF pulse sequence polarization transfer methods, there are small, long-range J couplings are often involved;[316,317] that is why it has been reported that these methods are less efficient on esters derived from side arm hydrogenation and that MFC is more suitable for the hyperpolarization of the 13C carboxylate signals of an ester. [318] Optimizing the parahydrogenation reaction, polarization transfer, and ester hydrolysis can result in an increased polarization level of the end product. It has

been demonstrated that that 13C hyperpolarization on the allyl ester of [1-13C]pyruvate, following to parahydrogenation and MFC, was increased from about 2% to 5%.[308]

By using a pulsed NMR method, a side-arm hydrogenation scheme has been developed that uses a relaying proton to hyperpolarize metabolites. Using this method, spin-order from the side-arm was transferred to 1-13C pyruvate with 46% efficiency, resulting in 7.6% of 13C polarization.[307]

These PHIP-SAH hyperpolarisation substrates have limitations in biological studies due to their metal complexes, so catalyst removal is necessary. By separating the HP product from its hydrophobic phase, in which hydrogenation takes place, and putting it in the water phase, a considerable amount of metal complex may be removed from the product's aqueous solution.[319] After the parahydrogenation and the polarization transfer, the hydrolysis step in the PHIP-SAH procedure allows to remove the hydrogenated side arm, enabling the separation of the active catalyst that is retained in the organic phase. As a result of Eleonora Cavallari and their team's work,[320] [1-13C]pyruvate hyperpolarized by PHIP-SAH was proven to be a suitable method for evaluating the kinetics of pyruvate metabolism in cell suspensions. In their work, two murine breast cancer cell lines (168FARN and 4T1) were analysed for metabolic 13C label exchange between pyruvate and lactate, catalysed by the LDH enzyme. In addition to its versatility, the PHIP-SAH approach may contribute to a large expansion of metabolic studies in cellular systems due to its accessibility to any NMR lab. PHIP-SAH provides access to HP substrates, allowing researchers to design suitable precursors for key metabolic transformations in a simple and easy manner.[320] This method of hyperpolarising pyruvate results in a one-step, irreversible batch process.

An alternative PHIP-based method that does not require hydrogenation is signal amplification by reversible exchange (SABRE), which involves transferring spin polarisation from *p*-H_2 to the substrate in conjunction with an iridium catalyst, as depicted in the Figure 2.6 and 2.7.[159] In recent years, SABRE has been reported to be capable of hyperpolarizing pyruvate in a cost-effective, fast, and reversible manner without the technological challenges of DNP or the multiple steps of PHIP-SAH.[182]

Chapter 4. Methods

4.1 Methods

NMR and SABRE measurements were performed using a 400 MHz (9.4T) NMR spectrometer (Avance III, Bruker), the temperature was 298 K. The obtained data were analysed using the *TopSpin* program, Versions 3.5 pl 1 and 3.6.1 (Bruker), *Microsoft Excel* 2021, version 16.50 as well as MATLAB_R2020b.

p-H_2 was obtained by cooling gaseous H_2 using a helium refrigeration system over an interconversion catalyst (activated charcoal).

2 mg of iridium catalyst, pyruvate (various amount, usually 2 mg) and 1.5 µL co-ligand DMSO were dissolved in 600 µL of methanol-d_4. Samples then were placed into a 5 mm Wilmad Precision NMR tube with J. Young Valve(S-527-PP-JY-7). Before measurement, the samples were degassed using on a high vacuum Schlenk line techniques (about 3 bar) to remove dissolved oxygen and other gases. The tube was subsequently filled with *p*-H_2 (3 bar) and shaken for 10-20 s in order ensure the *p*-H_2 is able to freely exchange into solution. This manual shaking occurred in the fringe field of the NMR magnet.

Mostly the concentrations have been 0.02 mmol for DMSO, 0.0032 mmol for catalysts and 0.0179 mmol for [1,2-^{13}C]pyruvate, the co-ligand was added by volume (mostly portions of 1.5 µL).

There were also done experiments by altering the concentrations of [1,2-^{13}C]pyruvate and DMSO. Relevant amounts are listed in the appendix.

In this work, T_1 relaxation time was measured using the variable flip angle (Figure 4.1 (a)) and constant flip angle methods (Figure 4.1 (b)).

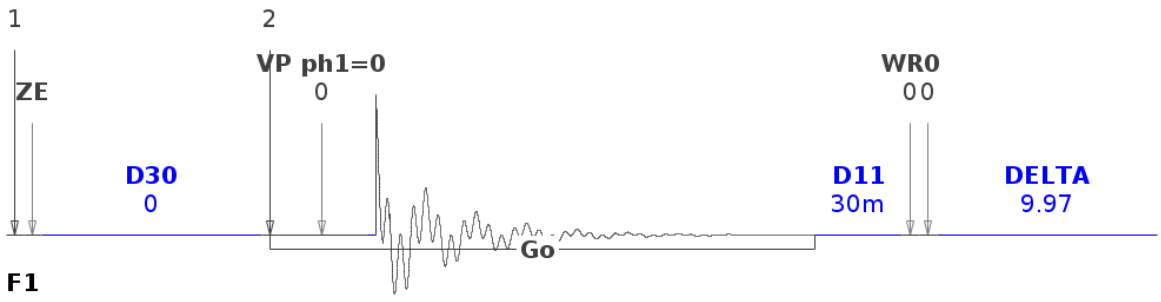

Figure 4.1 (a). The diagram of variable flip angle pulse program, where delay time is 10 s.

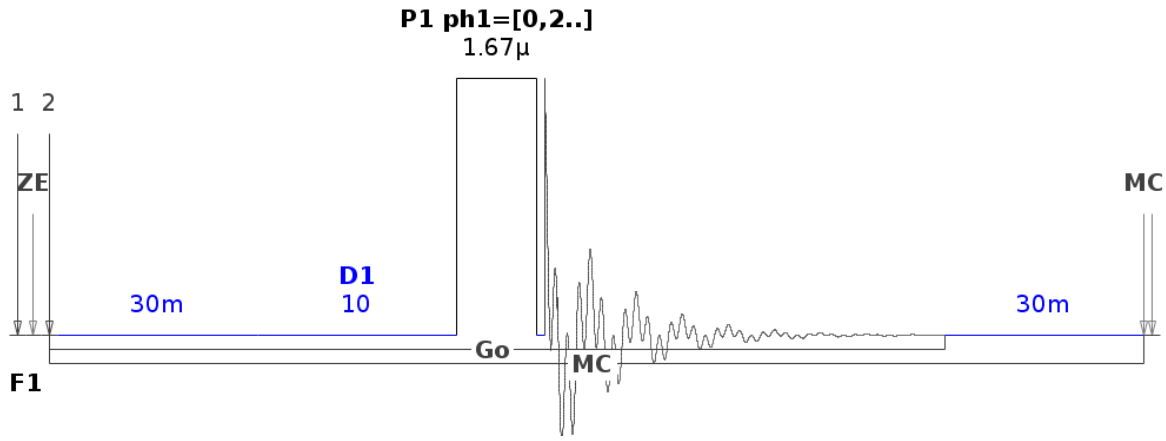

Figure 4.1 (b). The diagram of constant flip angle pulse program, where delay time is 10 s and the pulse angle is 10-degree.

The experiments involved samples of the precatalysts [IrCl(COD)(SIPr)] (2 mg), [IrCl(COD)(IMes)] (2 mg), [IrCl(COD)(SIMes)] (2 mg), [IrCl(COD)(IPr)] (2 mg), DMSO-d_6 (1.5 uL), 13-C_2 pyruvate (2 mg) in 0.6 mL of MeOD.

Variable flip angle experiments were repeated several times with D_{20} set to: 10 sec and 5 sec. Constant flip angle methods were run with the different excitation angles of 5 and 10 degrees and separations times of 5 and 10 seconds.

The two peaks were integrated via *TopSpin* Integrals, Peak A at 203.0 ppm and Peak B at 169.9 ppm. These correspond to the ^{13}C signals for free pyruvate. Their absolute integral numbers were taken into *Excel* and calculations using the solver routine actioned to determine the T_1 value. The error in T_1 was estimated according to the Jack Knife method.

4.2 Signal Enhancement Calculations and Errors

Calculations of the signal enhancements were obtained using equation 4.1.

$$\varepsilon = \frac{SI\ (hyperpolarised)}{SI\ (thermal)} \qquad (4.1)$$

ε – Signal Enhancement, *SI* (thermal) – Integral of the signal from the sample at thermal conditions, *SI* (hyperpolarised) – Integral of the signal from hyperpolarised sample. These integrals of pyruvate's peaks in the thermal and hyperpolarised spectra were consequently used to calculate the signal enhancement levels.

The analytical solution for T_1 precision was derived by standard error propagation methods based on Jack-knife, the Student's distribution and the standard

deviation methods. The jack-knife approach involves leaving out one data point and recalculating the predicted T_1. If there are n observations, then there are *n* jack-knife samples, each of data point size *n*-1. If the original data are $\{x_1, x_2,..., x_n\}$, then the *i* th jack-knife sample is $\{x_1,..., x_{i-1},x_{i+1},..., x_n\}$. Then *n* jack-knife replicates have been computed. An estimate of the standard error from the variance of the jack-knife replicates has been obtained. The jack-knife method can be displayed by the following:

- Compute a statistic, T, on the original sample of size *n*.
- For i = 1 to *n*, repeat the following:
  - Leave out the *i*_th observation to form the *i*_the Jack-knife sample.
  - Compute the i_th jack-knife replicate statistic, T_i, by computing the statistic on the *i*_th jack-knife sample.
- Compute the average (mean) of the jack-knife replicates: $T_{avg} = \Sigma_i T_i/n$.
- Estimate the standard error as SE_{jack} = sqrt((n-1)/n $\Sigma_i(T_i - T_{avg})$**2)

Then, the standard deviation was used which is shown in equation 4.2 to calculate standard errors, where n is the number of experiments (typically between 3 and 6):

$$\sigma = \frac{SD}{\sqrt{n}} \quad (4.2)$$

To obtain precise error, the numbers which were calculated above multiplied to values for Student's t-distributions with v degrees of freedom and for a range of two-sided critical regions. The percentage of confidence level which was used is 95%.

For any nuclei, the polarisation can be calculated by using equation 4.3.

$$P = \frac{\gamma B_0 \hbar}{2k_B T} \quad (4.3)$$

Where γ – gyromagnetic ratio, B_0 – the main magnetic field, $\hbar$ - reduced Planck constant, k_B – Boltzmann constant, T is temperature.

Afterwards, the percentage of polarisation was obtained via the following equation 4.4, where ε is the signal enhancement factor.

$$P(\text{in } \%) = P \cdot \varepsilon \cdot 100 \quad (4.4)$$

Chapter 5. Results and Discussion

5.1 Results and Discussion

One of the main goals of this project is to detect hyperpolarised pyruvate-$^{13}C_2$ using SABRE NMR as well as MRI. Moreover, extending the T_1 is also one of the main aims of this project. A major part of the research is to work out what is the best way to measure the T_1, as each of the methods that have been used have errors associated with them. It is therefore important to collect data for polarisation and T_1 on a variety of samples. Herein, a study of the effects of varying NHCs and the sulfoxide ligands on the SABRE complex [Ir(H)$_2$(η^2-pyruvate)(sulfoxide)(NHC)] and varying their concentrations to generate optimum conditions for achieving high signal gains in an inexpensive and reversible way is described.

When pyruvate-1,2-[$^{13}C_2$] is added to a precatalyst (for example, [IrCl(COD)(IMes)]) in the presence of a co-ligand (typically, DMSO) and 3 bar of hydrogen in MeOH added, an equilibrium mixture of [IrCl(H)$_2$(DMSO)$_2$(NHC)] and [Ir(H)$_2$(η^2-pyruvate)(DMSO)(NHC)] is produced (Figure 5.1). The latter product occurs in two forms that are distinguished by their ligand arrangements: in one isomer the ligated pyruvate is *trans* to both hydride and the NHC, as illustrated in **iii**, while in the other isomer the target substrate lies *trans* to the two hydride ligands is shown in **iv**.[230]

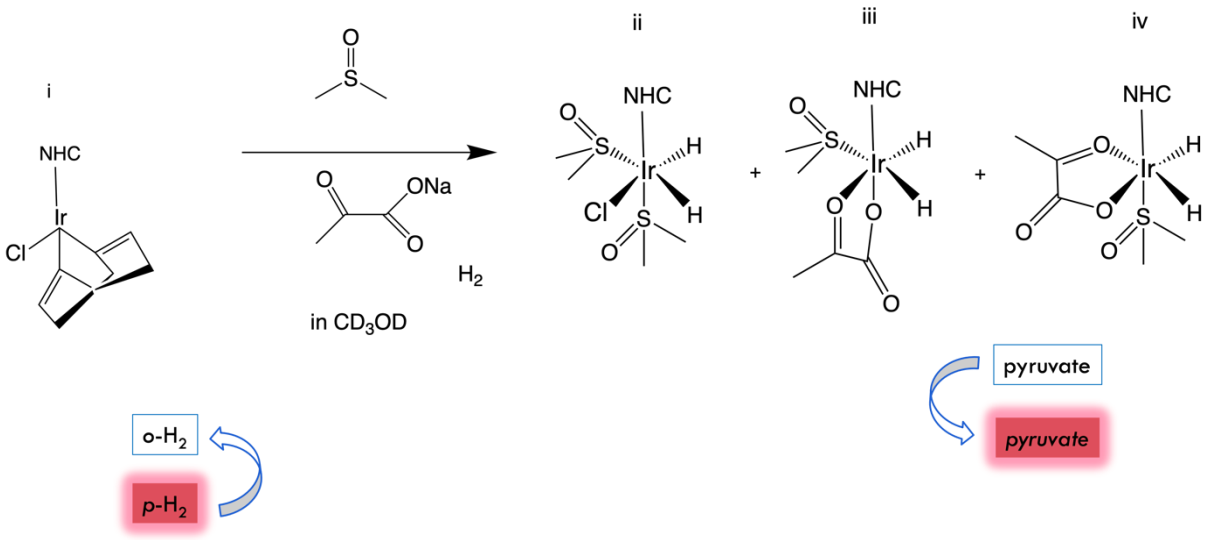

Figure 5.1. The possible SABRE pyruvate hyperpolarisation reaction that is achieved by [Ir(H)$_2$(η^2-pyruvate)(DMSO)(NHC)] where *para*-hydrogen exchange is highly mediated via [IrCl(H)$_2$(DMSO)$_2$(NHC)].[230]

The result of SABRE on a typical sample is shown in Figure 5.2. Clearly the NMR signal strengths for the carbonyl peaks of pyruvate are substantially larger

than those in the upper spectrum which reflects the corresponding acquisition with thermally polarise magnetisation. The following NMR spectra were obtained for the reaction of [Ir(Cl)(COD)(IMes)], the common SABRE catalyst precursor,[164] with DMSO, hydrogen and $^{13}C_2$ enriched sample of sodium pyruvate to produce [Ir(H)$_2$(η^2-pyruvate)(DMSO)(IMes)]. After sample transfer into a 9.4 T magnet under *para*-hydrogen, strongly hyperpolarised ^{13}C resonances corresponding to free pyruvate were observed.

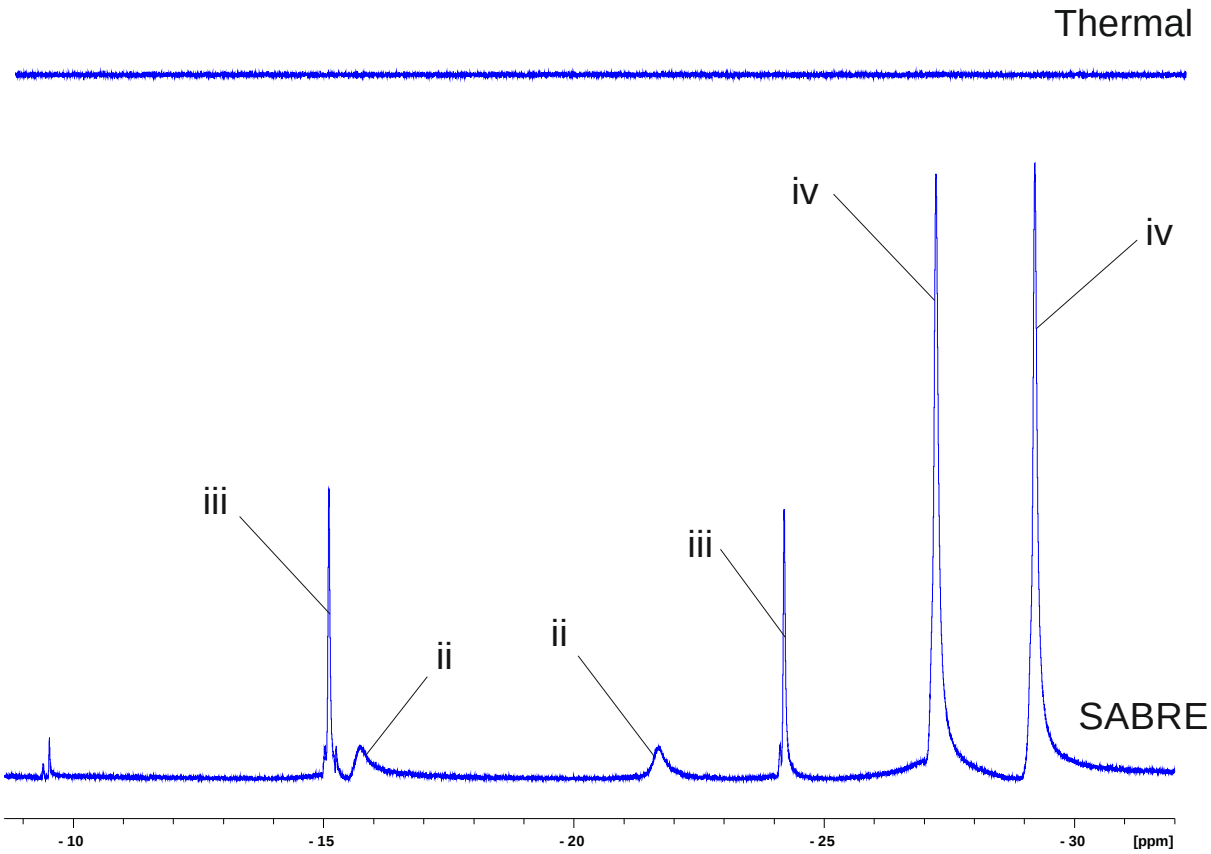

(a)

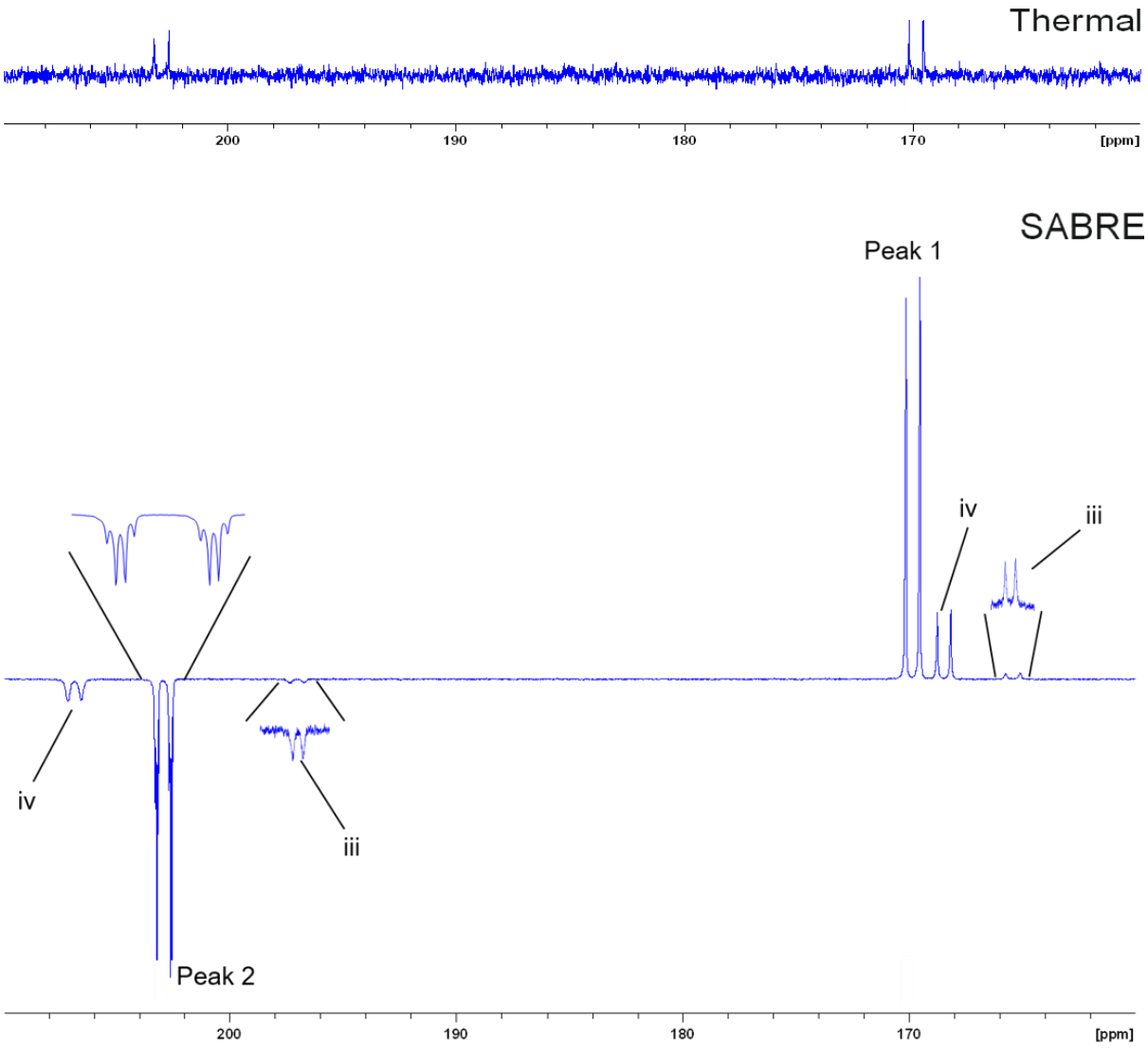

(b)

Figure 5.2. (a) Thermal and SABRE hyperpolarised NMR spectra of ^{1}H hydride region; (b) Thermal and SABRE hyperpolarised NMR spectra of ^{13}C region after shaking a sample of **i**, sodium pyruvate-1,2-[$^{13}C_2$] and DMSO with *p*-H_2. The sample was shaken manually for around 10 seconds before measurement in a 400 MHz spectrometer at 9.4 T.

I first obtained high-field proton NMR spectra at 298 K to confirm that the main hydride containing complex in the solutions was **iv**. Peaks for **ii** and **iii** were not spotted under thermal conditions. However, after filling the tube with 3 bar of para-hydrogen and shaking it for about 10 seconds, hyperpolarised peaks for the hydride responses of **ii**, **iii** and **iv** were observed (Figure 5.2(a)).[231] The corresponding hyperpolarised ^{13}C NMR spectra showed strong signals corresponding to free pyruvate at δ 169 and δ 203 (J_{CC} = 62 Hz). The catalyst-bound pyruvate responses for **iv** are also detected in these NMR spectra as hyperpolarised signals, at 168 ppm and 207 ppm (J_{CC} = 60 Hz). There are also tiny signals for the catalyst-bound pyruvate ligand at 161 ppm and 198 ppm (J_{CC} = 63 Hz) (Figure 5.2 (c)) in **iii**.

Figure 5.3., shows the results of a catalyst variation study, and it can be seen that when IMes is the NHC ligand the highest polarisation levels are observed for both of the peaks of [1,2-^{13}C]Pyruvate, 341-fold for [1-^{13}C] and 301-fold for [2-^{13}C]. SIMes enhances the signal a factor of 2.5 times, and 1.2 times, less respectively than IMes. The IPr catalyst hyperpolarised these peaks to 186 and 173 fold signal gains relative to the thermal peak, and SiPr creates the lowest enhancement level at just above 50-fold for [1,2-^{13}C]Pyruvate at 9.4 T.

Consequently, the highest polarisation level is achieved by the sample containing [Ir(Cl)(COD)(IMes)] (0.0032 mM), DMSO and pyruvate and this results in about 0.3% for [1-^{13}C] when these reagents are present in a 1:6:6 ratio after ~10 s shaking with 3 bar of *para*-hydrogen. This complex was chosen by Ducket *et al.* and Feiters *et al.*, in a previous study and they obtained enhancement values of 1.16%[164] and 1.11%[175] respectively. The difference in these values is likely to reflect the different concentrations used, and variation in prepolarisation field strength. Nevertheless, the demonstrated highest enhancement among other NHC ligands is in reasonable accordance with this MSc Research.

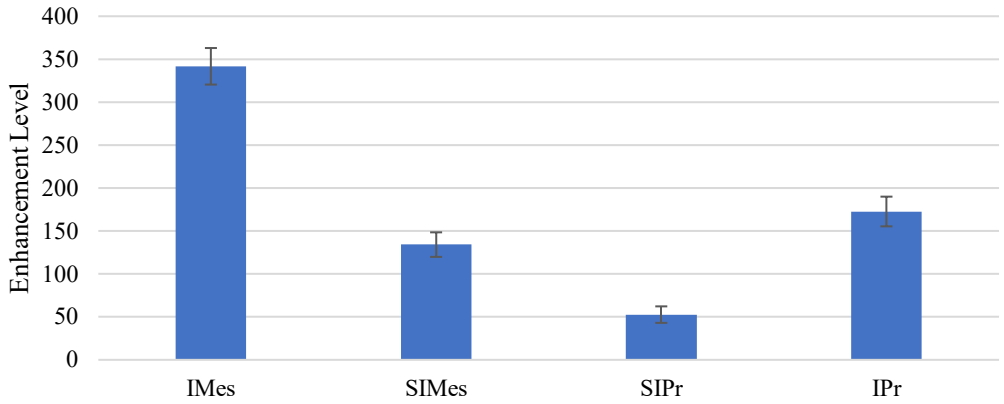

(a)

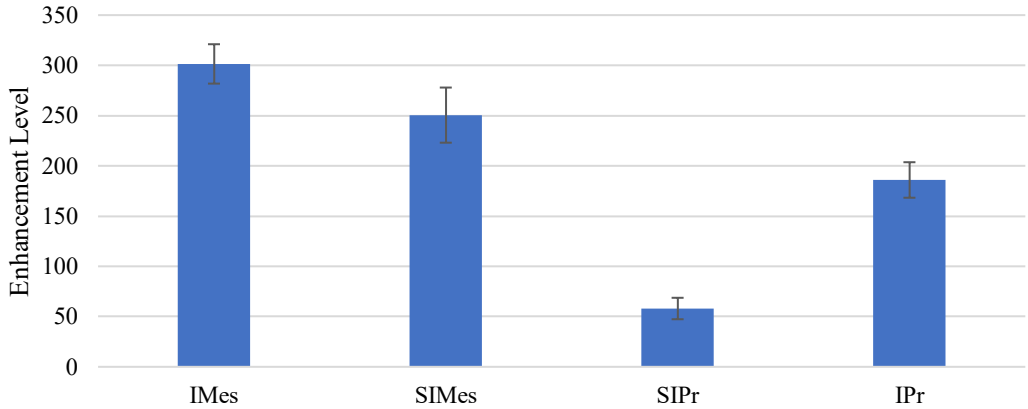

(b)

Figure 5.3. Signal Enhancement values measured for [1-^{13}C]Pyruvate (a) and [2-^{13}C]Pyruvate (b) sites with various NHC ligands. The standard deviation was used which is shown in equation 4.2 to calculate standard errors, where n is the number of experiments (for these graphs they are from 2 to 5).

Design of the catalyst was previously discussed in **Section 2.1.4.3.1**; the signal enhancement is affected by electron donating characteristics, steric bulkiness and exchange rates for the substrate and H_2 (Table 2.1 and 2.2). The four ligands used in this research can be compared according to their Tolman Electronic Parameters by the following order IMes > IPr > SIMes > SIPr and they can be ordered by their steric bulkiness properties IMes < SIMes < IPr < SIPr.[178–180] These properties of the carbene ligand will influence the exchange rate between pyruvate and hydrogen or DMSO and so the polarisation build up in solution. It is seen that the saturated ligands have larger steric parameters than their unsaturated analogues. Reported experiments have revealed that the exchange rate of pyridine grows with the ligands' steric bulkiness.[175] This was also proven with IMes that the exchange undergoes by a dissociative pathway in accordance with thermodynamic and density functional theory (DFT).[164] The level of signal enhancement in the free material directly relies to the ligand exchange rate but the polarisation transfer occurs through the scalar coupling system within the hydride ligand and substrate in the bound SABRE complex.[167]

In this research project, the exchange rate has not been measured. Nevertheless, an indirect measure of their relative rates should be illustrated by the ratio of signal integrals for the bound and free pyruvate peaks. The higher the ratio, the faster the exchange rate (Figure 5.4). These comparisons might be expected to support the previous results on NHC ligands that steric bulkiness and the exchange rate are related.[175] Although steric bulky molecules can be speed up the exchange rate, if this process is too fast, they depict lower signal enhancements. This means that there is a sweet spot where the exchange rate will lead to high signal enhancement.[175] IMes, giving the highest signal enhancement is therefore supplying the optimal exchange rate for these four systems.

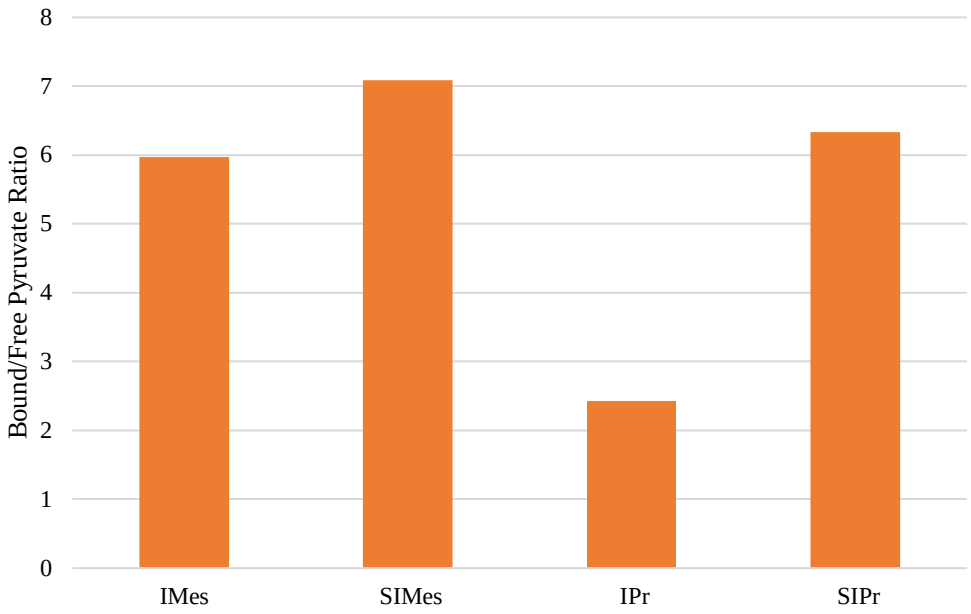

Figure 5.4 The ratio between bound and free [1-^{13}C] site of hyperpolarised [1,2-^{13}C]pyruvate at various temperature, with IMes NHC ligand, DMSO in methanol-d_4 at 9.4T.

As the n = 1, more repeats are required in the future to make these results statistically significant.

One of the main benefits of hyperpolarised pyruvate measurement is the ability to monitor processes related to a variety of inflammatory, ischemic and metabolic diseases. The most important properties in choosing the optimal ^{13}C enrichment site must be: i) chemical shift difference between the sample and respective metabolites; ii) appropriate longitudinal relaxation time, since it indicates how long the magnetisation takes to decay back to the equilibrium state and visibility stops.[321] And it consequently determines whether it is possible to precisely and accurately interrogate biochemical processes in *vivo*. Carbon atoms on carbonyl groups such as in pyruvate have high relaxation times, that is why ^{13}C enriched analytes have been targeted as biological substrate in the HP techniques and T_1 is important.

In this MSc by Research work, the longitudinal relaxation time of two sites of [1,2-$^{13}C_2$]pyruvate has been measured and analysed. The intensity of the two pyruvate peaks were monitored under the variable and constant flip angle protocols to determine T_1. A typical decay curve for hyperpolarised [1,2-^{13}C]pyruvate is represented in Figure 5.5. The peak integrals were fitted by an exponential decay (equation 3.5), thereby providing access to a decay constant. The constant flip angle experiments resulted in finding that the longest longitudinal relaxation time for the [1-^{13}C]pyruvate site with the SIMes containing catalyst using a 10-degree pulse with 5 seconds delay (Figure 5.6) was 54.8 ±1.0 s. These parameters for constant flip angle pulse were chosen for the

data recording, and subsequent analysis, since they have provided the best determined and longest spin-lattice relaxation times; other P1 and D1 values (Figure 5.8) were tested. According to the variable flip angle pulse sequence results, for [1-^{13}C], a 5 second delay time (D20) and for [2-^{13}C] a 10 second delay time were selected. Again these parameters yielded the longest T_1 time for the respective peaks (Figure 5.9). The [2-^{13}C]pyruvate site, with the IPr containing catalyst led to the longest relaxation time of 44.7 ± 1.7 s, via variable flip angle data and a 10 second delay (Figure 5.7).

These results are challenging to interpret. It is important that we encode signal for as long as possible to accurately determine these T_1 values. However, the signal is destroyed by the measurement so only so many sampling points can be used. Furthermore, the T_1 times for the two carbon centres are different. The result of this complex interplay of effects means that getting the correct delay and readout sequence is vital if accurate data is to result.

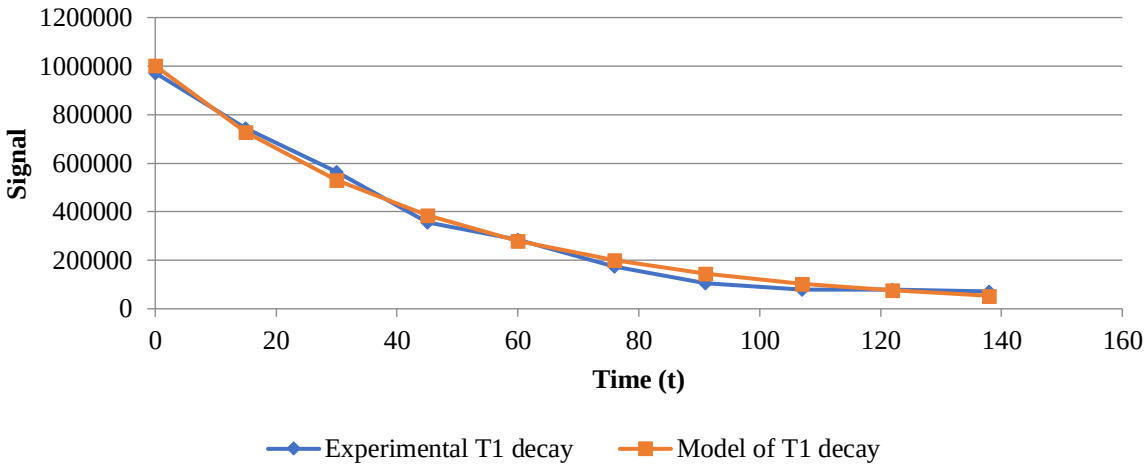

Figure 5.5 A typical T_1 decay curve, and fit to a suitable mathematical model, for the [1-^{13}C] site data obtained with hyperpolarised [1,2-^{13}C]pyruvate using IMes as the NHC ligand and DMSO as the co-ligand in methanol-d_4 at 9.4T. The extracted T_1 value for these data was 46.0 ± 2.3 s.

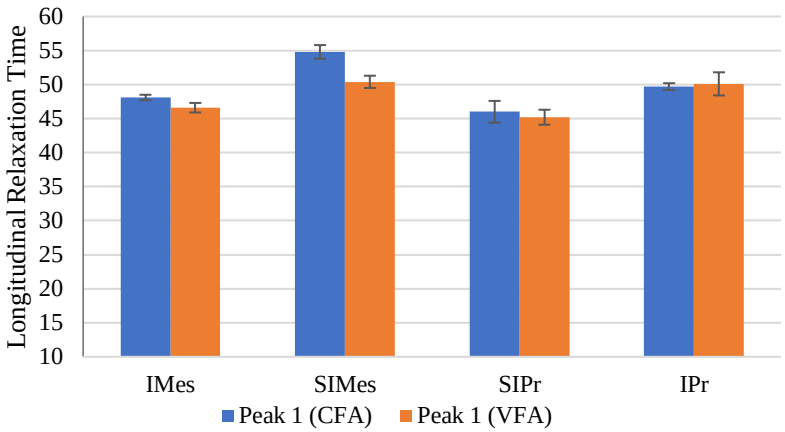

Figure 5.6 T_1 values of the [1-^{13}C]Pyruvate site as a function of NHC determined using the Constant Flip Angle approach (P1 is 10 degree and D1 is 5 seconds) and Variable Flip Angle (D20 is 5 seconds) approach. The standard deviation was used which is shown in equation 4.2 to calculate standard errors, where n is the number of experiments (typically between 3 to 6).

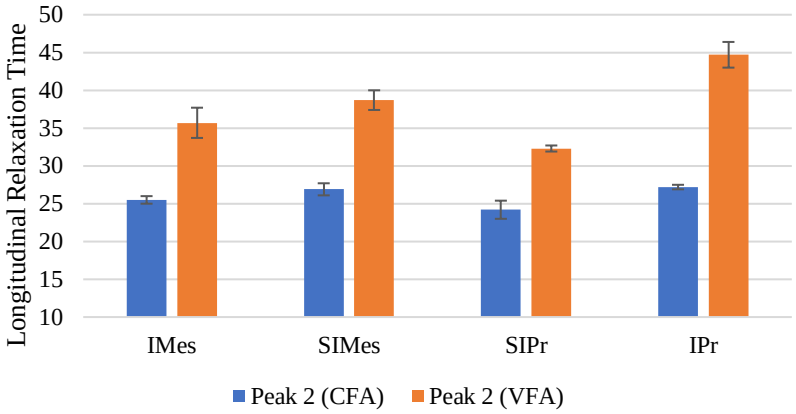

Figure 5.7 T_1 values of [2-^{13}C]Pyruvate site using Constant Flip Angle (P1 is 10 degree and D1 is 5 seconds) and Variable Flip Angle (D20 is 10 seconds) pulse sequences. The standard deviation was used which is shown in equation 4.2 to calculate standard errors, where n is the number of experiments (typically between 3 to 6).

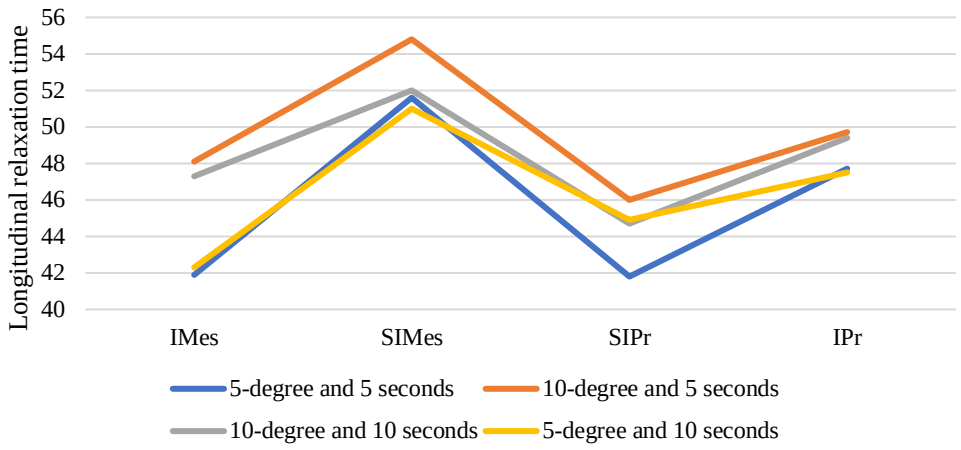

Figure 5.8 Comparison of T_1 values for [1-^{13}C] site using various Constant Flip Angle pulse sequences. Setting a 10-degree pulse and 5 seconds delay time has provided the longest relaxation time

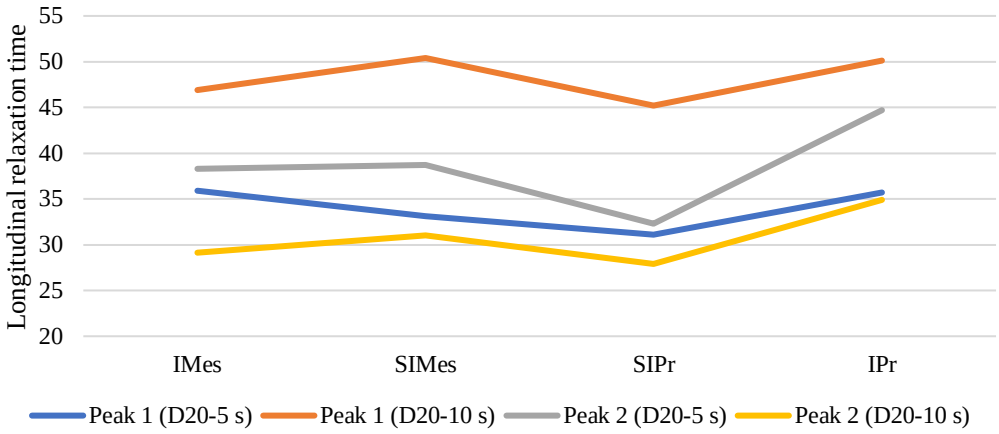

Figure 5.9 Comparison of T_1 values for both [1-^{13}C] and [2-^{13}C] sites using two Variable Flip Angle pulse sequences. Setting a 5 seconds delay time has provided the longest relaxation time for [2-^{13}C] and 10 seconds delaying has been the favourable option for the first site of pyruvate.

It is clearly observed that the [1-^{13}C]pyruvate site shows the highest enhancement factor (342-fold) and possesses the longest relaxation time (approximately 55 seconds at 9.4 T). This site of pyruvate therefore offers the highest signal-to-noise ratio for real time studies. However, there are many factors that might affect T_1-relaxation as discussed in **Section 3.1.3**. The relaxation times which were measured earlier for [1-^{13}C] and [2-^{13}C]pyruvate probes are approximately 67 sec and 39 sec at 3.0 T respectively.[302] As previously mentioned, T_1 depends on the magnetic field strength. That is why the literature T_1 values are different from this thesis's results.

The ancillary ligands act to control the exchange rate of pyruvate when bound to the catalyst. Furthermore, it is normal for the bound pyruvate to have a shorter

T_1 than the free material, as effective size increases and more dipole-dipole interactions are present to drive relaxation. Hence under exchange, the T_1 of the free material is influenced by the time it spends on the catalyst and hence its ligands.

Pyruvate has low symmetry, that is why $[Ir(H)_2(\eta^2\text{-pyruvate})(DMSO)(IMes)]$ forms 2 non-equivalent hydride ligands even at relatively low magnetic field reflective of a [AA'XX'] spin system. A, theoretical model for the effective polarisation transfer between these spins under SABRE-SHEATH has been described.[322] This theory used to predict optimum magnetic field strength needed polarisation transfer.[182] Moreover, it has been shown that a long-lived singlet states population in ^{13}C can extend the lifetime of hyperpolarised [1,2-^{13}C]pyruvate to 85 s at a low field and 44 s at high field (Table 5.1). T_{LLS} is used to refer to the decay time of a long-lived singlet state, which is usually longer than T_1.

Table 5.1 Hyperpolarisation levels and relaxation times for [1,2-^{13}C]pyruvate populated by a long-lived single state and for [1-^{13}C], [2-^{13}C]-pyruvate isotopologues.[182]

Substrate	^{13}C polarisation (%)	Thermally polarised longitudinal relaxation times, T_1 (s)	Hyperpolarised longitudinal relaxation times, T_1 (s)
[1-^{13}C]pyruvate	C_1: 0.96	C_1: 35.4 ± 0.5	C_1: 32.5 ± 4.7
[2-^{13}C]pyruvate	C_2: 0.60	C_2: 20.1 ± 0.5	C_2: 18.2 ± 3.0
[1,2-^{13}C]pyruvate	C_1: 1.85	C_1: 33.6 ± 0.5	T_{LLS} (HF): 43.5 ± 0.8
	C_2: 1.65	C_2: 21.2 ± 0.4	T_{LLS} (LF): 85.4 ± 8.5

Moreover, managing the polarisation transfer process requires careful consideration of the relaxation caused by the presence of the catalyst as well as the exchange rate which allows build-up of polarisation within pyruvate. Consequently, the apparent (measured) relaxation time is highly dependent on the exchange rates of both para-hydrogen and the analyte.[175] It has been already mentioned that there is a high possibility that SABRE reactions with SIMes have the fastest exchange rate among the NHC ligands studied here. This property would cause the shortest apparent spin-lattice relaxation time which is directly opposite to that predicted based on the bound:free signal ratio.

However, when we consider the [2-^{13}C] Pyruvate resonance, we see that the longest longitudinal relaxation time of 44.7 ± 1.7 s is seen for IPr, even though IPr has the lowest bound/free pyruvate ratio and hence what we think of as the slowest pyruvate exchange rate. Clearly another effect is occurring.

Even though IMes provides the highest polarisation level, the relaxation time with SIMes is longest. Regardless of these numbers and the deductions we might make, practicality must also be remembered. There is going to be some time delay between preparation of the sample and its detection in *situ* as well as in *vivo*. If a long time is required, SIMes could be the better catalyst, if, for example, 60 s is enough to prepare the sample, IMes might be beneficial as it provided better in signal availability. Which one would be better might depend on how long we have before the detection. In the experiments, the total time after shaking the NMR tube with *p*-H_2 through the solution and before SABRE NMR measurement is started was approximately 5 s. That is to say, this time also might be reduced in the future, using automatic way of this procedure.

The next experiments were done by altering concentration of [1,2-$^{13}C_2$]pyruvate and DMSO. Figures 5.11 and 5.12 show the influence of Pyruvate concentrations on the observed longitudinal relaxation time which is somehow exchange weighted. It can clearly be seen that using 4 mg of 13-carbon enriched pyruvate (concentration ratio of catalyst to pyruvate is 1:11) increases the apparent T_1 value. This supports the idea that the ligand exchange involves a bimolecular process, involving the interception of an intermediate by pyruvate. This will speed up with increase in pyruvate concertation. If the catalyst has a quicker relaxation time than the free material, we will therefore see a drop off in T_1. The trends in Figure 5.10 are consistent with this view.

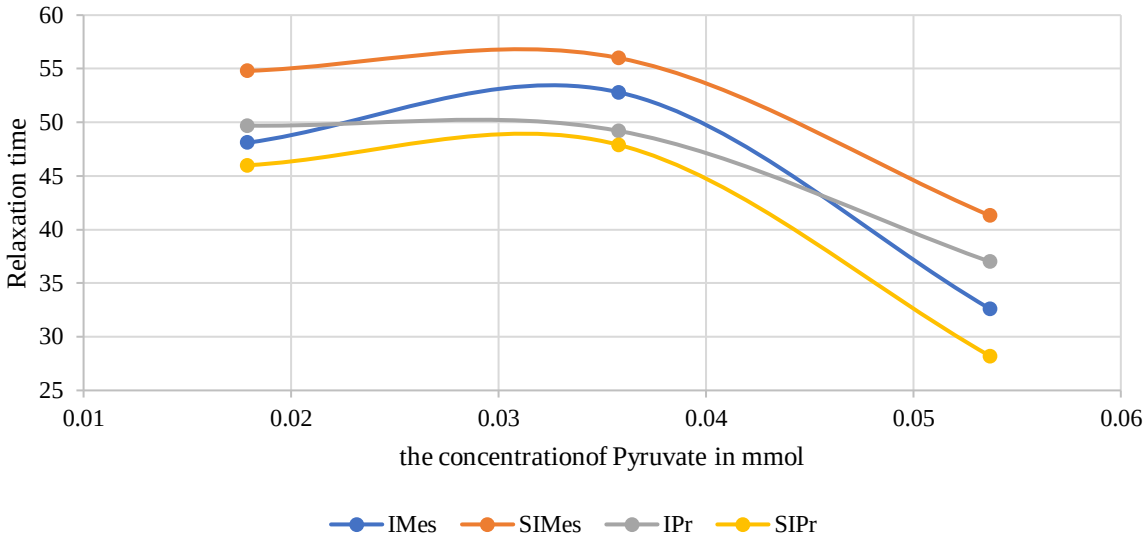

Figure 5.10. Comparison of T_1 values for both [2-^{13}C] site by varying Pyruvate's concentrations (0.0179 mmol, 0.0358 mmol and 0.0537 mmol). The longest T1 time is shown with 0.0358 mmol conc. $^{13}C_2$-Pyruvate with SIMes pre-catalyst. The overall trend is demonstrating that the increasing substrate concentration extend the relaxation time, however, it goes down after

0.0358 mmol concentration of the substrate. The parameters for measuring T_1 for this graph is Constant Flip Angle pulse sequence, P1 is 10-degree and D1 is 5 seconds.

In order to obtain a more accurate perspective on the effect of analyte concentration on T_1, these experiments were repeated with seven distinct pyruvate concentrations. The IMes NHC ligand systems was chosen for these SABRE measurements, since it depicts the highest polarisation level amongst the pre-catalysts and should lead to the highest accuracy in T_1.

The results now clarify behaviour. The T_1 relaxation time values have been plotted as detailed in Figure 5.11 (a). An apparent T_1 maximum is seen at ~ 4mg loading, as there is a shallow gradient leading to an increase in apparent T_1 of pyruvate prior to a dramatic fall. The experiments involve an 0.0032 mM catalyst concentration and 0.0090 mM pyruvate concentration (1: 3 ratio), increasing by a factor of ~3 per mg meaning the optimum ratio is 1:11 to maximise the T_1. According to the mechanism, pyruvate ligand exchange proceeds via the opening of the chelate to form an η^1-bound intermediate which can be intercepted by H_2 or pyruvate (Figure 5.11(b)). Increasing the concentration of pyruvate therefore promotes ligand exchange and therefore the equilibration of T_1 values between the free and bound forms. If the bound form has a shorted T_1 than the free form, the T_1 will compress. This is what is observed beyond 4 mg. The small but consistent increase from 1-4 seconds is interesting and suggests that we now change the rate limiting step for ligand exchange that leads to a T_1 reduction in some way.

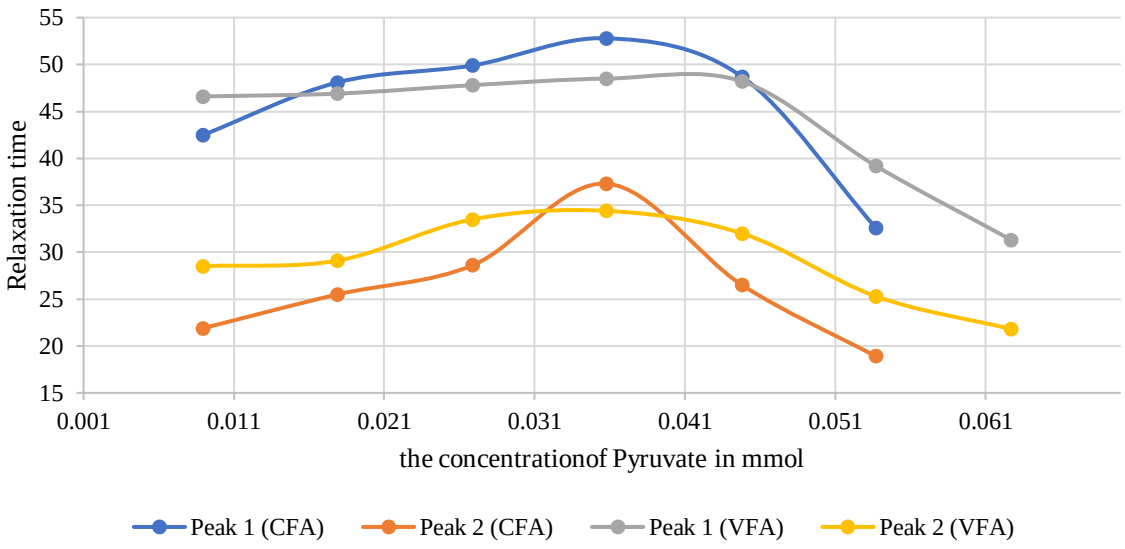

(a)

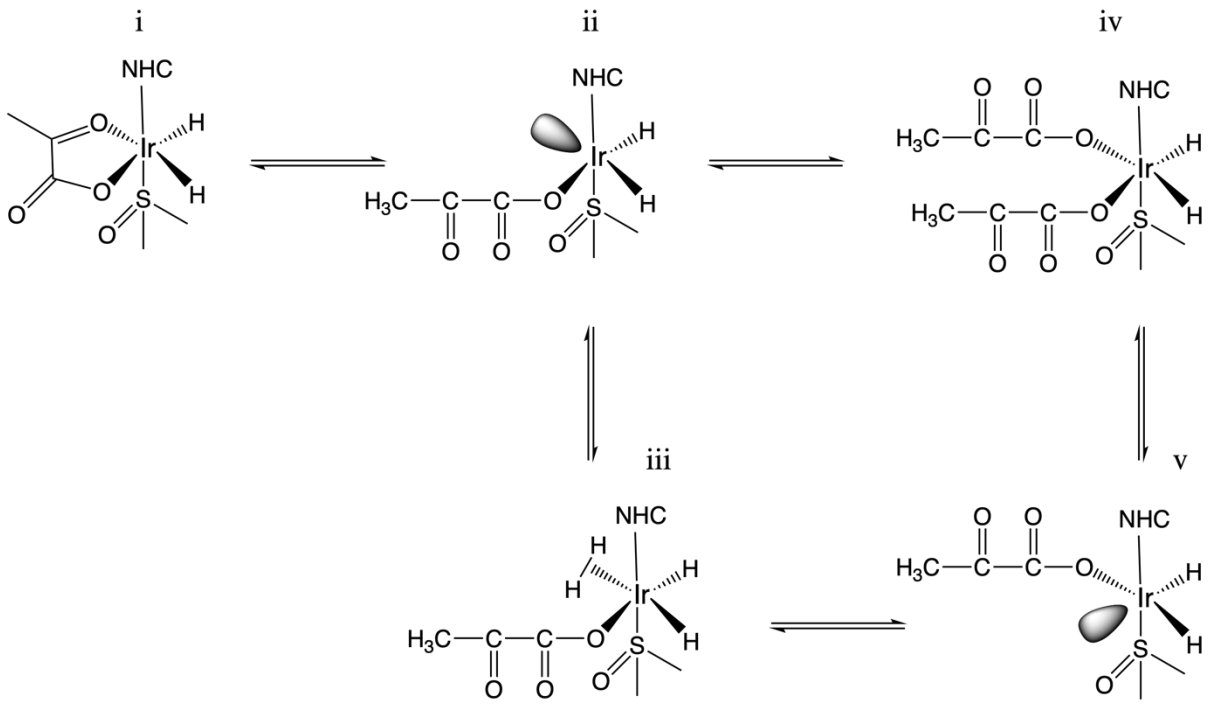

(b)

Figure 5.11 (a) Comparison of T_1 values for both [1-^{13}C] and [2-^{13}C] sites by varying Pyruvate's concentrations. The longest T_1 time is shown with 0.0358 mmol $^{13}C_2$-Pyruvate the overall trend is demonstrating that the increasing substrate concentration extend the relaxation time, however, it goes down after certain amount of the substrate. The NHC ligand that was in this SABRE complex is [IrCl(COD)(IMes)]; (b) The possible mechanisms when concentration of the pyruvate is varied. According to the mechanism, pyruvate ligand exchange proceeds via the opening of the chelate to form an η^1-bound intermediate (ii) which can be intercepted by H_2 (iii) or pyruvate (iv). The reversible formation of a 16-electron intermediate with an η^1-bound pyruvate ligand can be occur afterwards (v). It can return to the starting complex by rechelation (i), or react with H_2 (iii).

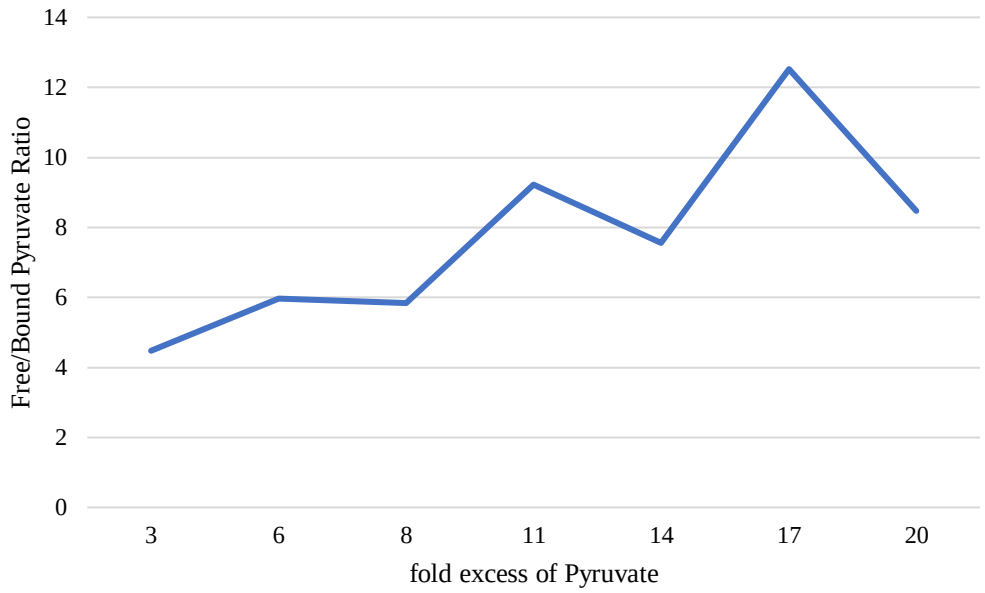

Figure 5.12 The ratio between bound and free [1-^{13}C] site of hyperpolarised [1,2-^{13}C]pyruvate at various amounts of the substrate, with IMes as a NHC ligand, DMSO in methanol-d_4 at 9.4 T.

When we plot the ratio of the free the bound signals, it remains somewhat constant until 4 mg is reached. This is consistent with the reversible formation of a 16-electron intermediate with an η^1-bound pyruvate ligand. It can return to the starting complex by rechelation, or react with H_2, necessary for SABRE. Competitive reaction with pyruvate is needed for exchange. This process begins to compete effectively at the 4 mg load as the free to bound ratio now takes off and begins to approach that expected for an averaged process.

Despite the fact that DMSO is the main co-ligand in this research, diphenyl sulfoxide (DPSO) was examined as well. In this case, only SIPr was used as the NHC ligand for the catalyst. Although the enhancement factor of pyruvate with DPSO as the co-ligand proved higher than for DMSO (136-fold vs 57-fold respectively) it shortened the relaxation time of [1-^{13}C]Pyruvate by ~1.5 times (Figure 5.13) thereby implying a faster ligand exchange rate.

SABRE derived hyperpolarisation experiments have also shown that pyridine leads to improved signal gains when DPSO is utilised.[229] This article suggested that using a more sterically bulky sulfoxide, with larger effective cone angle, led to bigger signal enhancements. DMSO has the effective circular cone angle of 111.6° whereas for DPSO's it is 124.4°. This causes an improved binding affinity for Ir. The consequence of changing the co-ligand from DMSO-d_6 to DPSO might therefore be expected to increase the targeted pyruvate polarisation level if the exchange rate is too slow. This is however, not supported by the data which shows

that fact the free to bound pyruvate ratio with DMSO-d_6 is greater relative to DPSO (Figure 5.13 (d)).

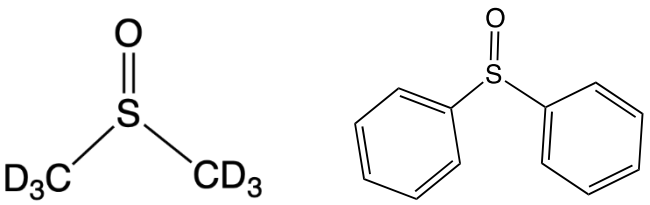

(a)

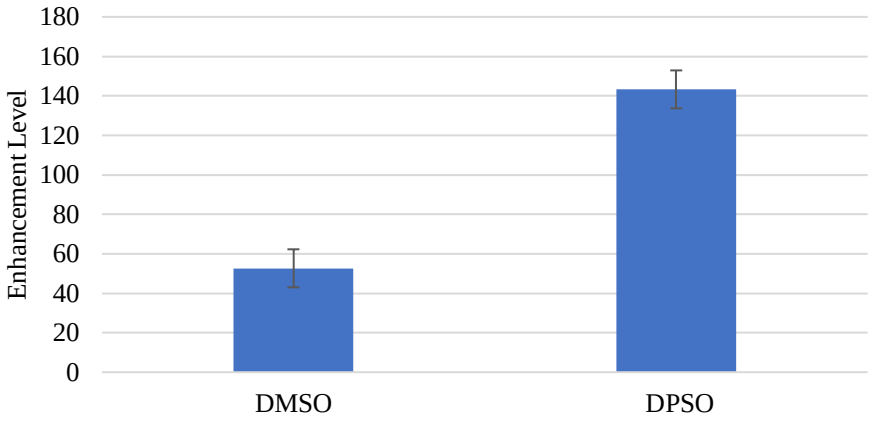

(b)

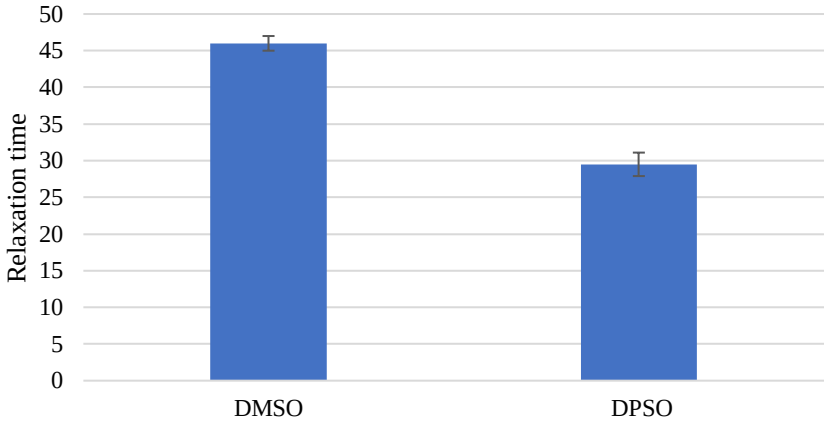

(c)

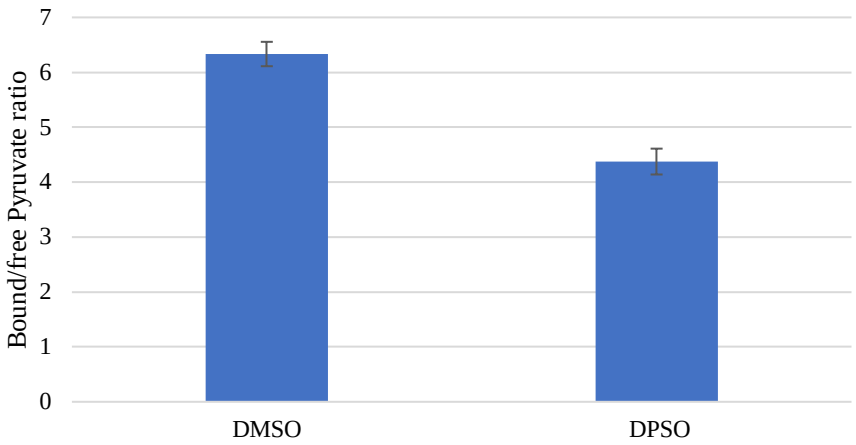

(d)

Figure 5.13 (a) dimethyl sulfoxide (DMSO) (left) and diphenyl sulfoxide (DPSO) (right) structure; (b) Signal Enhancement values measured for [1-^{13}C]Pyruvate with SIPr as NHC ligand, DMSO-d_6 or DPSO in methanol-d_4 at 9.4 T; (c) T_1 values of [1-^{13}C]Pyruvate site after interrogation with a constant 10° pulse and 5 seconds delay time with two different co-ligands; (d) The ratio between bound and free [1-^{13}C] site of hyperpolarised [1,2-^{13}C]pyruvate with two different co-ligands. The standard deviation was used which is shown in equation 4.2 to calculate standard errors, where n is the number of experiments (typically between 4 to 12).

Temperature is also a factor affecting to the hyperpolarisation level and lifetime of pyruvate bound to the metal centre. Many researchers have examined this factor by varying the temperature of the SABRE system in order to achieve an optimum exchange rate.[226,233] One study showed that for DMSO as a co-ligand and IMes or SIMes as precatalysts, the maximum enhancement of free pyruvate ^{13}C was achieved at 293 K.[230]

To this end, solutions of IMes, 11.2 equivalents of sodium pyruvate-1,2-[$^{13}C_2$], and 6.25 equivalents of the DMSO-d_6, were shaken with 3 bar *p*-H_2 in methanol-d_4 at five different temperatures (263 K, 273 K, 283 K, 298 K and 303 K). These were achieved by placing the NMR tube in a thermostatically controlled water bath for a period of one minute, then immediately afterwards the tube was shaken for about 10 seconds under *para*-hydrogen at room temperature. The observed [1,2-^{13}C]pyruvate signal enhancement is illustrated in Figure 5.14 (a). For IMes as the precatalyst, the resulting substrate signal enhancement is maximised at 303 K. The proportion of free substrate magnetisation relative to the bound substrate signal is also growing while the temperature is elevated, which confirms faster exchange (Figure 5.14 (b)).

The effect of temperature on T_1 was also explored. As the data in Figure 5.14 (c) shows, T_1 seems to increase with temperature. It is impossible to draw firm conclusions from this T1 data as the sample was shaken at 298 K and dropped into the probe whose temperature was set. Consequently, the samples are not at a

precise temperature when the data is recorded. Nonetheless, we can see that there is a general trend which is consistent with that expected.

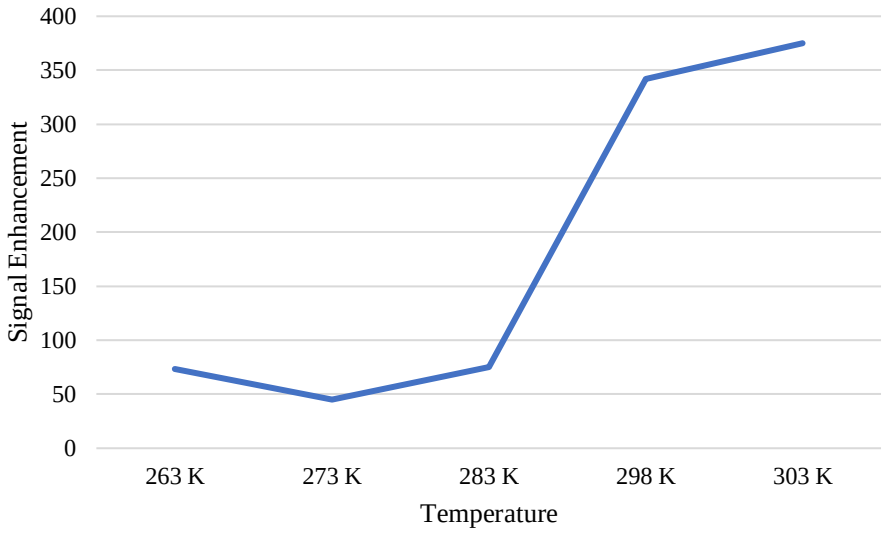

(a)

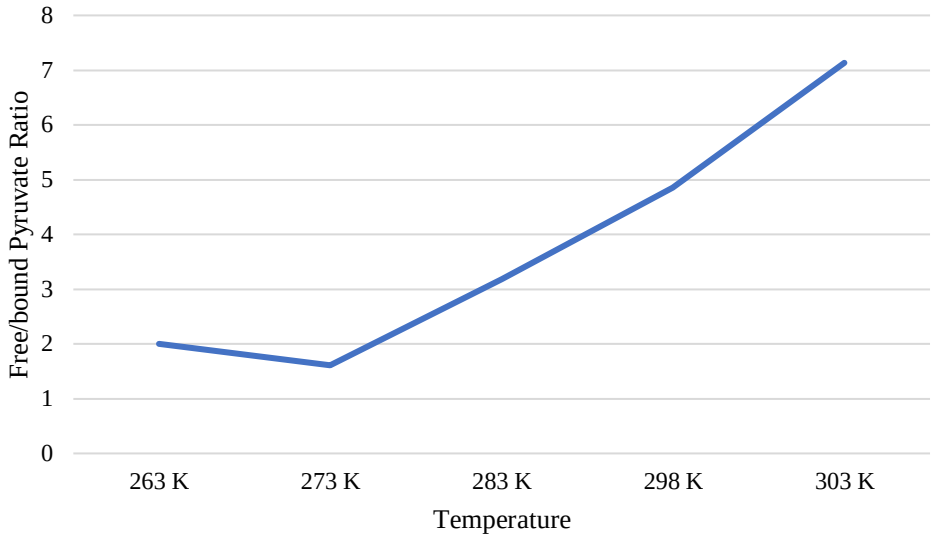

(b)

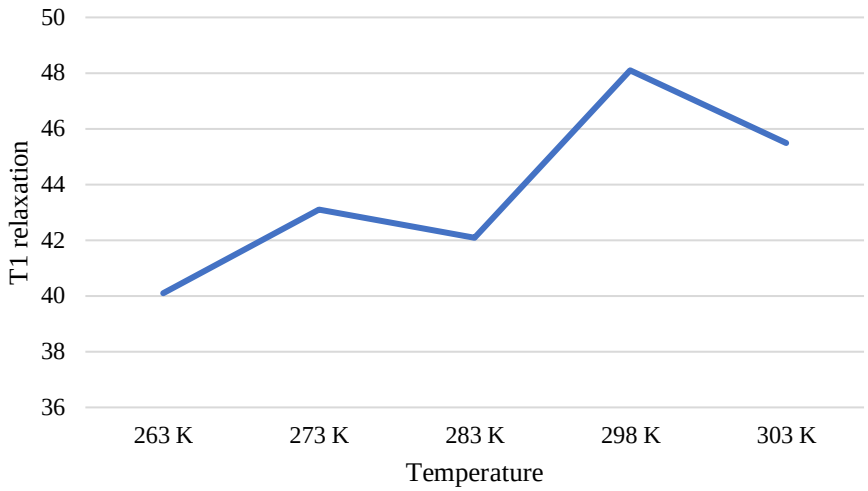

(c)

Figure 5.14 (a) Signal Enhancement values measured for [1-^{13}C]Pyruvate with IMes as NHC ligand, DMSO-d_6 in methanol-d_4 at various temperatures; (b) T_1 values of [1-^{13}C]Pyruvate site after interrogation with a constant 10° pulse and 5 seconds delay time; (c) The ratio between bound and free [1-^{13}C] site of hyperpolarised [1,2-^{13}C]pyruvate.

The effect of the concentration of DMSO-d_6 on both the [1,2-^{13}C]pyruvate polarisation level and its relaxation time was also examined. Table 5.2, demonstrates that the amount of DMSO affects the enhancement level but not the observed T_1 value. It has been proposed that DMSO and hydrogen exchange proceed via formation of the same common 16-electron intermediate [IrCl(H)$_2$(DMSO)(IMes)] through a dissociative first step. H_2 exchange then proceeds via the formation of [IrCl(H)$_2$(H_2)(DMSO)(IMes)]; in another words, indirect H_2 exchange, rather than direct H_2 exchange (loss).[231]

Table 5.2. Signal Enhancement values, bound to free proportions ratio and relaxation times measured for [1-^{13}C]Pyruvate with IPr as an NHC ligand, with various amount of DMSO-d_6 in methanol-d_4 at room temperature. For Signal Enhancement and Free to Bound ratio the standard deviation was used which is shown in equation 4.2 to calculate standard errors, where n is the number of experiments (typically between 4 to 10). Jack Knife method was used to calculate standard errors, where n is the number of experiments (typically between 4 to 10).

DMSO-d_6 amount	Signal Enhancement	Free to bound pyruvate ratio	T_1 relaxation
1.5 µL	172.7 ± 17.7	2.4	49.7 ± 0.5
3.0 µL	184.1 ± 17.1	2.8	51.2 ± 1.3
4.5 µL	128.9 ± 13.8	2.4	50.6 ± 0.5

MRI experiments

MRI SABRE measurements have been performed using a 7T MRI preclinical spectrometer at room temperature. The obtained data were analysed using the *MATLAB* program. *p*-H_2 was obtained by cooling gaseous H_2 using a helium refrigeration system over an interconversion catalyst (activated charcoal). 10 mcg of iridium catalyst, 10 mg pyruvate and 7.5 µL co-ligand DMSO were dissolved in 3 mL of methanol-d_4. Samples then were placed into a 10 mm Wilmad Precision NMR tube with J. Young Valve(S-527-PP-JY-7). Before measurement, the samples were degassed using on a high vacuum Schlenk line techniques (about 3 bar) to remove dissolved oxygen and other gases. The tube was subsequently filled with *p*-H_2 (3 bar) and shaken for 10-20 s in order ensure the *p*-H_2 is able to freely exchange into solution. This manual shaking occurred in the fringe field of the MRI magnet.

Various imaging parameters were used to obtain hyperpolarised pyruvate image. The first was FLASH sequence with low excitation flip angles of 5° to 10°. As first carbon nuclei of the [1,2-^{13}C]pyruvate shows the highest signal, it was chosen for imaging (Figure 5.15(a)). The size of these images were 32 pixel × 32 pixel.

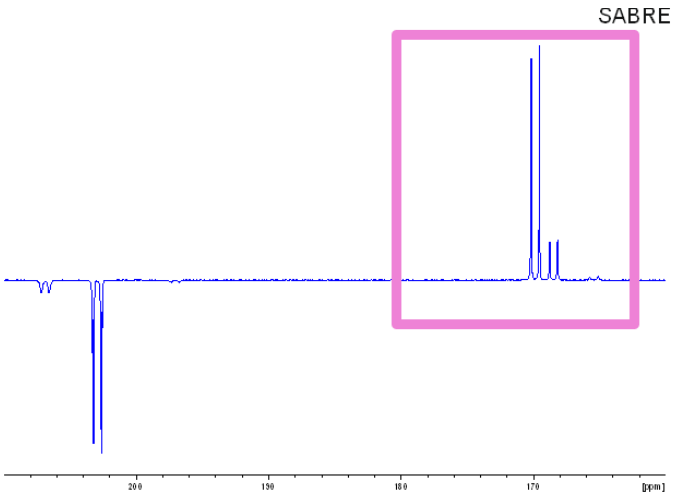

(a)

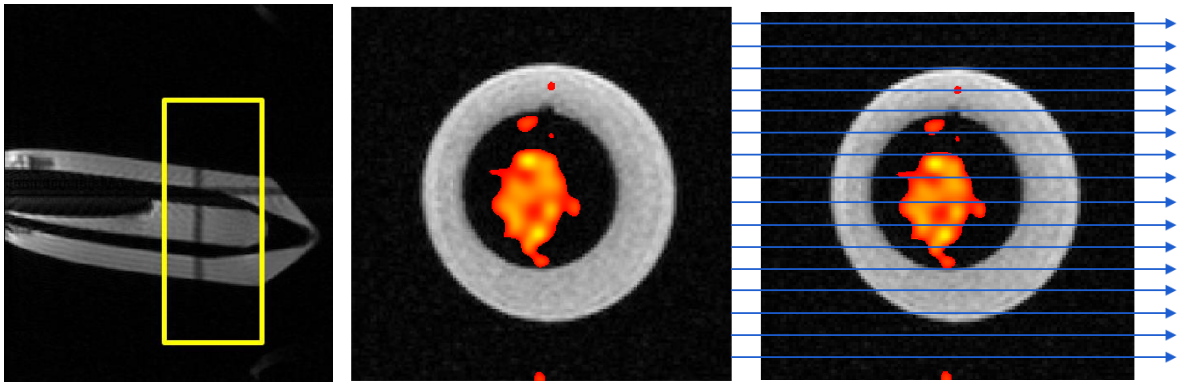

Figure 5.15 (a) Integral analysis across 161 ppm and 171 ppm peaks was selected; (b) the analysed field from the 10 mm Young's tube containing the sample surrounded by a falcon tube containing a water/agar mixture; (c) the image of HP [1,2-^{13}C]pyruvate using Imaging a single nuclear oscillator – FLASH; (d) the illustration of acquired linear and centrically encoded FLASH sequence.

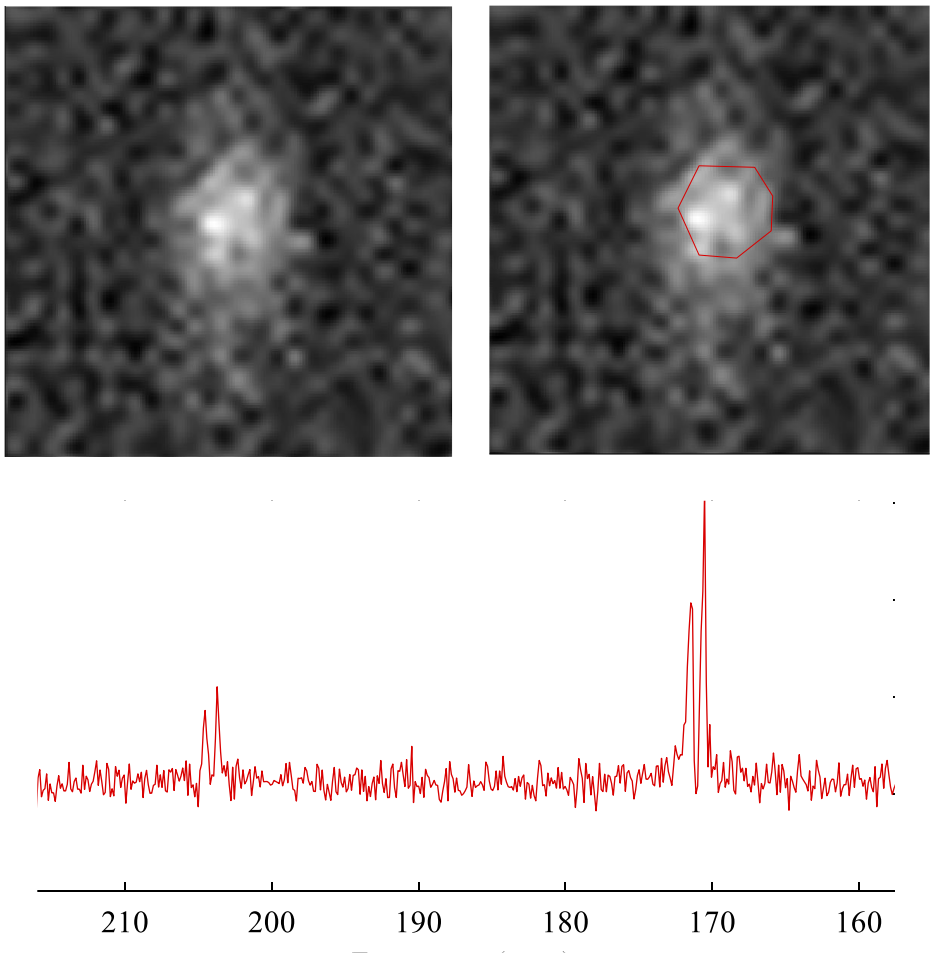

Figure 5.16 (a) Hyperpolarised CSI (Chemical Shift Imaging) signal from of [1,2-^{13}C]pyruvate; (b) selected high intesity signal area of target molecule for the spectra; (c) the NMR spectra of HP [1,2-^{13}C]pyruvate.

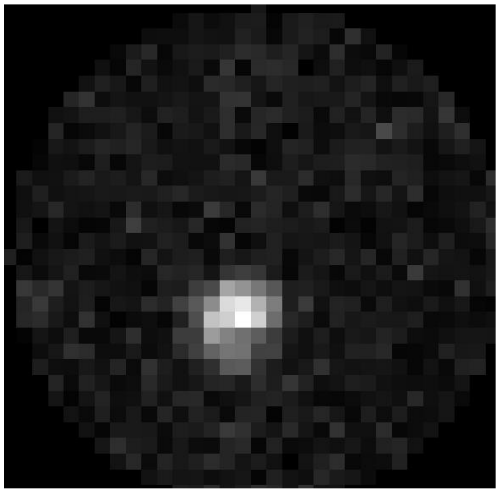

Figure 5.17. The image of [1,2-^{13}C]pyruvate by spiral acquisition

The extracted images by centric encoding, CSI and spiral encoding took 158.6 ms, 1 min 33 s and 23.1 ms respectively. It can be estimated that linear and centrically encoded FLASH sequence might be optimal option to extract the image of hyperpolarised [1,2-^{13}C]pyruvate in terms of time and the accurate measurement.

In conclusion, our aims were extending spin-lattice relaxation time as well as enhancing polarisation level of [1,2-^{13}C]pyruvate utilising SABRE process. There have been four NHC ligands (IMes, SIMes, IPr and SIPr) utilised to achieve these objectives. [IrCl(COD)(IMes)] catalyst generated 341-fold enhancement for [1-^{13}C] site of hyperpolarised [1,2-^{13}C]Pyruvate. This is the largest signal enhancement among other precatalysts. That is to say, IMes is possibly the most effective complex in terms of exchange rate. Its buried volume and electron donating properties lead to create fast enough exchange to produce the highest enhancement for substrate. Although the latter catalyst has shown the high signal, [IrCl(COD)(SIMes)] has provided the longest T1 value, which might be critical for pre-clinical measurements. The one limitation for this catalyst is that it enhances the signal 2.5 times less than IMes.

The effect of concentrations of the analyte and co-ligand have been examined. The highest signal and longest T1 time are obtained with 0.0358 Mmol of $^{13}C_2$-Pyruvate. However, the concentration of DMSO-d_6 might not be a significant factor for either relaxation time or signal enhancement.

The measurements of varying the temperature seem to be less accurate, since, there have been a rapid change of temperature during the experiment's performance. Nonetheless, the overall change in signal size might assume that the polarisation is going up via increasing the temperature and 303 K which the maximum temperature used, may be optimum temperature. Whereas, for relaxation time, the suitable condition can be a room temperature.

Knowing the polarisation level of target analytes is vital as the longer hyperpolarised lifetime provide a quality and accurate monitoring or imaging in metabolism. On the other hand, the practicality is also must be considered, there is going to be a time delay between preparation of the hyperpolarised sample and its detection because it is polarised remotely from the end point of observation. Due to increased magnetic state lifetimes, signal detection is now possible over a longer time frame and can provide significant advantages for tracer analysis.[230]

In this MSc by research project, we have demonstrated the effects of various complexes present in the sample, their concentrations and temperatures at which the measurements might be successfully obtained in terms of delivered hyperpolarisation. Thus, by varying these conditions, we studied characteristics of the SABRE catalyst to generate an optimum rationale for reaching high ^{13}C pyruvate signal enhancements.

5.2 Significance of the results

SABRE hyperpolarisation has the potential to aid clinical diagnosis of cancer by probing pyruvate metabolism and characteristics such as timescale and cost of parahydrogen make this an attractive avenue for study. From the results of a catalyst variation study, and it can be seen that when IMes is the NHC ligand the highest polarisation levels are observed for both of the peaks of [1,2-^{13}C]Pyruvate, 341-fold for [1-^{13}C] and 301-fold for [2-^{13}C]. Moreover, in this MSc by Research work, the longitudinal relaxation time of two sites of [1,2-$^{13}C_2$]pyruvate has been measured and analysed. The experiments resulted in finding that the longest longitudinal relaxation time for the [1-^{13}C]pyruvate and for [2-^{13}C]pyruvate sites with the SIMes and the IPr containing catalysts, showing 54.8 ±1.0 s. and 44.7 ± 1.7 s, accordingly. It is clearly observed that the [1-^{13}C]pyruvate site shows the highest enhancement factor and possesses the longest relaxation time. This site of pyruvate therefore offers the highest signal-to-noise ratio for real time studies.

The next experiments results show that using 4 mg of 13-carbon enriched pyruvate (concentration ratio of catalyst to pyruvate is 1:11) increases the apparent T_1 value.

The temperature effects' results can be also important to consider in the future studies. In this research, it shows that for IMes as the precatalyst, the resulting substrate signal enhancement is maximised at 303 K. Moreover, the effect of temperature on T_1 depicts that T_1 seems to increase with temperature.

The results of this MSc are measurements that provide high levels of hyperpolarisation for $^{13}C_2$-pyruvate using particular catalyst NHC-ligand combinations and specific conditions. These studies provide results that will help with the future use of SABRE hyperpolarised $^{13}C_2$-pyruvate. The importance of relaxation is clearly indicated and this is influenced by the catalyst and temperature. It will be vital to optimise these parameters if the best signal gains are to be achieved.

References

1. Dubois, J. *et al.* MRI of the Neonatal Brain: A Review of Methodological Challenges and Neuroscientific Advances. *Journal of Magnetic Resonance Imaging* vol. 53 1318–1343 Preprint at https://doi.org/10.1002/jmri.27192 (2021).
2. Freeman Ray, 1932-. *Magnetic resonance in chemistry and medicine*. (Oxford University Press, 2003).
3. Hövener, J.-B. *et al.* Parawasserstoff-basierte Hyperpolarisierung für die Biomedizin. *Angewandte Chemie* **130**, 11310–11333 (2018).
4. de Feyter, H. M. *et al. Deuterium metabolic imaging (DMI) for MRI-based 3D mapping of metabolism in vivo*. *Sci. Adv* vol. 4 https://www.science.org (2018).
5. Miloushev, V. Z., Keshari, K. R. & Holodny, A. I. Hyperpolarization MRI preclinical models and potential applications in neuroradiology. *Topics in Magnetic Resonance Imaging* vol. 25 31–37 Preprint at https://doi.org/10.1097/RMR.0000000000000076 (2016).
6. Purcell, E. M., Torrey, H. C. & Pound, R. v. Resonance absorption by nuclear magnetic moments in a solid. *Physical review* **69**, 37 (1946).
7. Borisov, A. S., Hazendonk, P. & Hayes, P. G. Solid-state nuclear magnetic resonance spectroscopy: A review of modern techniques and applications for inorganic polymers. *Journal of Inorganic and Organometallic Polymers and Materials* vol. 20 183–212 Preprint at https://doi.org/10.1007/s10904-010-9358-5 (2010).
8. Slichter C. P.
9. Lasoialfari, A., Filibian, M., Sangregorio, C. & Carretta, P. In vivo biomedical applications of magnetic resonance and magnetic materials. *Rivista del Nuovo Cimento* vol. 36 211–271 Preprint at https://doi.org/10.1393/ncr/i2013-10089-8 (2013).
10. Buxton 1954-, R. B. *Introduction to functional magnetic resonance imaging : principles and techniques*. (Cambridge University Press, 2009).
11. Schwarzschild, B. Lauterbur and Mansfield Awarded Nobel Medicine Prize for Magnetic Resonance Imaging. *Phys Today* **56**, 24–27 (2003).
12. Durston, S. & Casey, B. J. What have we learned about cognitive development from neuroimaging? *Neuropsychologia* **44**, 2149–2157 (2006).
13. Babic, R. R., Babic, G. S., Babic, S. R. & Babic, N. R. 120 Years Since the discovery of X-Rays/120. Godina od otkrica X-Zraka. *Med Pregl* **69**, 323+ (2016).
14. Boivin, G. & Meunier, P. J. The degree of mineralization of bone tissue measured by computerized quantitative contact microradiography. *Calcif Tissue Int* **70**, 503 (2002).
15. Mould, R. F. The early history of X-ray diagnosis with emphasis on the contributions of physics 1895-1915. *Phys Med Biol* **40**, 1741–1787 (1995).
16. Frans, J. T. David E. Kuhl (1929–2017). *Journal of Nuclear Cardiology* **26**, 1062–1063 (2019).
17. Jaszczak, R. J. & Coleman, R. E. Single photon emission computed tomography (SPECT). Principles and instrumentation. *Invest Radiol* **20**, 897–910 (1985).
18. Pablico-Lansigan, M. H., Situ, S. F. & Samia, A. C. S. Magnetic particle imaging: advancements and perspectives for real-time in vivo monitoring and image-guided therapy. *Nanoscale* **5**, 4040–4055 (2013).
19. Hirschmann, M. T., Davda, K., Rasch, H., Arnold, M. P. & Friederich, N. F. Clinical value of combined single photon emission computerized tomography and conventional computer tomography (SPECT/CT) in sports medicine. *Sports Med Arthrosc Rev* **19**, 174–181 (2011).
20. Kuhl, D. E. & Edwards, R. Q. Image separation radioisotope scanning. *Radiology* **80**, 653–662 (1963).

21. Hutton, B. F. The origins of SPECT and SPECT/CT. *Eur J Nucl Med Mol Imaging* **41**, 3–16 (2014).
22. Pichler, B. J., Judenhofer, M. S. & Pfannenberg, C. Multimodal imaging approaches: Pet/ct and pet/mri. *Molecular Imaging I* 109–132 (2008).
23. Buchbender, C., Heusner, T. A., Lauenstein, T. C., Bockisch, A. & Antoch, G. Oncologic PET/MRI, part 2: bone tumors, soft-tissue tumors, melanoma, and lymphoma. *Journal of Nuclear Medicine* **53**, 1244–1252 (2012).
24. Saad, F. F. A., Kqueen, C. Y., Hassan, H., Mustafa, S. & Nordin, A. J. 18F-FDGPET-CT is a Useful Molecular Marker in Cancer Biology.
25. Bockisch, A. *et al.* Principles of PET/CT and clinical application. *Radiologe* **44**, 1045–1054 (2004).
26. Bogowicz, M. *et al.* Comparison of PET and CT radiomics for prediction of local tumor control in head and neck squamous cell carcinoma. *Acta Oncol (Madr)* **56**, 1531–1536 (2017).
27. Bailey, D. L. *et al.* Combined PET/MR: The Real Work Has Just Started. Summary Report of the Third International Workshop on PET/MR Imaging; February 17–21, 2014, Tübingen, Germany. *Mol Imaging Biol* **17**, 297–312 (2015).
28. Phelps, M. E. PET: the merging of biology and imaging into molecular imaging. *Journal of Nuclear Medicine* **41**, 661–681 (2000).
29. Ross, B. & Bluml, S. *Magnetic Resonance Spectroscopy of the Human Brain*. (2001).
30. Gujar, S. K., Maheshwari, S., Björkman-Burtscher, I. & Sundgren, P. C. Magnetic resonance spectroscopy. *Journal of neuro-ophthalmology* **25**, 217–226 (2005).
31. Kwock, L. *et al.* Clinical role of proton magnetic resonance spectroscopy in oncology: brain, breast, and prostate cancer. *Lancet Oncol* **7**, 859–868 (2006).
32. Golder, W. Magnetic resonance spectroscopy in clinical oncology. *Oncol Res Treat* **27**, 304–309 (2004).
33. Menichetti, L. *et al.* Assessment of real-time myocardial uptake and enzymatic conversion of hyperpolarized [1-13C] pyruvate in pigs using slice selective magnetic resonance spectroscopy. *Contrast Media Mol Imaging* **7**, 85–94 (2012).
34. Najac, C. & Ronen, S. M. MR Molecular Imaging of Brain Cancer Metabolism Using Hyperpolarized 13C Magnetic Resonance Spectroscopy. *Top Magn Reson Imaging* **25**, 187–196 (2016).
35. Woitek, R. & Gallagher, F. A. The use of hyperpolarised 13C-MRI in clinical body imaging to probe cancer metabolism. *Br J Cancer* **124**, 1187–1198 (2021).
36. Mishkovsky, M. & Comment, A. Hyperpolarized MRS: New tool to study real-time brain function and metabolism. *Anal Biochem* **529**, 270–277 (2017).
37. Meyer, D. & Larsen, M. Nuclear magnetic resonance gyro for inertial navigation. *Gyroscopy and Navigation* **5**, 75–82 (2014).
38. Lee, J. H., Okuno, Y. & Cavagnero, S. Sensitivity enhancement in solution NMR: emerging ideas and new frontiers. *J Magn Reson* **241**, 18–31 (2014).
39. Brown, M. A. & Semelka, R. C. *MRI: Basic Principles and Applications*. (Wiley, 2011).
40. Pons, D. J., Pons, A. D. & Pons, A. J. A Physical Explanation for Particle Spin. *Journal of Modern Physics* **10**, 835–860 (2019).
41. GEROTHANASSIS, I. P., TROGANIS, A., EXARCHOU, V. & BARBAROSSOU, K. NUCLEAR MAGNETIC RESONANCE (NMR) SPECTROSCOPY: BASIC PRINCIPLES AND PHENOMENA, AND THEIR APPLICATIONS TO CHEMISTRY, BIOLOGY AND MEDICINE. *Chem. Educ. Res. Pract.* **3**, 229–252 (2002).

42. Lombardi, M. *et al. The EACVI Textbook of Cardiovascular Magnetic Resonance*. (OUP Oxford, 2018).
43. Gossuin, Y., Hocq, A., Gillis, P. & Quoc Lam, V. Physics of magnetic resonance imaging: From spin to pixel. *Journal of Physics D: Applied Physics* vol. 43 Preprint at https://doi.org/10.1088/0022-3727/43/21/213001 (2010).
44. Ridgway, J. P. Cardiovascular magnetic resonance physics for clinicians: Part i. *Journal of Cardiovascular Magnetic Resonance* vol. 12 Preprint at https://doi.org/10.1186/1532-429X-12-71 (2010).
45. Lee, Y., Callaghan, M. F. & Nagy, Z. Analysis of the precision of variable flip angle T1 mapping with emphasis on the noise propagated from RF transmit field maps. *Front Neurosci* **11**, (2017).
46. Loening, N. M., Thrippleton, M. J., Keeler, J. & Griffin, R. G. Single-scan longitudinal relaxation measurements in high-resolution NMR spectroscopy. *Journal of Magnetic Resonance* **164**, 321–328 (2003).
47. Levitt, M. H. *Spin dynamics: basics of nuclear magnetic resonance*. (John Wiley & Sons, 2013).
48. Xu, L., Li, Q., Myers, M., Chen, Q. & Li, X. Application of nuclear magnetic resonance technology to carbon capture, utilization and storage: A review. *Journal of Rock Mechanics and Geotechnical Engineering* vol. 11 892–908 Preprint at https://doi.org/10.1016/j.jrmge.2019.01.003 (2019).
49. Lee, X. & Tsai, A. *Nuclear Magnetic Resonance and the Measurement of Relaxation Times of Acetone with Gadolinium*. (2006).
50. Wuu, Y.--R. *Nuclear Magnetic Resonance: Determination of T1 and T2 values for Oil, Methanol, and Water*.
51. Currie, S., Hoggard, N., Craven, I. J., Hadjivassiliou, M. & Wilkinson, I. D. Understanding MRI: Basic MR physics for physicians. *Postgraduate Medical Journal* vol. 89 209–223 Preprint at https://doi.org/10.1136/postgradmedj-2012-131342 (2013).
52. Warren, W. S., Jenista, E., Branca, R. T. & Chen, X. Increasing hyperpolarized spin lifetimes through true singlet eigenstates. *Science (1979)* **323**, 1711–1714 (2009).
53. Holmes, A. J. *et al.* The reaction of an iridium PNP complex with para hydrogen facilitates polarisation transfer without chemical change. *Dalton transactions* **44**, 1077–1083 (2015).
54. Zeng, H. *et al.* Optimization of SABRE for polarization of the tuberculosis drugs pyrazinamide and isoniazid. *Journal of magnetic resonance* **237**, 73–78 (2013).
55. Chekmenev, E. Y., Norton, V. A., Weitekamp, D. P. & Bhattacharya, P. Hyperpolarized 1H NMR employing low γ nucleus for spin polarization storage. *J Am Chem Soc* **131**, 3164–3165 (2009).
56. Pileio, G., Carravetta, M. & Levitt, M. H. Storage of nuclear magnetization as long-lived singlet order in low magnetic field. *Proceedings of the National Academy of Sciences* **107**, 17135–17139 (2010).
57. Roy, S. S., Rayner, P. J., Norcott, P., Green, G. G. R. & Duckett, S. B. Long-lived states to sustain SABRE hyperpolarised magnetisation. *Physical Chemistry Chemical Physics* **18**, 24905–24911 (2016).
58. Carravetta, M. & Levitt, M. H. Long-lived nuclear spin states in high-field solution NMR. *J Am Chem Soc* **126**, 6228–6229 (2004).
59. Carravetta, M., Johannessen, O. G. & Levitt, M. H. Beyond the T 1 limit: singlet nuclear spin states in low magnetic fields. *Phys Rev Lett* **92**, 153003 (2004).
60. Stevanato, G. *et al.* A nuclear singlet lifetime of more than one hour in room-temperature solution. *Angewandte Chemie* **127**, 3811–3814 (2015).

61. Tayler, M. C. D. *et al.* Direct enhancement of nuclear singlet order by dynamic nuclear polarization. *J Am Chem Soc* **134**, 7668–7671 (2012).
62. Harris, T. *et al.* Long-lived 15N hyperpolarization and rapid relaxation as a potential basis for repeated first pass perfusion imaging–marked effects of deuteration and temperature. *ChemPhysChem* **19**, 2148–2152 (2018).
63. Chiavazza, E., Viale, A., Karlsson, M. & Aime, S. 15N-permethylated amino acids as efficient probes for MRI-DNP applications. *Contrast Media Mol Imaging* **8**, 417–421 (2013).
64. Harris, T., Szekely, O. & Frydman, L. On the potential of hyperpolarized water in biomolecular NMR studies. *J Phys Chem B* **118**, 3281–3290 (2014).
65. Allouche-Arnon, H., Lerche, M. H., Karlsson, M., Lenkinski, R. E. & Katz-Brull, R. Deuteration of a molecular probe for DNP hyperpolarization–a new approach and validation for choline chloride. *Contrast Media Mol Imaging* **6**, 499–506 (2011).
66. Keshari, K. R. & Wilson, D. M. Chemistry and biochemistry of 13 C hyperpolarized magnetic resonance using dynamic nuclear polarization. *Chem Soc Rev* **43**, 1627–1659 (2014).
67. Hundshammer, C., Grashei, M., Greiner, A., Glaser, S. J. & Schilling, F. pH Dependence of T1 for 13C-Labelled Small Molecules Commonly Used for Hyperpolarized Magnetic Resonance Imaging. *ChemPhysChem* **20**, 798–802 (2019).
68. Chen, A. P. *et al.* In vivo hyperpolarized 13C MR spectroscopic imaging with 1H decoupling. *Journal of magnetic resonance* **197**, 100–106 (2009).
69. Allouche-Arnon, H., Lerche, M. H., Karlsson, M., Lenkinski, R. E. & Katz-Brull, R. Deuteration of a molecular probe for DNP hyperpolarization–a new approach and validation for choline chloride. *Contrast Media Mol Imaging* **6**, 499–506 (2011).
70. Grover, V. P. B. *et al.* Magnetic Resonance Imaging: Principles and Techniques: Lessons for Clinicians. *Journal of Clinical and Experimental Hepatology* vol. 5 246–255 Preprint at https://doi.org/10.1016/j.jceh.2015.08.001 (2015).
71. Jacobs, M. A., Ibrahim, T. S. & Ouwerkerk, R. MR imaging: brief overview and emerging applications. *Radiographics* **27**, 1213–1229 (2007).
72. McRobbie, D. W. Occupational exposure in MRI. *Br J Radiol* **85**, 293–312 (2012).
73. Hidalgo-Tobon, S. S. Theory of gradient coil design methods for magnetic resonance imaging. *Concepts in Magnetic Resonance Part A* **36**, 223–242 (2010).
74. Gruber, B., Froeling, M., Leiner, T. & Klomp, D. W. J. RF coils: A practical guide for nonphysicists. *J Magn Reson Imaging* **48**, 590–604 (2018).
75. Wachowicz, K. Evaluation of active and passive shimming in magnetic resonance imaging. *Res Rep Nucl Med* 1 (2014) doi:10.2147/rrnm.s46526.
76. Zhou, J. *et al.* An orthogonal shim coil for 3T brain imaging. *Magn Reson Med* **83**, 1499–1511 (2020).
77. Optimization magnetic resonance imaging shim coil using second derivative discretized stream function. *Concepts Magn Reson* (2017).
78. Lauterbur, P. C. Image formation by induced local interactions: examples employing nuclear magnetic resonance. *Nature* **242**, 190–191 (1973).
79. Davids, M., Guerin, B., Klein, V. & Wald, L. L. Optimization of MRI Gradient Coils With Explicit Peripheral Nerve Stimulation Constraints. *IEEE Trans Med Imaging* **40**, 129–142 (2021).
80. Webb, A. G. *Introduction to Biomedical Imaging*. (Wiley, 2017).
81. Lu, A., Daniel, B. L., Pauly, J. M. & Butts Pauly, K. Improved slice selection for R2* mapping during cryoablation with eddy current compensation. *Journal of magnetic resonance imaging.* **28**, 190–198 (2008).

82. Madelin, G. *et al.* Detection of acoustic waves by NMR using a radiofrequency field gradient. *Journal of Magnetic Resonance* **161**, 108–111 (2003).
83. Dabek, J. *et al.* Gradient-excitation encoding combined with frequency and phase encodings for three-dimensional ultra-low-field MRI. in *2012 Annual International Conference of the IEEE Engineering in Medicine and Biology Society* 1093–1097 (IEEE, 2012).
84. Deans, S. R. *The Radon transform and some of its applications*. (Courier Corporation, 2007).
85. Blank, A., Shapiro, G., Fischer, R., London, P. & Gershoni, D. Optically detected magnetic resonance imaging. *Appl Phys Lett* **106**, 034102 (2015).
86. Bryant, D. J., Payne, J. A., Firmin, D. N. & Longmore, D. B. Measurement of flow with NMR imaging using a gradient pulse and phase difference technique. *J Comput Assist Tomogr* **8**, 588–593 (1984).
87. DeLaPaz, R. L. Echo-planar imaging. *Radiographics* **14**, 1045–1058 (1994).
88. Magnetic resonance spectroscopy.
89. Levitt, M. H. The signs of frequencies and phases in NMR. *Journal of Magnetic Resonance* **126**, 164–182 (1997).
90. Pope, J. M. & Yao, S. Quantitative NMR imaging of flow. *Concepts Magn Reson* **5**, 281–302 (1993).
91. Viikinkoski, M. & Kaasalainen, M. Shape reconstruction from images: Pixel fields and Fourier transform. *Inverse Problems & Imaging* **8**, 885 (2014).
92. Chang, W.-T. *et al.* Improving the spatial resolution of magnetic resonance inverse imaging via the blipped-CAIPI acquisition scheme. *Neuroimage* **91**, 401–411 (2014).
93. Callaghan, P. T., Forde, L. C. & Rofe, C. J. Correlated susceptibility and diffusion effects in NMR microscopy using both phase-frequency encoding and phase-phase encoding. *J Magn Reson B* **104**, 34–52 (1994).
94. Magland, J. F., Wald, M. J. & Wehrli, F. W. Spin-echo micro-MRI of trabecular bone using improved 3D fast large-angle spin-echo (FLASE). *Magnetic Resonance in Medicine: An Official Journal of the International Society for Magnetic Resonance in Medicine* **61**, 1114–1121 (2009).
95. *Basics of Magnetic Resonance Imaging and Magnetic Resonance Spectroscopy*.
96. Jung, B. A. & Weigel, M. Spin echo magnetic resonance imaging. *Journal of Magnetic Resonance Imaging* **37**, 805–817 (2013).
97. Gebker, R., Schwitter, J., Fleck, E. & Nagel, E. How We Perform Myocardial Perfusion With Cardiovascular Magnetic Resonance. *J Cardiovasc Magn Reson* **9**, 539–547 (2007).
98. Friedman, B. R., Jones, J. P., Chavez-Munoz, G., Salmon, A. P. & Merritt, C. R. B. Principles of MRI. (1989).
99. Kuhn, L. T. & Akbey, Ü. *Hyperpolarization methods in NMR spectroscopy*. vol. 338 (Springer, 2013).
100. Hersman, F. W. *et al.* Large production system for hyperpolarized 129Xe for human lung imaging studies. *Acad Radiol* **15**, 683–692 (2008).
101. Duhamel, G. *et al.* Global and Regional Cerebral Blood Flow Measurements Using NMR of Injected Hyperpolarized Xenon-129. *Acad Radiol* **9**, S498–S500 (2002).
102. Norquay, G., Leung, G., Stewart, N. J., Wolber, J. & Wild, J. M. (129) Xe chemical shift in human blood and pulmonary blood oxygenation measurement in humans using hyperpolarized (129) Xe NMR. *Magn Reson Med* **77**, 1399–1408 (2017).
103. Driehuys, B. *et al.* Imaging alveolar–capillary gas transfer using hyperpolarized ¹²⁹Xe MRI. *Proceedings of the National Academy of Sciences* **103**, 18278 (2006).

104. Rao, M. R., Stewart, N. J., Griffiths, P. D., Norquay, G. & Wild, J. M. Imaging Human Brain Perfusion with Inhaled Hyperpolarized 129Xe MR Imaging. *Radiology* **286**, 659–665 (2017).
105. Chacon-Caldera, J. *et al.* Dissolved hyperpolarized xenon-129 MRI in human kidneys. *Magn Reson Med* **83**, (2019).
106. Walker, T. G. & Happer, W. Spin-exchange optical pumping of noble-gas nuclei. *Rev Mod Phys* **69**, 629–642 (1997).
107. Adrian, C. Helium-3 Shortage Could Put Freeze On Low-Temperature Research. *Science (1979)* **326**, 778–779 (2009).
108. Couch, M. J. *et al.* Pulmonary ultrashort echo time 19F MR imaging with inhaled fluorinated gas mixtures in healthy volunteers: feasibility. *Radiology* **269**, 903–909 (2013).
109. Schreiber, W. G. *et al.* Dynamic 19F-MRI of pulmonary ventilation using sulfur hexafluoride (SF6) gas. *Magnetic Resonance in Medicine: An Official Journal of the International Society for Magnetic Resonance in Medicine* **45**, 605–613 (2001).
110. Kuethe, D. O., Behr, V. C. & Begay, S. Volume of rat lungs measured throughout the respiratory cycle using 19F NMR of the inert gas SF6. *Magnetic Resonance in Medicine: An Official Journal of the International Society for Magnetic Resonance in Medicine* **48**, 547–549 (2002).
111. Kuethe, D. O., Caprihan, A., Gach, H. M., Lowe, I. J. & Fukushima, E. Imaging obstructed ventilation with NMR using inert fluorinated gases. *J Appl Physiol* (2000).
112. Adolphi, N. L. & Kuethe, D. O. Quantitative mapping of ventilation-perfusion ratios in lungs by 19F MR imaging of T1 of inert fluorinated gases. *Magnetic Resonance in Medicine: An Official Journal of the International Society for Magnetic Resonance in Medicine* **59**, 739–746 (2008).
113. Overhauser, A. W. Polarization of nuclei in metals. *Physical Review* **92**, 411 (1953).
114. Carver, T. R. & Slichter, C. P. Polarization of nuclear spins in metals. *Physical Review* **92**, 212 (1953).
115. Carver, T. R. & Slichter, C. P. Experimental verification of the Overhauser nuclear polarization effect. *Physical Review* **102**, 975 (1956).
116. Majee, S. B. *Emerging Concepts in Analysis and Applications of Hydrogels*. (IntechOpen, 2016).
117. de Boer, W. Dynamic orientation of nuclei at low temperatures. *J Low Temp Phys* **22**, 185–212 (1976).
118. Ardenkjær-Larsen, J. H. *et al.* Increase in signal-to-noise ratio of > 10,000 times in liquid-state NMR. *Proceedings of the National Academy of Sciences* **100**, 10158 (2003).
119. Ardenkjaer-Larsen, J. H. On the present and future of dissolution-DNP. *Journal of Magnetic Resonance* **264**, 3–12 (2016).
120. Lumata, L. *et al.* DNP by thermal mixing under optimized conditions yields> 60 000-fold enhancement of 89Y NMR signal. *J Am Chem Soc* **133**, 8673–8680 (2011).
121. Lumata, L. L. *et al.* Development and performance of a 129-GHz dynamic nuclear polarizer in an ultra-wide bore superconducting magnet. *Magnetic Resonance Materials in Physics, Biology and Medicine* **28**, 195–205 (2015).
122. Lumata, L. *et al.* Hyperpolarized 13C magnetic resonance and its use in metabolic assessment of cultured cells and perfused organs. *Methods Enzymol* **561**, 73–106 (2015).
123. Golman, K., in 't Zandt, R. & Thaning, M. Real-time metabolic imaging. *Proc Natl Acad Sci U S A* **103**, 11270–5 (2006).

124. Dutta, P., Martinez, G. v & Gillies, R. J. A New Horizon of DNP technology: Application to In-vivo (13)C Magnetic Resonance Spectroscopy and Imaging. *Biophys Rev* **5**, 271–281 (2013).
125. Ardenkjaer-Larsen, J. *et al.* Increase in signal-to-noise ratio of > 10,000 times in liquid-state NMR. *Proc Natl Acad Sci U S A* **100**, 10158–10163 (2003).
126. Albers, M. J. *et al.* Hyperpolarized ¹³C Lactate, Pyruvate, and Alanine: Noninvasive Biomarkers for Prostate Cancer Detection and Grading. *Cancer Res* **68**, 8607 (2008).
127. Witney, T. *et al.* A Comparison between Radiolabeled Fluorodeoxyglucose Uptake and Hyperpolarized 13C-Labeled Pyruvate Utilization as Methods for Detecting Tumor Response to Treatment 1 2. *Neoplasia* **11**, 574–582, 1 p following 582 (2009).
128. Kurhanewicz, J. *et al.* Analysis of Cancer Metabolism by Imaging Hyperpolarized Nuclei: Prospects for Translation to Clinical Research. *Neoplasia* **13**, 81–97 (2011).
129. Day, S. E. *et al.* Detecting tumor response to treatment using hyperpolarized 13C magnetic resonance imaging and spectroscopy. *Nat Med* **13**, 1382–1387 (2007).
130. Gallagher, F. A. *et al.* Production of hyperpolarized [1,4-13C2]malate from [1,4-13C2]fumarate is a marker of cell necrosis and treatment response in tumors. *Proceedings of the National Academy of Sciences* (2009) doi:10.1073/PNAS.0911447106.
131. Witney, T. H. *et al.* Detecting treatment response in a model of human breast adenocarcinoma using hyperpolarised [1-13C]pyruvate and [1,4-13C2]fumarate. *Br J Cancer* **103**, 1400–1406 (2010).
132. Kunkel, M. *et al.* Overexpression of Glut-1 and increased glucose metabolism in tumors are associated with a poor prognosis in patients with oral squamous cell carcinoma. *Cancer* **97**, 1015–1024 (2003).
133. Otto, W. On the Origin of Cancer Cells. *Science (1979)* **123**, 309–314 (1956).
134. Warburg, O., Wind, F. & Negelein, E. THE METABOLISM OF TUMORS IN THE BODY. *J Gen Physiol* **8**, 519–530 (1927).
135. Ahola, S. *et al.* Ultrafast multidimensional Laplace NMR for a rapid and sensitive chemical analysis. *Nat Commun* **6**, 1–7 (2015).
136. Wagner, S. Conversion rate of para-hydrogen to ortho-hydrogen by oxygen: implications for PHIP gas storage and utilization. *Magnetic Resonance Materials in Physics, Biology and Medicine* **27**, 195–199 (2014).
137. Bowers, C. R. & Weitekamp, D. P. Parahydrogen and synthesis allow dramatically enhanced nuclear alignment. *J Am Chem Soc* **109**, 5541–5542 (1987).
138. Duckett, S. B. & Wood, N. J. Parahydrogen-based NMR methods as a mechanistic probe in inorganic chemistry. *Coord Chem Rev* **252**, 2278–2291 (2008).
139. Bhattacharya, P. *et al.* Parahydrogen-induced polarization (PHIP) hyperpolarized MR receptor imaging in vivo: a pilot study of 13C imaging of atheroma in mice. *NMR Biomed* **24**, 1023–1028 (2011).
140. Zacharias, N. M., Chan, H. R., Sailasuta, N., Ross, B. D. & Bhattacharya, P. Real-time molecular imaging of tricarboxylic acid cycle metabolism in vivo by hyperpolarized 1-13C diethyl succinate. *J Am Chem Soc* **134**, 934–943 (2012).
141. Plaumann, M. *et al.* Parahydrogen-Induced Polarization Transfer to 19F in Perfluorocarbons for 19F NMR Spectroscopy and MRI. *Chemistry–A European Journal* **19**, 6334–6339 (2013).
142. Farkas, A. *Orthohydrogen, parahydrogen and heavy hydrogen*. (CUP Archive, 1935).
143. Trapnell, B. M. W. Parahydrogen and Orthodeuterium Conversions and Hydrogen/Deuterium Exchange. *Catalysis* **3**, 1 (1956).

144. Feng, B., Coffey, A. M., Colon, R. D., Chekmenev, E. Y. & Waddell, K. W. A pulsed injection parahydrogen generator and techniques for quantifying enrichment. *Journal of Magnetic Resonance* **214**, 258–262 (2012).
145. Bowers, C. R. & Weitekamp, D. P. Transformation of symmetrization order to nuclear-spin magnetization by chemical reaction and nuclear magnetic resonance. *Phys Rev Lett* **57**, 2645 (1986).
146. Bowers, C. R. & Weitekamp, D. P. Parahydrogen and synthesis allow dramatically enhanced nuclear alignment. *J Am Chem Soc* **109**, 5541–5542 (1987).
147. Eisenschmid, T. C. *et al.* Para hydrogen induced polarization in hydrogenation reactions. *J Am Chem Soc* **109**, 8089–8091 (1987).
148. Pravica, M. G. & Weitekamp, D. P. Net NMR alignment by adiabatic transport of parahydrogen addition products to high magnetic field. *Chem Phys Lett* **145**, 255–258 (1988).
149. Osborn, J. A., Jardine, F. H., Young, J. F. & Wilkinson, G. The preparation and properties of tris(triphenylphosphine)halogenorhodium(I) and some reactions thereof including catalytic homogeneous hydrogenation of olefins and acetylenes and their derivatives. *Journal of the Chemical Society A: Inorganic, Physical, Theoretical* 1711–1732 (1966) doi:10.1039/J19660001711.
150. Crabtree, R. H., Mihelcic, J. M. & Quirk, J. M. Iridium complexes in alkane dehydrogenation. *J Am Chem Soc* **101**, 7738–7740 (1979).
151. Horiuti, I. & Polanyi, M. Exchange reactions of hydrogen on metallic catalysts. *Transactions of the Faraday Society* **30**, 1164–1172 (1934).
152. Kuhn, L. T. & Akbey, Ü. *Hyperpolarization methods in NMR spectroscopy*. vol. 338 (Springer, 2013).
153. Glöggler, S. *et al.* A nanoparticle catalyst for heterogeneous phase para-hydrogen-induced polarization in water. *Angewandte Chemie International Edition* **54**, 2452–2456 (2015).
154. Fekete, M., Rayner, P. J., Green, G. G. R. & Duckett, S. B. Harnessing polarisation transfer to indazole and imidazole through signal amplification by reversible exchange to improve their NMR detectability. *Magn Reson Chem* **55**, 944–957 (2017).
155. Duckett, S. B. & Mewis, R. E. Application of para hydrogen induced polarization techniques in NMR spectroscopy and imaging. *Acc Chem Res* **45**, 1247–1257 (2012).
156. Reineri, F., Boi, T. & Aime, S. Parahydrogen induced polarization of 13 C carboxylate resonance in acetate and pyruvate. *Nat Commun* **6**, 1–6 (2015).
157. Cavallari, E. *et al.* The 13 C hyperpolarized pyruvate generated by ParaHydrogen detects the response of the heart to altered metabolism in real time. *Sci Rep* **8**, 1–9 (2018).
158. Nikolaou, P., Goodson, B. M. & Chekmenev, E. Y. NMR hyperpolarization techniques for biomedicine. *Chemistry* **21**, 3156 (2015).
159. Adams, R. W. *et al.* Reversible interactions with para-hydrogen enhance NMR sensitivity by polarization transfer. *Science (1979)* **323**, 1708–1711 (2009).
160. Hövener, J.-B. *et al.* A hyperpolarized equilibrium for magnetic resonance. *Nat Commun* **4**, 1–5 (2013).
161. Richardson, P. M. *et al.* A simple hand-held magnet array for efficient and reproducible SABRE hyperpolarisation using manual sample shaking. *Magnetic Resonance in Chemistry* **56**, 641–650 (2018).
162. Suggs, J. W., Cox, S. D., Crabtree, R. H. & Quirk, J. M. Facile homogeneous hydrogenations of hindered olefins with [Ir(cod)py(PCy3)]PF6. *Tetrahedron Lett* **22**, 303–306 (1981).

163. Atkinson, K. D. *et al.* Para-hydrogen induced polarization without incorporation of para-hydrogen into the analyte. *Inorg Chem* **48**, 663–670 (2009).
164. Cowley, M. J. *et al.* Iridium N-Heterocyclic Carbene Complexes as Efficient Catalysts for Magnetization Transfer from para-Hydrogen. *J Am Chem Soc* **133**, 6134–6137 (2011).
165. Boehme, C. & Frenking, G. Electronic Structure of Stable Carbenes, Silylenes, and Germylenes. *J Am Chem Soc* **118**, 2039–2046 (1996).
166. Díez-González, S. & Nolan, S. P. Stereoelectronic parameters associated with N-heterocyclic carbene (NHC) ligands: A quest for understanding. *Coord Chem Rev* **251**, 874–883 (2007).
167. Adams, R. W., Duckett, S. B., Green, R. A., Williamson, D. C. & Green, G. G. R. A theoretical basis for spontaneous polarization transfer in non-hydrogenative para hydrogen-induced polarization. *J Chem Phys* **131**, 194505 (2009).
168. Lloyd, L. S. *et al.* Hyperpolarisation through reversible interactions with para hydrogen. *Catal Sci Technol* **4**, 3544–3554 (2014).
169. Mewis, R. E. Developments and advances concerning the hyperpolarisation technique SABRE. *Magnetic Resonance in Chemistry* **53**, 789–800 (2015).
170. Atkinson, K. D. *et al.* Para-hydrogen induced polarization without incorporation of para-hydrogen into the analyte. *Inorg Chem* **48**, 663–670 (2009).
171. Atkinson, K. D. *et al.* Spontaneous transfer of para hydrogen derived spin order to pyridine at low magnetic field. *J Am Chem Soc* **131**, 13362–13368 (2009).
172. Díez-González, S. & Nolan, S. P. Stereoelectronic parameters associated with N-heterocyclic carbene (NHC) ligands: A quest for understanding. *Coord Chem Rev* **251**, 874–883 (2007).
173. Vázquez-Serrano, L. D., Owens, B. T. & Buriak, J. M. Catalytic olefin hydrogenation using N-heterocyclic carbene–phosphine complexes of iridium. *Chemical communications* 2518–2519 (2002).
174. Rayner, P. J., Burns, M. J., Fear, E. J. & Duckett, S. B. Steric and Electronic Effects on the 1 H Hyperpolarisation of Substituted Pyridazines by Signal Amplification by Reversible Exchange. *Magn Reson Chem* (2021).
175. van Weerdenburg, B. J. A. *et al.* Ligand effects of NHC–iridium catalysts for signal amplification by reversible exchange (SABRE). *Chemical Communications* **49**, 7388–7390 (2013).
176. Lloyd, L. S. *et al.* Hyperpolarisation through reversible interactions with para hydrogen. *Catal Sci Technol* **4**, 3544–3554 (2014).
177. Tolman, C. A. Phosphorus ligand exchange equilibriums on zerovalent nickel. Dominant role for steric effects. *J Am Chem Soc* **92**, 2956–2965 (1970).
178. Poater, A. *et al.* SambVca: A web application for the calculation of the buried volume of N-heterocyclic carbene ligands. Preprint at (2009).
179. Clavier, H. & Nolan, S. P. Percent buried volume for phosphine and N-heterocyclic carbene ligands: steric properties in organometallic chemistry. *Chemical communications* **46**, 841–861 (2010).
180. Kelly Iii, R. A. *et al.* Determination of N-heterocyclic carbene (NHC) steric and electronic parameters using the [(NHC) Ir (CO) 2Cl] system. *Organometallics* **27**, 202–210 (2008).
181. Vazquez-Serrano, L. D., Owens, B. T. & Buriak, J. M. The search for new hydrogenation catalyst motifs based on N-heterocyclic carbene ligands. *Inorganica Chim Acta* **359**, 2786–2797 (2006).
182. Iali, W. *et al.* Hyperpolarising Pyruvate through Signal Amplification by Reversible Exchange (SABRE). *Angewandte Chemie* **131**, 10377–10381 (2019).

183. Rayner, P. J. & Duckett, S. B. Signal amplification by reversible exchange (SABRE): From discovery to diagnosis. *Angewandte Chemie International Edition* **57**, 6742–6753 (2018).
184. Ivanov, K. L., Pravdivtsev, A. N., Yurkovskaya, A. v, Vieth, H.-M. & Kaptein, R. The role of level anti-crossings in nuclear spin hyperpolarization. *Prog Nucl Magn Reson Spectrosc* **81**, 1–36 (2014).
185. Pravdivtsev, A. N., Yurkovskaya, A. v, Vieth, H., Ivanov, K. L. & Kaptein, R. Level Anti-Crossings are a Key Factor for Understanding para-Hydrogen-Induced Hyperpolarization in SABRE Experiments. *ChemPhysChem* **14**, 3327–3331 (2013).
186. Burns, M. J. *et al.* Improving the Hyperpolarization of 31P Nuclei by Synthetic Design. *J Phys Chem B* **119**, 5020–5027 (2015).
187. Administration, F. and D. Guidance for industry, PAT-A framework for innovative pharmaceutical development, manufacturing and quality assurance. *http://www. fda. gov/cder/guidance/published. html* (2004).
188. Rathore, A. S., Bhambure, R. & Ghare, V. Process analytical technology (PAT) for biopharmaceutical products. *Anal Bioanal Chem* **398**, 137–154 (2010).
189. Blümich, B. Introduction to compact NMR: A review of methods. *TrAC Trends in Analytical Chemistry* **83**, 2–11 (2016).
190. Meyer, K., Kern, S., Zientek, N., Guthausen, G. & Maiwald, M. Process control with compact NMR. *TrAC Trends in Analytical Chemistry* **83**, 39–52 (2016).
191. Semenova, O. *et al.* Reaction monitoring using SABRE-hyperpolarized benchtop (1 T) NMR spectroscopy. *Anal Chem* **91**, 6695–6701 (2019).
192. Frydman, L. & Blazina, D. Ultrafast two-dimensional nuclear magnetic resonance spectroscopy of hyperpolarized solutions. *Nat Phys* **3**, 415–419 (2007).
193. Lloyd, L. S. *et al.* Utilization of SABRE-derived hyperpolarization to detect low-concentration analytes via 1D and 2D NMR methods. *J Am Chem Soc* **134**, 12904–12907 (2012).
194. Chae, H. *et al.* Organic Reaction Monitoring of a Glycine Derivative Using Signal Amplification by Reversible Exchange-Hyperpolarized Benchtop Nuclear Magnetic Resonance Spectroscopy. *Anal Chem* **92**, 10902–10907 (2020).
195. Jeong, H. J. *et al.* Signal amplification by reversible exchange for COVID-19 antiviral drug candidates. *Sci Rep* **10**, 14290 (2020).
196. Hill-Casey, F. *et al.* In Situ SABRE Hyperpolarization with Earth's Field NMR Detection. *Molecules* **24**, 4126 (2019).
197. Barskiy, D. A. *et al.* In situ and ex situ low-field NMR spectroscopy and MRI endowed by SABRE hyperpolarization. *Chemphyschem* **15**, 4100 (2014).
198. Daniele, V., Legrand, F.-X., Berthault, P., Dumez, J.-N. & Huber, G. Single-scan multidimensional NMR analysis of mixtures at sub-millimolar concentrations by using SABRE hyperpolarization. *ChemPhysChem* **16**, 3413–3417 (2015).
199. Truong, M. L. *et al.* Irreversible catalyst activation enables hyperpolarization and water solubility for NMR signal amplification by reversible exchange. *J Phys Chem B* **118**, 13882–13889 (2014).
200. Marion, N., Díez-González, S. & Nolan, S. P. N-heterocyclic carbenes as organocatalysts. *Angewandte Chemie International Edition* **46**, 2988–3000 (2007).
201. Norcott, P., Burns, M. J., Rayner, P. J., Mewis, R. E. & Duckett, S. B. Using 2H labelling to improve the NMR detectability of pyridine and its derivatives by SABRE. *Magnetic Resonance in Chemistry* **56**, 663–671 (2018).
202. Glöggler, S. *et al.* Para-hydrogen induced polarization of amino acids, peptides and deuterium–hydrogen gas. *Physical Chemistry Chemical Physics* **13**, 13759–13764 (2011).

203. Olaru, A. M. *et al.* Creating a hyperpolarised pseudo singlet state through polarisation transfer from para hydrogen under SABRE. *Chemical Communications* **52**, 7842–7845 (2016).
204. Glöggler, S. *et al.* Selective drug trace detection with low-field NMR. *Analyst* **136**, 1566–1568 (2011).
205. Appleby, K. M. *et al.* Investigating pyridazine and phthalazine exchange in a series of iridium complexes in order to define their role in the catalytic transfer of magnetisation from para-hydrogen. *Chem Sci* **6**, 3981–3993 (2015).
206. Reile, I. *et al.* NMR detection in biofluid extracts at sub-μM concentrations via para-H 2 induced hyperpolarization. *Analyst* **141**, 4001–4005 (2016).
207. Baumann, M. & Baxendale, I. R. An overview of the synthetic routes to the best selling drugs containing 6-membered heterocycles. *Beilstein Journal of Organic Chemistry* **9**, 2265–2319 (2013).
208. Altaf, A. A. *et al.* A review on the medicinal importance of pyridine derivatives. *J. Drug Des. Med. Chem* **1**, 1–11 (2015).
209. Pravdivtsev, A. N., Yurkovskaya, A. v, Vieth, H., Ivanov, K. L. & Kaptein, R. Level Anti-Crossings are a Key Factor for Understanding para-Hydrogen-Induced Hyperpolarization in SABRE Experiments. *ChemPhysChem* **14**, 3327–3331 (2013).
210. Barskiy, D. A., Pravdivtsev, A. N., Ivanov, K. L., Kovtunov, K. v & Koptyug, I. v. A simple analytical model for signal amplification by reversible exchange (SABRE) process. *Physical Chemistry Chemical Physics* **18**, 89–93 (2016).
211. Pravdivtsev, A. N., Yurkovskaya, A. v, Vieth, H.-M. & Ivanov, K. L. RF-SABRE: a way to continuous spin hyperpolarization at high magnetic fields. *J Phys Chem B* **119**, 13619–13629 (2015).
212. Roy, S. S., Stevanato, G., Rayner, P. J. & Duckett, S. B. Direct enhancement of nitrogen-15 targets at high-field by fast ADAPT-SABRE. *Journal of Magnetic Resonance* **285**, 55–60 (2017).
213. Theis, T., Truong, M., Coffey, A. M., Chekmenev, E. Y. & Warren, W. S. LIGHT-SABRE enables efficient in-magnet catalytic hyperpolarization. *Journal of Magnetic Resonance* **248**, 23–26 (2014).
214. Theis, T. *et al.* Microtesla SABRE enables 10% nitrogen-15 nuclear spin polarization. *J Am Chem Soc* **137**, 1404–1407 (2015).
215. Truong, M. L. *et al.* 15N hyperpolarization by reversible exchange using SABRE-SHEATH. *The journal of physical chemistry C* **119**, 8786–8797 (2015).
216. Skovpin, I. v *et al.* (15) N Hyperpolarization of Dalfampridine at Natural Abundance for Magnetic Resonance Imaging. *Chemistry* **25**, 12694–12697 (2019).
217. Shchepin, R. v *et al.* 15N hyperpolarization of imidazole-15N2 for magnetic resonance pH sensing via SABRE-SHEATH. *ACS Sens* **1**, 640–644 (2016).
218. Barskiy, D. A. *et al.* Over 20% 15N Hyperpolarization in Under One Minute for Metronidazole, an Antibiotic and Hypoxia Probe. *J Am Chem Soc* **138**, 8080–8083 (2016).
219. Shen, K. *et al.* Diazirines as potential molecular imaging tags: Probing the requirements for efficient and long-lived SABRE-induced hyperpolarization. *Angewandte Chemie* **129**, 12280–12284 (2017).
220. Thomas, T. *et al.* Direct and cost-efficient hyperpolarization of long-lived nuclear spin states on universal 15N2-diazirine molecular tags. *Sci Adv* **2**, e1501438 (2021).
221. Atkinson, K. D. *et al.* Spontaneous transfer of para hydrogen derived spin order to pyridine at low magnetic field. *J Am Chem Soc* **131**, 13362–13368 (2009).
222. Truong, M. L. *et al.* 15N Hyperpolarization by Reversible Exchange Using SABRE-SHEATH. *The Journal of Physical Chemistry C* **119**, 8786–8797 (2015).

223. Barskiy, D. A. *et al.* The absence of quadrupolar nuclei facilitates efficient 13C hyperpolarization via reversible exchange with parahydrogen. *ChemPhysChem* **18**, 1493–1498 (2017).
224. TomHon, P. *et al.* Temperature Cycling Enables Efficient 13C SABRE-SHEATH Hyperpolarization and Imaging of [1-13C] Pyruvate. (2021).
225. Roy, S. S., Appleby, K. M., Fear, E. J. & Duckett, S. B. SABRE-Relay: a versatile route to hyperpolarization. *J Phys Chem Lett* **9**, 1112–1117 (2018).
226. Rayner, P. J. *et al.* Relayed hyperpolarization from para-hydrogen improves the NMR detectability of alcohols. *Chem Sci* **10**, 7709–7717 (2019).
227. Iali, W., Rayner, P. J. & Duckett, S. B. Using parahydrogen to hyperpolarize amines, amides, carboxylic acids, alcohols, phosphates, and carbonates. *Sci Adv* **4**, eaao6250 (2018).
228. Tickner, B. J. *et al.* Using coligands to gain mechanistic insight into iridium complexes hyperpolarized with para-hydrogen. *Chem Sci* **10**, 5235–5245 (2019).
229. Rayner, P., Gillions, J., Hannibal, V., John, R. & Duckett, S. Hyperpolarisation of weakly binding N-heterocycles using Signal Amplification by Reversible Exchange. *Chem Sci* **12**, (2021).
230. Tickner, B. J. *et al.* Optimisation of pyruvate hyperpolarisation using SABRE by tuning the active magnetisation transfer catalyst. *Catal Sci Technol* **10**, 1343–1355 (2020).
231. Tickner, B. J., Lewis, J. S., John, R. O., Whitwood, A. C. & Duckett, S. B. Mechanistic insight into novel sulfoxide containing SABRE polarisation transfer catalysts. *Dalton Transactions* **48**, 15198–15206 (2019).
232. Dücker, E. B., Kuhn, L. T., Münnemann, K. & Griesinger, C. Similarity of SABRE field dependence in chemically different substrates. *Journal of Magnetic Resonance* **214**, 159–165 (2012).
233. Rayner, P. J. *et al.* Delivering strong 1H nuclear hyperpolarization levels and long magnetic lifetimes through signal amplification by reversible exchange. *Proceedings of the National Academy of Sciences* **114**, E3188–E3194 (2017).
234. Iali, W., Olaru, A. M., Green, G. G. R. & Duckett, S. B. Achieving High Levels of NMR-Hyperpolarization in Aqueous Media With Minimal Catalyst Contamination Using SABRE. *Chemistry* **23**, 10491–10495 (2017).
235. Olaru, A. M., Burns, M. J., Green, G. G. R. & Duckett, S. B. SABRE hyperpolarisation of vitamin B3 as a function of pH. *Chem Sci* **8**, 2257–2266 (2017).
236. Hirschhaeuser, F., Sattler, U. G. A. & Mueller-Klieser, W. Lactate: a metabolic key player in cancer. *Cancer Res* **71**, 6921–6925 (2011).
237. DeVience, S. J. *et al.* Metabolic imaging of energy metabolism in traumatic brain injury using hyperpolarized [1-13 C] pyruvate. *Sci Rep* **7**, 1–7 (2017).
238. Nelson, S. J. *et al.* Metabolic imaging of patients with prostate cancer using hyperpolarized [1-13C] pyruvate. *Sci Transl Med* **5**, 198ra108-198ra108 (2013).
239. Lau, A. Z. *et al.* Rapid multislice imaging of hyperpolarized 13C pyruvate and bicarbonate in the heart. *Magn Reson Med* **64**, 1323–1331 (2010).
240. Grist, J. T. *et al.* Quantifying normal human brain metabolism using hyperpolarized [1–13C] pyruvate and magnetic resonance imaging. *Neuroimage* **189**, 171–179 (2019).
241. Pourfathi, M. *et al.* In vivo imaging of the progression of acute lung injury using hyperpolarized [1-13C] pyruvate. *Magn Reson Med* **78**, 2106–2115 (2017).
242. Gray, L. R., Tompkins, S. C. & Taylor, E. B. Regulation of pyruvate metabolism and human disease. *Cellular and molecular life sciences* **71**, 2577–2604 (2014).

243. Cheng, S.-C., Nakamura, R. & Waelsch, H. Relative contribution of carbon dioxide fixation and acetyl-CoA pathways in two nervous tissues. *Nature* **216**, 928–929 (1967).
244. Patel, M. S., Grover, W. D. & Auerbach, V. H. Pyruvate metabolism by homogenates of human brain: effects of phenylpyruvate and implications for the etiology of the mental retardation in phenylketonuria. *J Neurochem* **20**, 289–296 (1973).
245. Mazurek, S., Grimm, H., Boschek, C. B., Vaupel, P. & Eigenbrodt, E. Pyruvate kinase type M2: a crossroad in the tumor metabolome. *British Journal of Nutrition* **87**, S23–S29 (2002).
246. K, B. D. *et al.* A Mitochondrial Pyruvate Carrier Required for Pyruvate Uptake in Yeast, Drosophila, and Humans. *Science (1979)* **337**, 96–100 (2012).
247. Sébastien, H. *et al.* Identification and Functional Expression of the Mitochondrial Pyruvate Carrier. *Science (1979)* **337**, 93–96 (2012).
248. Zangari, J., Petrelli, F., Maillot, B. & Martinou, J.-C. The multifaceted pyruvate metabolism: role of the mitochondrial pyruvate carrier. *Biomolecules* **10**, 1068 (2020).
249. McCommis, K. S. & Finck, B. N. Mitochondrial pyruvate transport: a historical perspective and future research directions. *Biochemical journal* **466**, 443–454 (2015).
250. Alegría, L. *et al.* A hypoperfusion context may aid to interpret hyperlactatemia in sepsis-3 septic shock patients: a proof-of-concept study. *Ann Intensive Care* **7**, 29 (2017).
251. Varis, E. *et al.* Evolution of Blood Lactate and 90-Day Mortality in Septic Shock. A Post Hoc Analysis of the FINNAKI Study. *Shock* **47**, (2017).
252. Bouzat, P. *et al.* Cerebral metabolic effects of exogenous lactate supplementation on the injured human brain. *Intensive Care Med* **40**, 412–421 (2014).
253. Suzuki, A. *et al.* Astrocyte-Neuron Lactate Transport Is Required for Long-Term Memory Formation. *Cell* **144**, 810–823 (2011).
254. Jourdain, P. *et al.* L-Lactate protects neurons against excitotoxicity: implication of an ATP-mediated signaling cascade. *Sci Rep* **6**, 21250 (2016).
255. Dienel, G. A. Brain Lactate Metabolism: The Discoveries and the Controversies. *Journal of Cerebral Blood Flow & Metabolism* **32**, 1107–1138 (2011).
256. Morgan-Parkes, J. H. Metastases: mechanisms, pathways, and cascades. *AJR Am J Roentgenol* **164**, 1075–1082 (1995).
257. Schmidt-Kittler, O. *et al.* From latent disseminated cells to overt metastasis: genetic analysis of systemic breast cancer progression. *Proceedings of the National Academy of Sciences* **100**, 7737–7742 (2003).
258. Cohen, S. J. *et al.* Prognostic significance of circulating tumor cells in patients with metastatic colorectal cancer. *Annals of oncology* **20**, 1223–1229 (2009).
259. Pierga, J.-Y. *et al.* High independent prognostic and predictive value of circulating tumor cells compared with serum tumor markers in a large prospective trial in first-line chemotherapy for metastatic breast cancer patients. *Annals of oncology* **23**, 618–624 (2012).
260. Thalgott, M. *et al.* Detection of circulating tumor cells in different stages of prostate cancer. *J Cancer Res Clin Oncol* **139**, 755–763 (2013).
261. Butler, T. P. & Gullino, P. M. Quantitation of cell shedding into efferent blood of mammary adenocarcinoma. *Cancer Res* **35**, 512–516 (1975).
262. Condeelis, J. & Pollard, J. W. Macrophages: obligate partners for tumor cell migration, invasion, and metastasis. *Cell* **124**, 263–266 (2006).
263. Fidler, I. J., Yano, S., Zhang, R., Fujimaki, T. & Bucana, C. D. The seed and soil hypothesis: vascularisation and brain metastases. *Lancet Oncol* **3**, 53–57 (2002).

264. Condeelis, J. S., Wyckoff, J. & Segall, J. E. Imaging of cancer invasion and metastasis using green fluorescent protein. *Eur J Cancer* **36**, 1671–1680 (2000).
265. Chang, Y. S. *et al.* Mosaic blood vessels in tumors: frequency of cancer cells in contact with flowing blood. *Proceedings of the National Academy of Sciences* **97**, 14608–14613 (2000).
266. Bockhorn, M., Roberge, S., Sousa, C., Jain, R. K. & Munn, L. L. Differential gene expression in metastasizing cells shed from kidney tumors. *Cancer Res* **64**, 2469–2473 (2004).
267. Nagy, J. A., Chang, S. H., Dvorak, A. M. & Dvorak, H. F. Why are tumour blood vessels abnormal and why is it important to know? *Br J Cancer* **100**, 865–869 (2009).
268. Fidler, I. J. Metastasis: quantitative analysis of distribution and fate of tumor emboli labeled with 125I-5-iodo-2′-deoxyuridine. *J Natl Cancer Inst* **45**, 773–782 (1970).
269. Luzzi, K. J. *et al.* Multistep nature of metastatic inefficiency: dormancy of solitary cells after successful extravasation and limited survival of early micrometastases. *Am J Pathol* **153**, 865–873 (1998).
270. Warburg, O. On respiratory impairment in cancer cells. *Science (1979)* **124**, 269–270 (1956).
271. vander Heiden, M. G., Cantley, L. C. & Thompson, C. B. Understanding the Warburg effect: the metabolic requirements of cell proliferation. *Science (1979)* **324**, 1029–1033 (2009).
272. Fantin, V. R., St-Pierre, J. & Leder, P. Attenuation of LDH-A expression uncovers a link between glycolysis, mitochondrial physiology, and tumor maintenance. *Cancer Cell* **9**, 425–434 (2006).
273. Moreno-Sánchez, R., Rodríguez-Enríquez, S., Marín-Hernández, A. & Saavedra, E. Energy metabolism in tumor cells. *FEBS J* **274**, 1393–1418 (2007).
274. Weinhouse, S. The Warburg hypothesis fifty years later. *Zeitschrift für Krebsforschung und Klinische Onkologie* **87**, 115–126 (1976).
275. Guppy, M., Leedman, P., Zu, X. & Russell, V. Contribution by different fuels and metabolic pathways to the total ATP turnover of proliferating MCF-7 breast cancer cells. *Biochemical Journal* **364**, 309–315 (2002).
276. Molina, J. R. *et al.* An inhibitor of oxidative phosphorylation exploits cancer vulnerability. *Nat Med* **24**, 1036–1046 (2018).
277. Viale, A. *et al.* Oncogene ablation-resistant pancreatic cancer cells depend on mitochondrial function. *Nature* **514**, 628–632 (2014).
278. Lu, J., Tan, M. & Cai, Q. The Warburg effect in tumor progression: mitochondrial oxidative metabolism as an anti-metastasis mechanism. *Cancer Lett* **356**, 156–164 (2015).
279. Stacpoole, P. W. Therapeutic targeting of the pyruvate dehydrogenase complex/pyruvate dehydrogenase kinase (PDC/PDK) axis in cancer. *JNCI: Journal of the National Cancer Institute* **109**, (2017).
280. Jin, Y. *et al.* Src drives the Warburg effect and therapy resistance by inactivating pyruvate dehydrogenase through tyrosine-289 phosphorylation. *Oncotarget* **7**, 25113 (2016).
281. Fan, J. *et al.* Tyr-301 phosphorylation inhibits pyruvate dehydrogenase by blocking substrate binding and promotes the Warburg effect. *Journal of Biological Chemistry* **289**, 26533–26541 (2014).
282. Levine, A. J. & Puzio-Kuter, A. M. The control of the metabolic switch in cancers by oncogenes and tumor suppressor genes. *Science (1979)* **330**, 1340–1344 (2010).
283. Hu, J. *et al.* Heterogeneity of tumor-induced gene expression changes in the human metabolic network. *Nat Biotechnol* **31**, 522–529 (2013).

284. Birsoy, K. *et al.* Metabolic determinants of cancer cell sensitivity to glucose limitation and biguanides. *Nature* **508**, 108–112 (2014).
285. Piskounova, E. *et al.* Oxidative stress inhibits distant metastasis by human melanoma cells. *Nature* **527**, 186–191 (2015).
286. Kamarajugadda, S. *et al.* Manganese superoxide dismutase promotes anoikis resistance and tumor metastasis. *Cell Death Dis* **4**, e504–e504 (2013).
287. Oberley, L. W. Free radicals and diabetes. *Free Radic Biol Med* **5**, 113–124 (1988).
288. Gorrini, C., Harris, I. S. & Mak, T. W. Modulation of oxidative stress as an anticancer strategy. *Nat Rev Drug Discov* **12**, 931–947 (2013).
289. Handschin, C. & Spiegelman, B. M. Peroxisome proliferator-activated receptor γ coactivator 1 coactivators, energy homeostasis, and metabolism. *Endocr Rev* **27**, 728–735 (2006).
290. Torrano, V. *et al.* The metabolic co-regulator PGC1α suppresses prostate cancer metastasis. *Nat Cell Biol* **18**, 645–656 (2016).
291. Luo, C. *et al.* A PGC1α-mediated transcriptional axis suppresses melanoma metastasis. *Nature* **537**, 422–426 (2016).
292. Andrzejewski, S. *et al.* PGC-1α promotes breast cancer metastasis and confers bioenergetic flexibility against metabolic drugs. *Cell Metab* **26**, 778–787 (2017).
293. St-Pierre, J. *et al.* Suppression of reactive oxygen species and neurodegeneration by the PGC-1 transcriptional coactivators. *Cell* **127**, 397–408 (2006).
294. Austin, S. & St-Pierre, J. PGC1α and mitochondrial metabolism–emerging concepts and relevance in ageing and neurodegenerative disorders. *J Cell Sci* **125**, 4963–4971 (2012).
295. Cavallari, E. *et al.* In-vitro NMR Studies of Prostate Tumor Cell Metabolism by Means of Hyperpolarized [1-13C]Pyruvate Obtained Using the PHIP-SAH Method. *Front Oncol* **10**, (2020).
296. Cavallari, E. *et al.* The 13C hyperpolarized pyruvate generated by ParaHydrogen detects the response of the heart to altered metabolism in real time. *Sci Rep* **8**, (2018).
297. Natterer, J. & Bargon, J. Parahydrogen induced polarization. *Prog Nucl Magn Reson Spectrosc* **31**, 293–315 (1997).
298. Olsson, L. E. *et al.* MR coronary angiography in pigs with intraarterial injections of a hyperpolarized 13C substance. *Magnetic Resonance in Medicine: An Official Journal of the International Society for Magnetic Resonance in Medicine* **55**, 731–737 (2006).
299. Golman, K. *et al.* Parahydrogen-induced polarization in imaging: Subsecond 13C angiography. *Magnetic Resonance in Medicine: An Official Journal of the International Society for Magnetic Resonance in Medicine* **46**, 1–5 (2001).
300. Hövener, J. *et al.* Parahydrogen-based hyperpolarization for biomedicine. *Angewandte Chemie International Edition* **57**, 11140–11162 (2018).
301. Reineri, F., Cavallari, E., Carrera, C. & Aime, S. Hydrogenative-PHIP polarized metabolites for biological studies. *Magnetic Resonance Materials in Physics, Biology and Medicine* **34**, 25–47 (2021).
302. Nelson, S. J. *et al.* Metabolic imaging of patients with prostate cancer using hyperpolarized [1-13C] pyruvate. *Sci Transl Med* **5**, 198ra108-198ra108 (2013).
303. Kurhanewicz, J. *et al.* Hyperpolarized 13C MRI: path to clinical translation in oncology. *Neoplasia* **21**, 1–16 (2019).
304. Serrao, E. M. & Brindle, K. M. Potential clinical roles for metabolic imaging with hyperpolarized [1-13C] pyruvate. *Front Oncol* **6**, 59 (2016).
305. Cunningham, C. H. *et al.* Hyperpolarized 13C metabolic MRI of the human heart: initial experience. *Circ Res* **119**, 1177–1182 (2016).

306. Gallagher, F. A. *et al.* Imaging breast cancer using hyperpolarized carbon-13 MRI. *Proceedings of the National Academy of Sciences* **117**, 2092–2098 (2020).
307. Dagys, L. *et al.* Nuclear hyperpolarization of (1-13C)-pyruvate in aqueous solution by proton-relayed side-Arm hydrogenation. *Analyst* **146**, 1772–1778 (2021).
308. Cavallari, E., Carrera, C., Aime, S. & Reineri, F. Studies to enhance the hyperpolarization level in PHIP-SAH-produced C13-pyruvate. *Journal of Magnetic Resonance* **289**, 12–17 (2018).
309. Plaumann, M. *et al.* Parahydrogen-Induced Polarization Transfer to 19F in Perfluorocarbons for 19F NMR Spectroscopy and MRI. *Chemistry–A European Journal* **19**, 6334–6339 (2013).
310. Kuhn, L. T. & Bargon, J. Transfer of parahydrogen-induced hyperpolarization to heteronuclei. *In Situ NMR Methods in Catalysis* 25–68 (2006).
311. Goldman, M. & Jóhannesson, H. Conversion of a proton pair para order into 13C polarization by rf irradiation, for use in MRI. *C R Phys* **6**, 575–581 (2005).
312. Haake, M., Natterer, J. & Bargon, J. Efficient NMR pulse sequences to transfer the parahydrogen-induced polarization to hetero nuclei. *J Am Chem Soc* **118**, 8688–8691 (1996).
313. Kadlecek, S., Emami, K., Ishii, M. & Rizi, R. Optimal transfer of spin-order between a singlet nuclear pair and a heteronucleus. *Journal of Magnetic Resonance* **205**, 9–13 (2010).
314. Jóhannesson, H., Axelsson, O. & Karlsson, M. Transfer of para-hydrogen spin order into polarization by diabatic field cycling. *C R Phys* **5**, 315–324 (2004).
315. Cai, C., Coffey, A. M., Shchepin, R. v, Chekmenev, E. Y. & Waddell, K. W. Efficient transformation of parahydrogen spin order into heteronuclear magnetization. *J Phys Chem B* **117**, 1219–1224 (2013).
316. Waddell, K. W., Coffey, A. M. & Chekmenev, E. Y. In situ detection of PHIP at 48 mT: demonstration using a centrally controlled polarizer. *J Am Chem Soc* **133**, 97–101 (2011).
317. Agraz, J. *et al.* LabVIEW-based control software for para-hydrogen induced polarization instrumentation. *Review of Scientific Instruments* **85**, 044705 (2014).
318. Cavallari, E., Carrera, C., Boi, T., Aime, S. & Reineri, F. Effects of magnetic field cycle on the polarization transfer from parahydrogen to heteronuclei through long-range J-couplings. *J Phys Chem B* **119**, 10035–10041 (2015).
319. Bastiaansen, J. A. M., Cheng, T., Lei, H., Gruetter, R. & Comment, A. Direct noninvasive estimation of myocardial tricarboxylic acid cycle flux in vivo using hyperpolarized 13C magnetic resonance. *J Mol Cell Cardiol* **87**, 129–137 (2015).
320. Cavallari, E., Carrera, C., Aime, S. & Reineri, F. Metabolic Studies of Tumor Cells Using [1-13C] Pyruvate Hyperpolarized by Means of PHIP-Side Arm Hydrogenation. *ChemPhysChem* **20**, 318–325 (2019).
321. Wang, Z. J. *et al.* Hyperpolarized 13C MRI: state of the art and future directions. *Radiology* **291**, 273–284 (2019).
322. Shchepin, R. v *et al.* Hyperpolarization of “neat” liquids by NMR signal amplification by reversible exchange. *J Phys Chem Lett* **6**, 1961–1967 (2015).

Appendixes

Starting with [IrCl(COD)(SIPr)] and the constant flip angle data of Table 1 we can see that the 5° and 10° results for a repetition rate of 5 seconds are statistically invariant for both peak A, the resonance at 203 ppm for the site next to the CH_3 and peak B, at 169.9 ppm for the acid site. When the spacing between measurements increases to 10 seconds, again, there is no impact within the errors and so both approaches prove equally valid. Interestingly, the errors resulting for the 10° measurements are consistently less than those for the 5° data which suggests that signal to noise, which will be larger with the higher value, might contribute to this. Specifically, low signal to noise would reduce the response that is visible for the longer time points and thereby act to decrease the apparent lifetime.

This reduction in signal is dealt with in the variable flip angle measurements, which aim to create a constant response level, although it uses up a larger amount of the magnetisation reservoir as a consequence. Table 2 presents the results of this for [IrCl(COD)(SIPr)]. The lifetime for the magnetisation yielding peak A increase from the average constant flip angle value of 23.3 ±1.0 s to 32.3 ±0.4 s with the 5 second spacing, and 27.9 s (±0.9) with the 10 second spacing.

In contrast, the time constants for peak B now reduce to 31.1 ± 1.1 s and slightly rise to 45.2 ± 1.1 s respectively. Based on these observations it would appear that signal-noise is a key issue and the variable flip angle experiments are more robust.

Hence, we can confirm that signal to noise in the longer time space is critical points. It would appear that relaxation causes a drop off the 10 second spaces data. Consequently, the more valid T1 for relaxation for peak A is 32.3 ± 0.4 s.

When the corresponding data for [IrCl(COD)(IMes)] are analysed (Table 3), the errors in both the 5° and 10° values are reduced by up to 80% relative to those for [IrCl(COD)(SIPr)]. However, it should be noted that the 5° angle with the 10 second spacing yields the larger error. This would again be consistent with a signal to noise effect. If this hypothesis is true, then signal enhancement should map directly onto the error level. Since [IrCl(COD)(IMes)] gives the largest enhancement values across the series it should on this basis also give the smallest error. The variable flip angle experiments now follow the same trend, with the longer time interval giving a smaller value, and the absolute value being larger than for the constant flip angle data. For peak B where there is a longer T_1, the larger spacing give a better sampling duration, which manifests itself in a longer T_1.

These trends are consistent across the series, [IrCl(COD)(SIPr)], [IrCl(COD)(IMes)], [IrCl(COD)(SIMes)], [IrCl(COD)(IPr)] and [IrCl(COD)(SIPr)]

Table 1. Constant flip angle derived T_1 values for pyruvate peaks A and B resulting from samples of 0.0032 mmol [IrCl(COD)(SIPr)], *p*-H_2, 1.5 uL DMSO-d_6 and 0.0179 mmol $^{13}C_2$ pyruvate.

Expt. No.	Pulse Angle	D1	T_1	
			A peak	B peak
1	5	5	22.4 ± 0.8	41.8 ± 1.5
2	10	5	24.2 ± 1.2	46.0 ± 1.6
3	10	10	24.0 ± 0.9	44.7 ± 1.4
4	5	10	21.0 ± 3.8	44.9 ± 2.4

Table 2. Variable flip angle derived T_1 values for pyruvate peaks A and B resulting from samples of 0.0032 mmol [IrCl(COD)(SIPr)], *p*-H_2, 1.5 uL DMSO-d_6 and 0.0179 mmol $^{13}C_2$ pyruvate.

No.	D20	T_1	
		A peak	B peak
1	5	32.3 ± 0.4	31.1 ± 1.1
2	10	27.9 ± 0.9	45.2 ± 1.1

Table 3. Constant flip angle derived T_1 values for pyruvate peaks A and B resulting from samples of 0.0032 mmol [IrCl(COD)(IMes)], *p*-H_2, 1.5 uL DMSO-d_6 and 0.0179 mmol $^{13}C_2$ pyruvate.

No.	Angle	D1	T_1	
			A peak	B peak
1	5	5	24.4 ± 0.4	41.9 ± 0.7
2	10	5	24.6 ± 0.3	42.5 ± 0.4
3	10	10	24.7 ± 0.8	42.3 ± 0.9
4	5	10	22.6 ± 1.5	38.1 ± 2.2

Table 4. Variable flip angle derived T_1 values for pyruvate peaks A and B resulting from samples of 0.0032 mmol [IrCl(COD)(SIPr)], *p*-H_2, 1.5 uL DMSO-d_6 and 0.0179 mmol $^{13}C_2$ pyruvate.

No.	D20	T_1	
		A peak	B peak
1	5	38.3 ± 1.6	35.9 ± 2.0
2	10	29.1 ± 0.9	46.9 ± 2.2

Table 5. Constant flip angle derived T_1 values for pyruvate peaks A and B resulting from samples 0.0032 mmol [IrCl(COD)(SIMes)], *p*-H_2, 1.5 uL DMSO-d_6 and 0.0179 mmol $^{13}C_2$ pyruvate.

Experiment No.	Angle	D1	T_1	
			A peak	B peak
1	5	5	26.8 ± 0.9	51.6 ± 2.4
2	10	5	26.9 ± 0.8	54.8 ± 1.0
3	10	10	26.9 ± 1.0	52.0 ± 3.1
4	5	10	27.3 ± 1.4	51.0 ± 2.0

Table 6. Variable flip angle derived T_1 values for pyruvate peaks A and B resulting from samples of 0.0032 mmol [IrCl(COD)(SIMes)], *p*-H_2, 1.5 uL DMSO-d_6 and 0.0179 mmol $^{13}C_2$ pyruvate.

No.	D20	T_1	
		A peak	B peak
1	5	38.7 ± 1.3	33.1 ± 1.5
2	10	31.0 ± 0.2	50.4 ± 0.9

Table 7. Constant flip angle derived T_1 values for pyruvate peaks A and B resulting from samples 0.0032 mmol [IrCl(COD)(IPr)], *p*-H_2, 1.5 uL DMSO-d_6 and 0.0179 mmol $^{13}C_2$ pyruvate.

Experiment No.	Angle	D1	T1	
			A peak	B peak
1	5	5	26.2 ± 0.4	47.7 ± 1.2
2	10	5	27.2 ± 0.3	49.7 ± 0.5
3	10	10	27.0 ± 0.8	49.4 ± 0.7
4	5	10	27.0 ± 0.9	47.5 ± 0.9

Table 8. Variable flip angle derived T_1 values for pyruvate peaks A and B resulting from samples of 0.0032 mmol [IrCl(COD)(IPr)], *p*-H_2, 1.5 uL DMSO-d_6 and 0.0179 mmol $^{13}C_2$ pyruvate.

No.	D20	T1	
		A peak	B peak
1	5	44.7 ± 1.7	35.7 ± 1.5
2	10	34.9 ± 1.7	50.1 ± 1.7

Table 9. Constant flip angle derived T_1 values for pyruvate peaks A and B resulting from samples 0.0032 mmol [IrCl(COD)(SIPr)], *p*-H_2, 1.5 uL DMSO-d_6 and 0.0179 mmol $^{13}C_2$ pyruvate.

Experiment No.	Angle	D1	T1	
			A peak	B peak
1	5	5	18.1 ± 1.3	29.1 ± 1.5
2	10	5	17.0 ± 1.0	29.5 ± 1.0
3	10	10	17.6 ± 0.4	28.1 ± 2.3
4	5	10	14.1 ± 2.2	18.7 ± 1.1

Table 10. Variable flip angle derived T_1 values for pyruvate peaks A and B resulting from samples of 0.0032 mmol [IrCl(COD)(SIPr)], *p*-H_2, 1.5 uL DMSO-d_6 and 0.0179 mmol $^{13}C_2$ pyruvate.

Experiment No.	D20	T1	
		A peak	B peak
1	5	23.0 ± 0.2	36.9 ± 1.2
2	10	20.1 ± 0.3	36.0 ± 2.3

Table 11. Variable flip angle derived T_1 values for pyruvate peaks A and B resulting from samples of 0.0032 mmol [IrCl(COD)(IMes)], *p*-H_2, 1.5 uL DMSO-d_6 and 0.0179 mmol $^{13}C_2$ pyruvate.

Experiment No.	D20	T1	
		A peak	B peak
1	5	38.9 ± 0.6	32.8 ± 1.3
2	10	30.9 ± 0.4	42.2 ± 1.0

Table 12. Constant flip angle derived T_1 values for pyruvate peaks A and B resulting from samples 0.0032 mmol [IrCl(COD)(IMes)], *p*-H_2, 1.5 uL DMSO-d_6 and 0.0179 mmol $^{13}C_2$ pyruvate.

Experiment No.	Angle	D1	T1	
			A peak	B peak
1	5	5	25.4 ± 0.3	40.4 ± 0.8
2	10	5	26.2 ± 0.3	39.9 ± 0.4
3	10	10	25.9 ± 0.8	40.3 ± 0.5
4	5	10	26.8 ± 1.4	38.2 ± 1.0